FACULDADE DE ENGENHARIA DA UNIVERSIDADE DO PORTO

Development of accurate numerical methodologies applied to the stamping of advanced high strength steels and experimental validation

Rui Ricardo Loureiro Amaral

U.PORTO
FEUP FACULDADE DE ENGENHARIA
UNIVERSIDADE DO PORTO

Programa Doutoral em Engenharia Mecânica

Supervisor: Abel Dias dos Santos

Co-supervisor: José Manuel de Almeida César de Sá

September, 2020

Development of accurate numerical methodologies applied to the stamping of advanced high strength steels and experimental validation

Rui Ricardo Loureiro Amaral

Programa Doutoral em Engenharia Mecânica

Approved by:

President: Dr. Renato Manuel Natal Jorge
Professor at Department of Mechanical Engineering, Faculty of Engineering of University of Porto

Referee: Dr. Marta Cristina Cardoso de Oliveira
Professor at Department of Mechanical Engineering, Faculty of Sciences and Technology of University of Coimbra

Referee: Dr. José Luís Carvalho Martins Alves
Professor at Department of Mechanical Engineering, University of Minho

Referee: Dr. Pedro Manuel Cardoso Teixeira
Researcher at Frezite High Performance Lda.

Referee: Dr. Abílio Manuel Pinho de Jesus
Professor at Department of Mechanical Engineering, Faculty of Engineering of University of Porto

Referee: Dr. Abel Dias dos Santos
Professor at Department of Mechanical Engineering, Faculty of Engineering of University of Porto

(This page was deliberately left blank)

Abstract

The trend towards the use of higher strength materials, such as Advanced High Strength Steels (AHSS), created new challenges to sheet metal forming processes, both in obtaining a component without defects and when using numerical simulation to predict material behavior and deformation limits, before breakage. These new challenges shaped the need for development of new numerical tools and constitutive mathematical models, with the potential for better replicating the material behavior in the sheet metal forming processes.

This thesis is a contribution to take a step forward on this kind of research, while its innovative approach seeks to provide the development and improvement of methodologies that allow the use of new numerical tools, aiming to a more accurate prediction of material behavior.

A suitable set of experimental tests for mechanical characterization and material formability has been defined and performed, corresponding to different strain paths and different stress states, in order to improve the material behavior definition and consequently the accuracy of the numerical results.

Finite element numerical simulations and experimental tests were carried out to evaluate and compare the obtained results for this advanced high strength steels. The numerical simulation combined with different constitutive models was applied to a series of benchmark tests, corresponding to a variety of conditions in which a material can be subjected during the deformation process, including the deep drawing cylindrical cup, the Nakajima and the Cross-Die tests.

In case of the deep drawing cylindrical cup, different yield criteria were evaluated and analyzed, as well as the application of a non-associated plasticity flow rule. The earing profiles and the wall thickness distribution showed to be sensitive to the adopted yield criterion. The comparison with experimental data indicates that the use of a non-associated plasticity flow rule can be more efficient, improving the accuracy of the predicted anisotropic behavior for the proposed materials.

Additionally, in order to verify and validate the applicability of ductile damage models to predict the occurrence of fractures, finite element simulations of the Nakajima and Cross-Die tests were performed. The implemented uncoupled damage models show to predict the same behavior and a very similar fracture location when compared to the experimental evidence.

Keywords: Sheet metal forming, Numerical simulation, Benchmark tests, Yield criteria, Ductile damage models

(This page was deliberately left blank)

Resumo

A tendência para a utilização de materiais mais resistentes, como é o caso dos aços avançados de alta resistência (AHSS), definiu a existência de novos desafios para a obtenção de componentes metálicos em chapa e para o uso da simulação numérica na previsão do comportamento do material e dos seus limites de deformação plástica, em processos de conformação plástica de chapas metálicas. Com estes novos desafios, o desenvolvimento de ferramentas numéricas continua a ter um grande crescimento, tal como os modelos constitutivos que reproduzem o comportamento das chapas metálicas nos processos de conformação plástica.

Esta dissertação procura dar um passo em frente na pesquisa científica, enquanto que a sua abordagem inovadora pretende contribuir para o desenvolvimento e aperfeiçoamento de metodologias que permitam a criação de novas ferramentas de modelação numérica, com o objetivo de prever como maior rigor o comportamento mecânico de materiais metálicos.

Foi definido e realizado um conjunto adequado de ensaios experimentais de caraterização mecânica e de conformabilidade, correspondendo a diversas trajetórias de deformação e estados de solicitação, uma vez que a precisão dos resultados numéricos obtidos depende da correta caracterização do comportamento do material. Simulações de elementos finitos e testes experimentais foram realizados para avaliar e comparar os resultados obtidos para este tipo de aços avançados de alta resistência. A aplicação da simulação numérica em conjunto com os diferentes modelos constitutivos foi feita a um conjunto de ensaios *benchmark*, correspondentes a uma variedade de situações a que um material pode ser submetido durante o processo de deformação, entre os quais a embutidura de um copo cilíndrico, o ensaio *Nakajima* e o ensaio *Cross-Die*.

No caso da embutidura de um copo cilíndrico, foram avaliados e analisados diferentes critérios de cedência e também foi feita a aplicação de uma lei de plasticidade não-associada. Os perfis das orelhas de embutidura e a distribuição da espessura na parede do copo mostraram ser sensíveis ao critério adotado. A comparação com dados experimentais indicou que a utilização de uma lei de plasticidade não-associada pode ser mais eficiente, melhorando o rigor obtido da previsão do comportamento anisotrópico dos materiais estudados.

Adicionalmente, com o intuito de verificar e validar a aplicabilidade de modelos de dano na previsão da ocorrência de fratura, foram realizadas simulações de elementos finitos dos ensaios Nakajima e Cross-Die. Da comparação dos resultados numéricos com as evidências experimentais existentes ressalta que os modelos de dano não-acoplados preveem comportamentos muito semelhantes aos experimentais e uma previsão correta do local da fratura.

Palavras-chave: Estampagem, Simulação numérica, *Benchmarks* experimentais, Critérios cedência, Modelos de dano dúctil

(This page was deliberately left blank)

Acknowledgments

I would like to express my sincere gratitude to Professor Doctor Abel Dias dos Santos for the opportunity given to work in the scientific field through this thesis. His guidance and valuable suggestions, support, availability, and finally, his critical spirit in the thorough review of this text were fundamental for the coherence and concretization of this thesis.

To Professor José Manuel de Almeida César de Sá thanks for the availability and support provided in the numerical implementations. Its critical revision of this text was also fundamental to its consistency.

I want to thank INEGI (Institute of Science and Innovation in Mechanical and Industrial Engineering) for the availability of means granted during the performance of this work. The ease of access to INEGI various scientific and technological capabilities made it possible to carry out the extensive experimental work on which this thesis is based.

To my colleagues at UTAF (Advanced Manufacturing Processes), I wish to thank the fellowship and support in carrying out this research. Also, to all those who directly or indirectly contributed with their effort and assistance.

A deep appreciation to my family, who have always supported and encouraged me, I want to express my sincere gratitude for your understanding and support throughout this journey.

Finally, I gratefully acknowledge the financial support of the Portuguese Foundation for Science and Technology (FCT) for the Doctoral grant SFRH/BD/119362/2016 provided under the program POCH, co-financed by the European Social Fund (FSE) and Portuguese National Funds from MCTES. I am also grateful for the financial support from FCT under the projects POCI-01-0145-FEDER-032466, POCI-01-0145-FEDER-030592, POCI-01-0145-FEDER-031243 and NORTE-01-0145-FEDER-032419 by UE/FEDER through the programs COMPETE 2020 and NORTE 2020.

COMPETE 2020
PROGRAMA OPERACIONAL COMPETITIVIDADE E INTERNACIONALIZAÇÃO
NORTE 2020
PROGRAMA OPERACIONAL REGIONAL DO NORTE
PORTUGAL 2020
UNIÃO EUROPEIA
Fundo Social Europeu
Fundo Europeu de Desenvolvimento Regional
FCT
Fundação para a Ciência e a Tecnologia

(This page was deliberately left blank)

”Before you say you can’t do something, try it”

Kiichiro Toyoda

(This page was deliberately left blank)

Contents

List of Figures

List of Tables

Acronyms and Nomenclature

Acronyms

AFR	Associated Flow Rule
AHSS	Advanced High Strength Steels
BCC	Body Centered Cubic
CPB06	Cazacu, Plunkett and Barlat 2006 yield criterion
DIC	Digital Image Correlation
DP	Dual-phase
FCC	Face Centered Cubic
FEA	Finite Element Analysis
FEM	Finite Element Method
FLC	Forming Limit Curve
FLD	Forming Limit Diagram
GTN	Gurson–Tvergaard–Needleman damage model
IFR	Infrared thermography
LDR	Limiting drawing ratio
MSTD	Mini Sample Tester Device
NAFR	Non-associated Flow Rule
RD,DD,TD	Rolling, Diagonal and Transverse Directions
SD	Stress Differential
SEM	Scanning Electron Microscope
Yld’89	Barlat and Lian 1989 yield criterion
Yld’91	Barlat. Lege and Brem 1991 yield criterion

Nomenclature

α	Swift+Voce hardening law weighting parameter
$\Delta\bar{\varepsilon}^p$	Equivalent plastic strain increment
$\Delta\lambda$	Plastic multiplier increment
Δr	Planar anisotropic coefficient
$\boldsymbol{\varepsilon}$	Strain tensor
ε^b	Biaxial strain
$\boldsymbol{\varepsilon}^e$	Elastic strain tensor
$\boldsymbol{\varepsilon}^p$	Plastic strain tensor
η	Stress triaxiality
ϕ	Yield condition
λ	Plastic multiplier
ρ	Radius of curvature
$\boldsymbol{\sigma}$	Cauchy stress tensor
$\sigma_1, \sigma_2, \sigma_3$	Principal stresses
$\overline{\sigma}$	Equivalent yield stress
σ_θ	Yield stress corresponding to the direction with the angle θ relative to the rolling direction
σ_b	Biaxial yield stress
σ_Y	Flow stress
σ_m	Mean stress
σ_0, K, n	Ludwik law parameters
$\overline{\theta}$	Lode angle parameter

A, B, C	Voce law parameters
a, b, c, f, g, h, m	Yld'91 yield criterion anisotropic parameters
a, b, c, n	Hosford-Coulomb damage model parameters
a, c, h, p, M	Yld'89 yield criterion anisotropic parameters
$C_{11}, C_{12}, C_{13}, C_{22}, C_{23}, C_{33}, C_{66}$	CPB06 yield criterion anisotropic parameters

D	Damage variable
$\boldsymbol{D}$	Elastic matrix
d_1, d_2, d_3, d_4, d_5	Johnson-Cook damage model parameters
e	Engineering strain
F, G, H, L, M, N	Hill'48 yield criterion anisotropic parameters
I_1, I_2, I_3	First, second and third invariant of Cauchy stress tensor
J_1, J_2, J_3	First, second and third invariant of deviatoric stress tensor
K, ε_0, n	Swift law hardening parameters
l_0	Clip gage initial length
$q_1, q_2, q_3, f_0, f_c, f_F, \varepsilon_N, S_N, f_N$	GTN damage model parameters
r	Plastic anisotropic coefficient
$\bar{r}$	Normal anisotropic coefficient
r_b	Biaxial anisotropic coefficient
r_θ	Plastic anisotropic coefficient for θ angle orientation relative to the rolling direction
S	Engineering stress
W	Equivalent plastic work per unit volume

(This page was deliberately left blank)

Chapter 1

Introduction

This chapter presents the overall framework of the challenges related to sheet metal forming processes, highlighting the importance of finite element numerical simulation. Additionally, the main objectives of the work carried out in this thesis are defined, taking into consideration its technological and industrial interest. Moreover, the outline and contents of this thesis are also presented.

(This page was deliberately left blank)

1.1 Motivation

Sheet metal forming processes are one of the main manufacturing possibilities in the production of metal components [1], being currently applied in a wide variety of industrial areas, such as the automotive, naval, electrical, aeronautical and aerospace industries, among other sectors.

Main advantages of these processes include the production of mechanical parts with high production rates and practically full use of the raw material. Of all the forming techniques, stamping is a widespread process, particularly in the automotive industry, being responsible for large volumes of production, as well as a wide variety of components (figure 1.1).

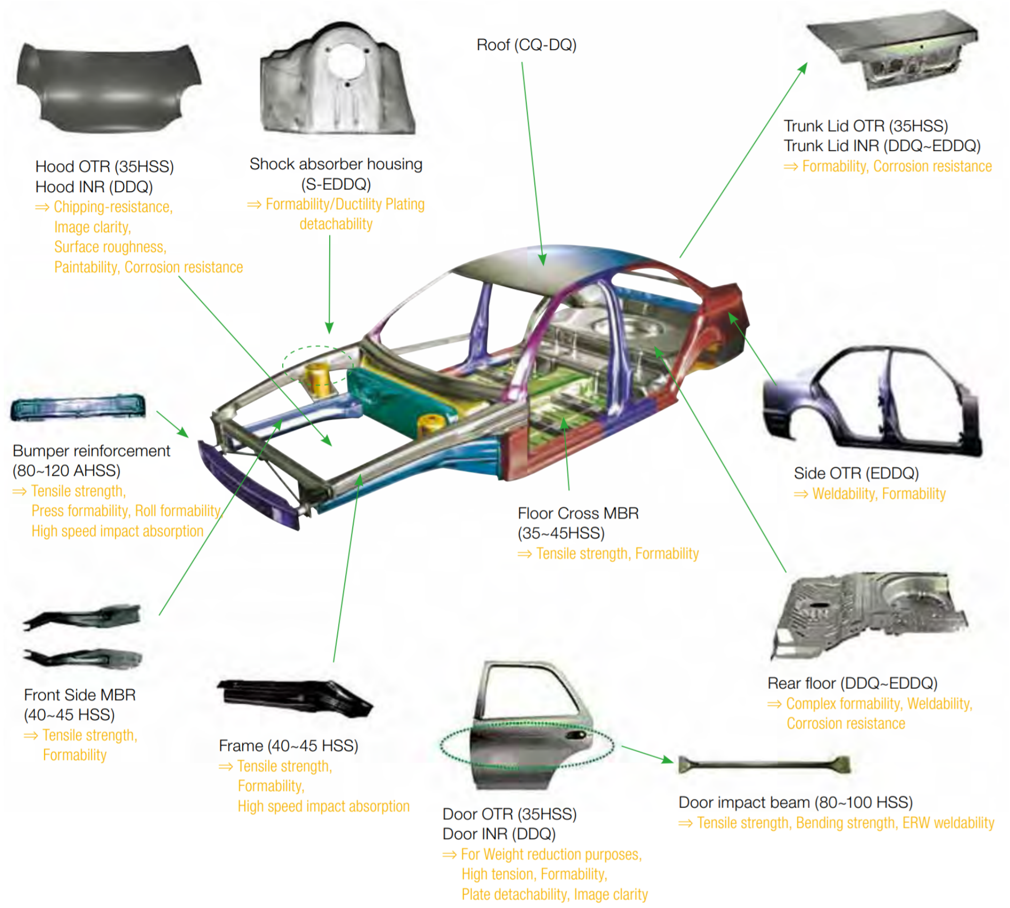

Figure 1.1: Use of different types of steels in the production of different automobile body structure components (adapted from [2]).

Metal stamping transforms sheet metal into different custom shapes, using machine presses and stamping tools. Tools usually include a punch, a die and a blank holder. These tools will apply external force on a flat metal sheet to promote the plastic deformation of the material and to obtain the desired shape.

Nowadays, the tendency of increasing complexity of product geometries, as well as the introduction of new materials and reduction of design-production cycles, a trend as seen in transportation industries, creates a constant need for research and technological advances. As the service life of the products has been decreasing, a quicker and flexible development stage is required, while keeping or even improving the final quality of the component. In general, numerous, costly and time-consuming trial-and-error cycles were required between the design and final product phases, in which prior knowledge and experience were essential concerning the technological process, product geometry and the material to deform. However, experience is not enough, while trial-error methodology is very expensive with respect to both money and time. Therefore, there is a need for development of both theoretical and experimental engineering methods enabling problems to be solved efficiently, thus reducing manufacturing costs and the time between design and start of production. Also, to face current trends, it is needed a continuous development concerning materials, concerning new innovative forming processes, in addition to the developments in tooling and manufacturing equipment.

Currently, in automotive industry there is an emphasis on weight reduction of vehicle body in order to improve vehicle fuel economy, the corresponding emissions in greenhouse gases and the lightweight design. In parallel, aspects related to passenger safety are uninterruptedly improved, mainly due to demanding imposed legislation. One method to accomplish these goals is to incorporate lightweight materials into the vehicle body structure, but also capable of supporting any load to maintain its structural integrity [3, 4].

Advanced High Strength Steels (AHSS) are among the materials that are currently seeing increased usage and implementation in weight reduction efforts due to their high strength-to-weight ratio. However, manufacturing automotive parts with AHSS have imposed many challenges [5]. One of the barriers to further implementation of these materials is the observed behavior that differs from mild steels and conventional high strength steels and, therefore, all the empirical knowledge learned over the years cannot be generalized to these new materials, needing the definition of new operating settings for the success of the forming processes. These conditions also seem to contribute for the inconsistent forming behavior of AHSS, i.e., unexpected fractures [6] occurring on high curvature die radii [7], while enhanced formability is observed with combined modes of deformation of stretching and bending [8, 9]. It is known that combination of stretching and bending effects can influence the material formability [10, 11]. This effect seems to be significantly more pronounced for AHSS than for conventional grades [6]. The formability of the AHSS seem also being more sensitive to combined stretching modes as well as deformation-induced heating, particularly in high strain rate conditions [12, 13]. As a result, the in-plane deformation forming limit, used to predict formability of conventional steels shows an underestimation of the forming limit strains, which prevent designers from exploring AHSS potential formability.

Therefore, the adoption of virtual production concepts and numerical methods tends to reduce the expensive and long experimental tryouts (tuning) in the press shop and evaluate the material behavior during deformation. This fact is due to the greater interactivity between the conceptualization and design phases of components and forming tools, using numerical simulation.

The numerical simulation of sheet metal forming processes has been playing a fundamental role in the reduction of development times, as well as the introduction of new materials. It allowed extending the application domain to more complex plastic deformation problems [14], which involve non-linearities of the material mechanical behavior associated with the hardening and anisotropy phenomena, strain rate and strain path sensitivity, temperature effects , material internal damage [15] and friction resulting from the contact between the material and the tools.

In the last decades, a constant and evolving effort was made in the development and implementation of constitutive models and tools in numerical simulation, making it possible to obtain accurate and faster results. However, such accuracy depends on the correct material characterization, as well as the definition of the process conditions. Regarding the material behavior, several researchers have been proposed different approaches, including hardening, anisotropy prediction, material strength degradation (damage), all of them needing an accurate identification of corresponding parameters, usually based on experimental information [16].

The automotive industry is a sheet metal forming sector that benefits from the use and development of numerical tools, as it faces a growing trend of demands imposed by environmental issues and by its consumers. From the design perspective, the stamping sector needs forming guidelines for AHSS, based on the development of FEA constitutive predictive models and valid formability references, having always in mind its industrial application.

1.2 Objectives

This work intends to take a step forward on research while its innovative approach seeks to contribute to the development and refinement of skills in the area of numerical simulation of technological processes, particularly in sheet metal forming processes, taking into account different methodologies to determine the mechanical behavior of metallic materials, applied to Advanced High Strength Steels, always having in mind its industrial applications. These objectives incorporate a general-purpose finite element analysis (FEA) program, more specifically, the ABAQUS^{TM} software.

The methodology considered will characterize the influence of material anisotropic effects on the behavior of selected materials, shedding light on the mechanisms leading to defects during processing. It is also expected that developed models will enable highlighting different failure mechanisms occurring in metal forming processes. Nowadays it is accepted that the failure mode exhibits a stress dependency that at the macro scale (i.e., in the phenomenological material laws normally used) is reflected by the inclusion of parameters that depend on triaxiality or on the so-called Lode angle, representing more traction or shear dependent failures.

The numerical simulation will be applied to different experimental benchmarks, representing different types of loading conditions present in the stamping field, in order to study and evaluate the ability of each constitutive model to predict the material's behavior using for such purpose, a set of parameters previously identified based on experimental characterization tests data. It is expected that this improved knowledge will contribute to a more suitable formability prediction in stamping processes and virtual tool tryout, using finite element method (FEM) codes.

In brief, the work addresses material and process conditions modeling, using ever growing computer capabilities, but exploring new ways and methodologies in simulation-based engineering science, by means of constitutive models, in parallel with relying on an interdisciplinary research and experimental validation.

1.3 Outline of the thesis

This thesis aims to apply the finite element method in the numerical simulation on the sheet metal forming process, using the ABAQUS^{TM} analysis program. In addition to current chapter (Chapter 1), where a brief introduction to numerical simulation and sheet metal forming is presented, this thesis consists of other five chapters and appendixes.

Chapter 2 presents some fundaments and basic concepts for the constitutive modeling of metallic materials behavior. Different topics are covered, starting with hardening, also considering yield criteria and including damage prediction models

Chapter 3 gives a brief description of the materials used in this study, as well as the respective mechanical characterization and its forming limits.

Chapter 4 describes strategies for the determination and identification of parameters for constitutive models (covered in Chapter 2), based on experimental data obtained in Chapter 3. The identified parameters in this chapter are used as input in the numerical simulations presented in Chapter 5.

In Chapter 5, results from the numerical simulation of experimental benchmark tests are evaluated and analyzed to determine and predict typical defects and behaviors that occur in metal parts obtained by the plastic deformation processes.

Chapter 6 presents the main conclusions of this thesis, along with some perspectives and suggestions for future work.

(This page was deliberately left blank)

Chapter 2

Constitutive modeling

This chapter presents a brief description of the constitutive modeling of sheet metal materials, concerning its mechanical properties, plastic and damage behavior in the numerical simulation of forming processes. Different approaches to describe the material behavior are shown, taking always in consideration its industrial usage and applicability.

(This page was deliberately left blank)

2.1 Introduction

Constitutive models are ever-present in scientific research, as well as in manufacturing processes, as a tool for a more detailed understanding of some physical phenomena, which can lead to an improvement or the development of new products. The primary purpose of material constitutive models is to reproduce, as close as possible, the reality under different assumptions and requirements, depending on the final goal and application area of the model.

The prediction of material behavior during the plastic sheet metal forming operation using numerical simulation has become an essential factor of technological interest [17]. Moreover, the ability to preview results, based on numerical simulation, allows the evaluation of material attributes, the detection and prevention of possible errors or the improvement and fine-tuning of the technological process, contributing to the constant increase in efficiency in terms of time and cost reduction, as well as to improving the quality of the final product.

In recent years, enormous efforts have been contributed to develop new constitutive models or to modify existent ones that describe the various sheet metal behaviors mathematically, from hardening to damage, not overlooking the anisotropy. Such need also arises from the introduction of new advanced materials whose behavior differs from those already well known and whose lack of accuracy in describing the mechanical behavior is evident [18]. Although, the accuracy of the results obtained by the numerical simulation depends, among other factors, on the characterization of the mechanical properties of the materials.

The level of uncertainties that are involved in material characterization creates challenges in constitutive modeling of sheet materials and therefore compromising the reliability of finite element simulations of forming processes [19]. The selection of the constitutive model that best reproduces the behavior of the material, which can be characterized by an arrangement of different properties (e.g. isotropic hardening with plastic anisotropy), has an essential contribution to such precision of results. Nevertheless, the benefit of the identified best material model has to be evaluated within its application context, considering that other process parameters can influence the final result [20].

The introduction of digital image correlation (DIC) techniques allowed the increasing of analysis area and the accuracy of obtained data, since it is possible to compare the global deformation field between experimental and numerical directly [21]. Scientific studies show that the hardening of the material is described in a very acceptable way; however, in some cases, there are differences between the measured and calculated strains [22]. This finding suggests that the classic approach of some constitutive models, in particular yield functions, which popularity are increasing in industry and numerical simulation codes, still does not allow accurate reproduction of different types of requests. A benchmark that demonstrates this phenomenon and that is well studied is the deep drawing cylindrical cup test, being the earing profile of the cylindrical cup a reference data to test and evaluated the capabilities of the constitutive models implemented in the numerical simulation [23].

The most basic approach to model a material, regarding its application to sheet metal forming processes, is its hardening behavior combined with a suited hardening law and a yield criterion to model the plastic anisotropic behavior. Figure 2.1 shows a scheme with different constitutive approaches used in numerical simulation and already available in some commercial finite element codes that can be considered to reproduce the material's behavior.

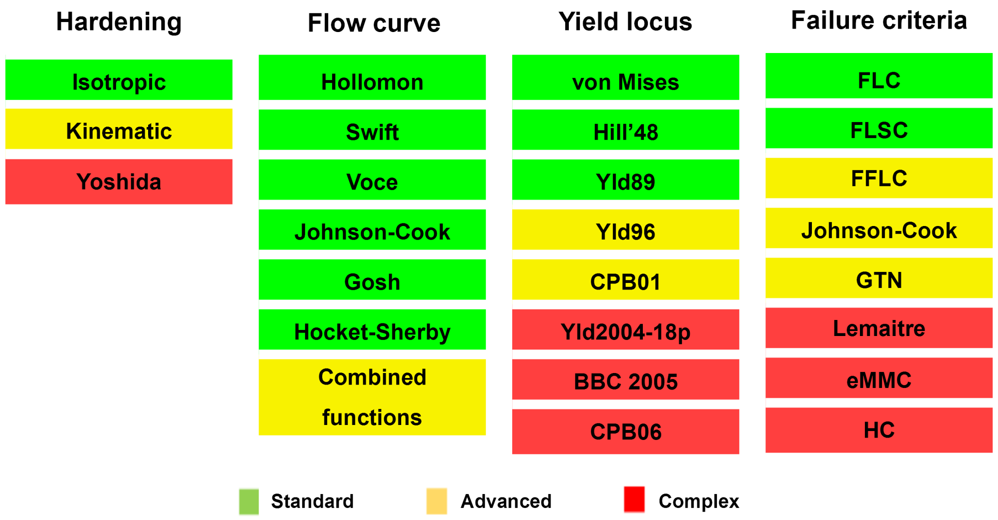

Hardening	Flow curve	Yield locus	Failure criteria
Isotropic	Hollomon	von Mises	FLC
Kinematic	Swift	Hill'48	FLSC
Yoshida	Voce	Yld89	FFLC
	Johnson-Cook	Yld96	Johnson-Cook
	Gosh	CPB01	GTN
	Hocket-Sherby	Yld2004-18p	Lemaitre
	Combined functions	BBC 2005	eMMC
		CPB06	HC

🟩 Standard 🟨 Advanced 🟥 Complex

Figure 2.1: Implementation complexity of different constitutive models with respect to the main purpose

Although it is not mentioned in figure 2.1, some researchers reported that the use of multi-scale models allows describing more accurately the deformation mechanisms which occur at the microscopic scale. However, such models are not suitable for industrial applications, since the time required to obtain results from numerical simulation of sheet metal forming processes makes their use unfeasible [24]. This drawback is one of the many reasons why there is still a focus on improving classic approaches, such as hardening of the material, modeling of anisotropy and degradation of material strength (damage).

In this chapter, a particular focus will be given to different techniques for the mathematical description of the hardening of materials, as well as the relationship between the anisotropic models and the non-associative flow rule, a topic receiving currently more attention. Besides, different methodologies for predicting damage of metallic materials during the forming process will be addressed. The following sections describe the possible ways to model the material behavior for application to sheet metal forming simulations.

2.2 Hardening behavior

In general, for the progress of the plastic deformation, a different stress level from the initial state is necessary, which depends on the amount of plastic deformation imposed in the material. This phenomenon, called hardening, defines that the yield surface varies with the development of the plastic deformation. So, the yield condition can be mathematically expressed in the form $\phi = f(\boldsymbol{\sigma}) - \sigma_Y(\varepsilon^p) = 0$. This relation implies that yielding occurs when the effective stress $f(\boldsymbol{\sigma}) = \overline{\sigma}$, which is a scalar function of the state of stress, reaches a critical value σ_Y, which in turn is a function of the effective plastic strain ε^p. The function $\sigma_Y(\varepsilon^p)$ is usually obtained from a uniaxial stress vs plastic strain curve [25, 26].

Figure 2.2 shows some of the models commonly used to characterize the hardening behavior of materials during plastic deformation.

The first model shown in figure 2.2(a) refers to a material that undergoes hardening, since the yield surface increase with loading. This type of hardening is called isotropic hardening. It is characterized by the yield locus expanding evenly, without changing its shape. In this hardening model, it is assumed that both tensile and compression stresses are initially equal, i.e., the stress asymmetry that develops for different deformation trajectories, such as the Bauschinger effect, can be neglected.

Finally, the second model shown in figure 2.2(b), is defined by the fact that the subsequent yield surface preserves their shape and dimension, but undergo rigid body translations in the plane $\sigma_1 - \sigma_2$, and, for this reason, it is called kinematic hardening. This type of hardening is applied in cases where the Bauschinger effect is important, for example, when there is an abrupt inversion of the strain path. This is not a common situation in plastic deformation processes, where the deformation trajectories are in general monotonic, and the strain levels are very high. However, there are still hardening models which result from a combination of the isotropic and kinematic hardening [27, 28].

It should be noted that there is still the case of a perfectly plastic material, i.e., it does not suffer hardening and its yield surface remains constant in the stress space. For this

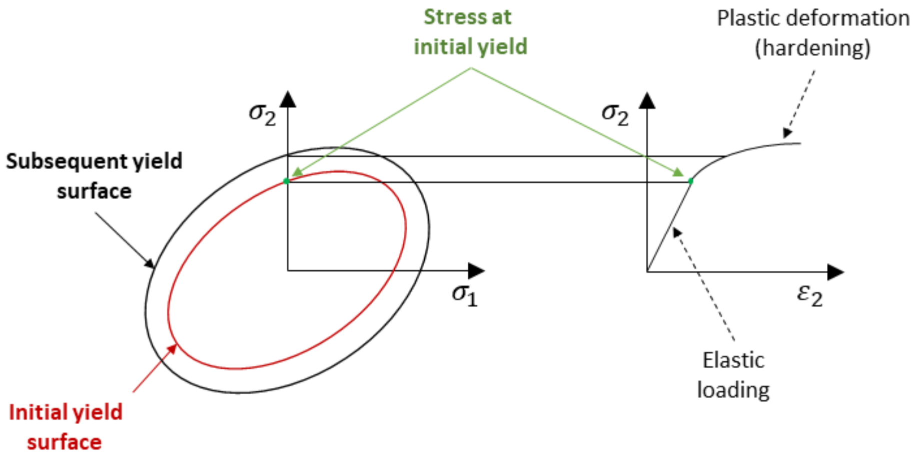

(a) Isotropic hardening

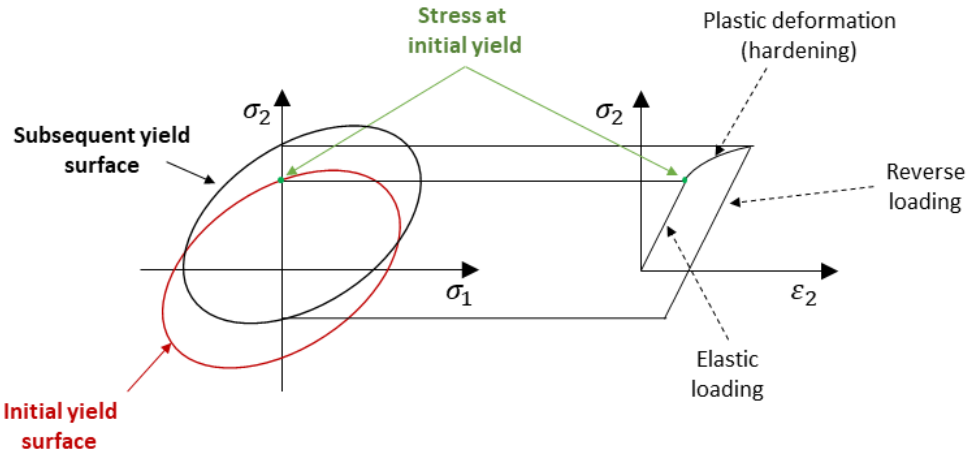

(b) Kinematic hardening

Figure 2.2: Types of models used for hardening description. (Note: The scheme was constructed based on the von Mises yield surface).

situation, the vector representing the stress state will have to vary so that its extreme point is always located on the initial yield surface.

Considering both hardening models, only the isotropic hardening will be used in this thesis, since there is no experimental data available to evaluate and to model the kinematic hardening and the cases to be covered do not have emphasis on inversion of the strain paths.

Among the different isotropic hardening laws proposed by several authors, the following stand out:

1. Ludwik, in 1909 [29]:

$$\sigma_Y = \sigma_0 + K \cdot \varepsilon_p^n \tag{2.1}$$

2. Hollomon, in 1945 [30]:

$$\sigma_Y = K \cdot \varepsilon_p^n \tag{2.2}$$

3. Voce, in 1948 [31]:

$$\sigma_Y = A - B\left(1 - e^{-C \cdot \varepsilon_p}\right) \tag{2.3}$$

4. Swift, in 1952 [32]:

$$\sigma_Y = K(\varepsilon_0 + \varepsilon_p)^n \tag{2.4}$$

5. Hockett-Sherby, in 1975 [33]

$$\sigma_Y = A + B(1 - e^{-C \cdot \varepsilon_p^n}) \tag{2.5}$$

6. Ghosh, in 1977 [34]:

$$\sigma_Y = A(\varepsilon_p + B)^n - C \tag{2.6}$$

7. Combination of Swif and Voce law [35]

$$\sigma_Y = \alpha\left[K(\varepsilon_0 + \varepsilon_p)^n\right] + (1 - \alpha) \cdot \left[A + B(1 - e^{-C \cdot \varepsilon_p})\right] \tag{2.7}$$

The Swift law is more appropriated to describe the behavior of materials that exhibit isotropic hardening without saturation.

On the other hand, the Voce law is more appropriated to describe the behavior of materials that exhibit isotropic hardening with saturation. This means, that for higher values of plastic strain, the equivalent stress prediction will be different between these two constitutive models.

Combining these two laws (Swift+Voce) allows to describe a material mechanical behavior that exhibits a high initial hardening behavior and saturation for higher levels of plastic extension.

2.3 Plasticity yield surface models

The plasticity theory establishes relationships that allow knowing which are the conditions of entry into the plastic regime of a given metallic material when it is subjected to a determined stress state due to a loading. Most technological processes of sheet metal forming involve multiaxial stress states, making the problem more complex than the simple uniaxial type, as in case of the tensile test.

To describe the plastic behavior of a sheet metal material for any general stress state, a yield criterion should be considered, which allows the identification of the transition moment from the elastic to the plastic regime. Another important point that is needed in plasticity is the stress and strain-rate components relationship, being given by a flow rule, which can be associated (AFR) or non-associated (NAFR). Nevertheless, the amount of hardening and corresponding evolution of a potential surface are described by a hardening rule during the plastic deformation.

The previous assumptions make clear that a yield criterion is a function of the stress tensor components and for a defined stress state, the elastic limit condition is expressed by:

$$\phi = \overline{\sigma} - \sigma_Y = 0 \tag{2.8}$$

where $\overline{\sigma}$ is the equivalent stress of a known yield function ($f(\boldsymbol{\sigma}_{ij})$) and σ_Y is a material property, usually associated with the scalar flow stress value from the hardening law.

For an arbitrary loading point, if $\phi < 0$ the deformation is purely elastic (inside of the yield surface). When the elastic limit is reached ($\phi = 0$), the material will deform permanently due to the plastic behavior. In case of the initial state, the flow stress corresponds to the elastic limit, being the yield stress from uniaxial tensile test a standard reference value.

In order to determine the constitutive equations of the plastic domain for a given material, it is necessary to relate the stresses to the strain increment, knowing that the plasticity criterion provides the combination of stresses that establish the beginning of the plastic flow. Decomposing the stress increment vector $d\boldsymbol{\sigma}_{ij}$, in tangential $d\boldsymbol{\sigma}^t_{ij}$ and normal $d\boldsymbol{\sigma}^n_{ij}$ directions relative to the yield locus (figure 2.3), it appears that the tangential component of the stress vector gives a neutral loading condition, without associated plastic deformation (case of purely plastic material). In contrast, the normal component will produce the plastic strain increment ($d\boldsymbol{\varepsilon}^p_{ij}$), which is perpendicular to the yield surface, and it can be expressed mathematically by:

$$d\boldsymbol{\varepsilon}_{ij}^{p} = d\lambda \frac{\partial g(\boldsymbol{\sigma}_{ij})}{\partial \sigma_{ij}} = \begin{cases} d\lambda = 0, & if \quad \phi < 0 \\ d\lambda > 0, & if \quad \phi = 0 \end{cases} \tag{2.9}$$

where $g(\boldsymbol{\sigma}_{ij})$ is the plastic potential function, $d\lambda$ is a constant that depends on the loading history, known as plastic multiplier and $\dfrac{\partial g(\boldsymbol{\sigma}_{ij})}{\partial \boldsymbol{\sigma}_{ij}}$ a vector normal to the yield surface at the considered loading point.

The principle of normality, called also associated flow rule (AFR), is illustrated in the principal $\sigma_1 - \sigma_2$ stress space (figure 2.3) and determines the flow direction.

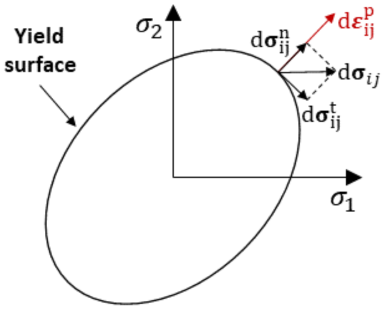

Figure 2.3: Representation of stress and plastic strain increment direction applied to the von Mises yield surface.

When an associated flow rule is adopted, the yield and the plastic potential surfaces are described by the same function, $f(\boldsymbol{\sigma}_{ij}) = g(\boldsymbol{\sigma})$, however, for some materials, their anisotropy cannot be well predicted. To overcome such a challenge, a non-associated flow rule (NAFR) is considered to enhance the accuracy of material behavior characterization [36]. For NAFR case, the yield and the plastic potential surfaces are described by different functions, $f(\boldsymbol{\sigma}) \neq g(\boldsymbol{\sigma})$. This subject will be reviewed in more detail in section 2.3.3 of this chapter.

In this section will be presented different plasticity criteria (isotropic and anisotropic) that can be used to model the material plastic behavior, proposed by several authors, highlighting the most relevant. Besides, it will be taken into consideration the conditions under which material passes from the elastic to the plastic state and the corresponding flow rules.

2.3.1 Isotropic yield criteria

A material that returns an identical stress state when requested by different strain paths (e.g., according to the rolling direction or transverse direction), is called isotropic material. The isotropy means that the material has the same properties regardless of the loading orientation. In the next following sections, some commonly used yield functions for isotropic materials are presented.

2.3.1.1 von Mises

The *von Mises* yield function [37], also known as the maximum distortion strain energy criterion, suggests that the yielding of materials begins when the second deviatoric stress invariant J_2 reaches a critical value.

When the material passes from an elastic state to a plastic state, the elastic energy of distortion reaches a critical value that is independent of the type of the stress state (isotropy). This comes from the relationship between J_2 and the elastic strain energy of distortion W_D.

$$W_D = J_2 \frac{1+\nu}{E} \tag{2.10}$$

In other words, the material starts to yield when *von Mises* stress reaches a critical value known as the yield strength (σ_y). The expression of *von Mises* function, considering the Cauchy stress tensor components, is:

$$2\phi(\boldsymbol{\sigma}) = (\sigma_{xx} - \sigma_{yy})^2 + (\sigma_{yy} - \sigma_{zz})^2 + (\sigma_{zz} - \sigma_{xx})^2 + 6\left(\sigma_{xy}^2 + \sigma_{yz}^2 + \sigma_{zx}^2\right) = \overline{\sigma_f}^2 \tag{2.11}$$

The equation 2.11 defines the yield surface as a circular cylinder (figure 2.4(a)) whose yield locus is a circle with radius $\sqrt{2/3}\sigma_y$ on the π-plane (figure 2.4(d)). Consequently, the plastic strain increments for the *von Mises* criterion, using the flow rule, can be given by the following explicit equation system:

$$\begin{bmatrix} d\varepsilon_x^p \\ d\varepsilon_y^p \\ d\varepsilon_z^p \\ d\gamma_{xy}^p \\ d\gamma_{yz}^p \\ d\gamma_{zx}^p \end{bmatrix} = d\lambda \frac{1}{2\overline{\sigma_f}} \begin{bmatrix} 2\sigma_x - \sigma_y - \sigma_z \\ 2\sigma_y - \sigma_z - \sigma_x \\ 2\sigma_z - \sigma_x - \sigma_y \\ 6\tau_{xy} \\ 6\tau_{yz} \\ 6\tau_{zx} \end{bmatrix} \tag{2.12}$$

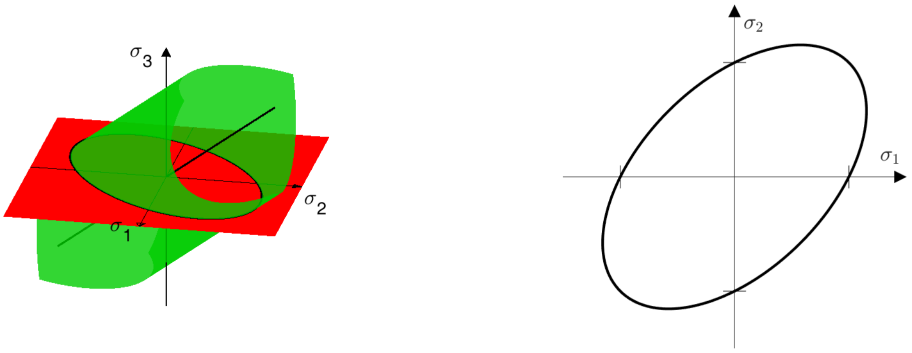

(a) Yield surface intersected by $\sigma_3 = 0$ plane (b) Yield surface projected in $\sigma_1 - \sigma_2$ plane

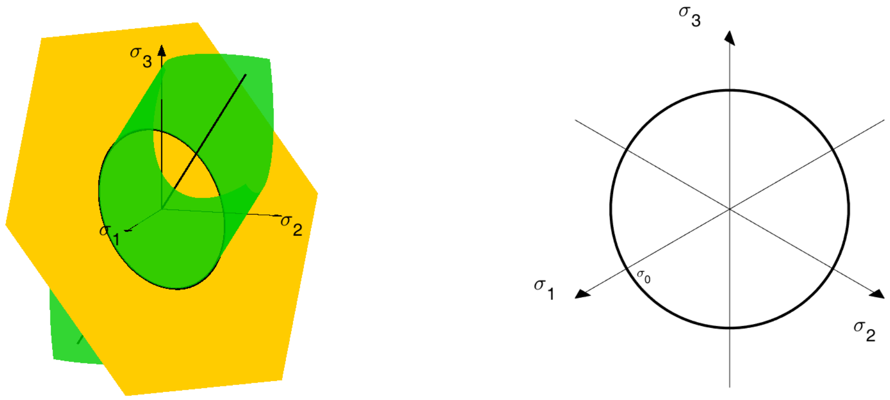

(c) Yield surface intersected by π-plane (d) von Mises yield surface in the π-plane

Figure 2.4: Yield surface of von Mises criterion.

This criterion needs only the elastic modulus, the Poisson ratio and the parameters for the isotropic hardening law, while a standard uniaxial tensile test is enough to obtain all the necessary data. Although the *von Mises* function is very valuable for isotropic plasticity, it has notable limitations since the plastic anisotropy is not taken into account and this model is not suitable for most of sheet metal materials.

2.3.1.2 Tresca

The Tresca [38] plasticity criterion considers that the plastic deformation starts when the maximum shear stress τ_{max} exceeds a critical value:

$$\tau_{max} = \frac{\sigma_1 - \sigma_3}{2} \tag{2.13}$$

where σ_1 and σ_3 are the principal stresses, with $\sigma_1 \geq \sigma_2 \geq \sigma_3$.

Replacing the previous equation 2.13 with the uniaxial condition ($\sigma_1 = \sigma_y$ and $\sigma_2 = \sigma_3 = 0$), the relationship between the value of the critical shear stress and the elastic limit (yield stress) of the uniaxial tensile test is given by:

$$\tau_{max} = \frac{\sigma_y}{2} \tag{2.14}$$

Actually, for the Tresca plasticity criterion, only the maximum and minimum principal stresses are responsible for the beginning of the plastic deformation, with the intermediate tension not having any influence on the yield locus. Generalizing the stresses of this analysis to the three-dimensional Haigh-Westergaard space, it appears that the intersection of the Tresca surface by a plane $\sigma_3 = 0$ gives a distorted hexagon, as shown in figure 2.5(b).

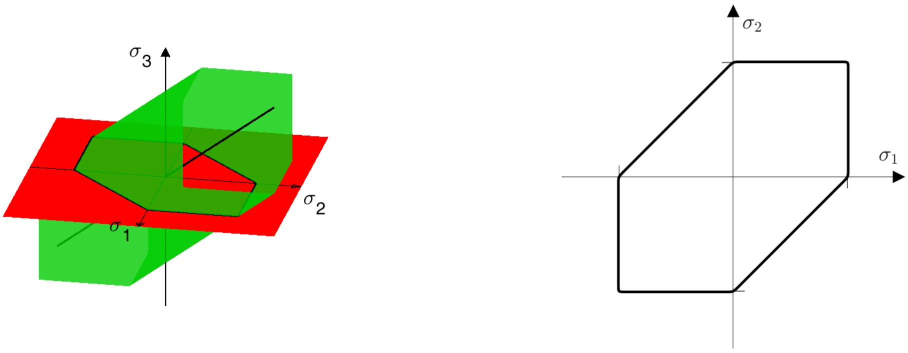

(a) Yield surface intersected by $\sigma_3 = 0$ plane

(b) Yield locus

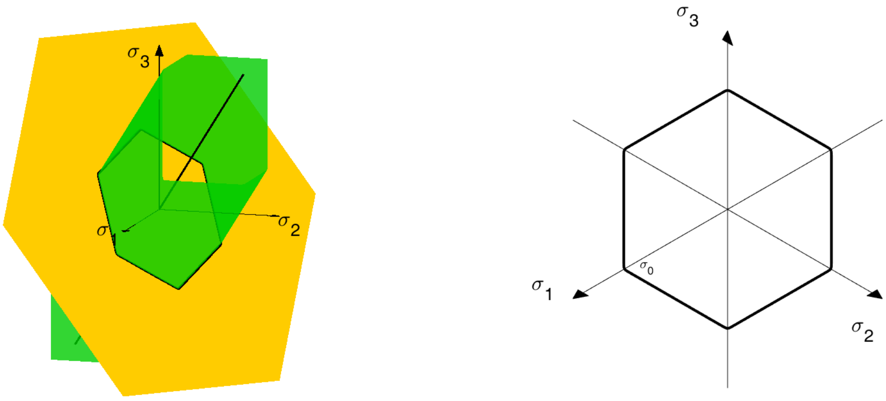

(c) Yield surface intersected by π-plane

(d) Tresca yield surface in the π-plane

Figure 2.5: Yield surface of Tresca criterion.

It is usual to refer that the Tresca plasticity criterion finds a phenomenological basis in the physical-metallurgical concepts of metallic materials. In fact, assuming that the crystalline network of these materials is formed by atomic planes superimposed on each other, it is easy to assume that, since the shear stresses are responsible for the dislocation of these planes, there must be a stress level above which the atoms of the network change their relative positions permanently (not recoverable). Even so, the phenomenological basis of the Tresca model can still be accepted, since the shear stresses are responsible for the dislocations and the change of the body shape.

2.3.1.3 Hershey

In 1954, Hershey [39] proposed a non-quadratic yield function, an evolution of the von Mises yield function, which is represented by the following expression:

$$\phi(\boldsymbol{\sigma}) = (\sigma_1-\sigma_2)^a + (\sigma_2-\sigma_3)^a + (\sigma_3-\sigma_1)^a = 2\overline{\sigma_f}^a \tag{2.15}$$

where a is a parameter determined based on the material crystallographic structure, and σ_1, σ_2 and σ_3 are the principal stresses.

The Hershey yield function is reduced to von Mises function when $a = 2$ and return the Tresca yield function for $a \to \infty$, as shown in figures 2.6 and 2.7. Since it is based on crystallographic structure, for a material with body-centered cubic (BCC) structures, the parameter $a = 6$ should be used and $a = 8$ for material with face-centered cubic (FCC) structures. Taking into consideration such assumption, the Hershey yield surface, usually, lies between von Mises and Tresca limits.

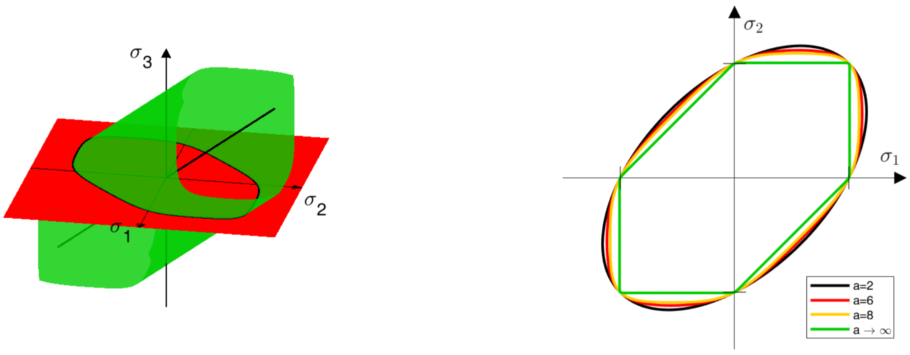

(a) Yield surface for a=8

(b) Projection in $\sigma_1 - \sigma_2$ plane for different values of parameter a

Figure 2.6: Yield surface and corresponding projection in $\sigma_1 - \sigma_2$ plane for Hershey criterion.

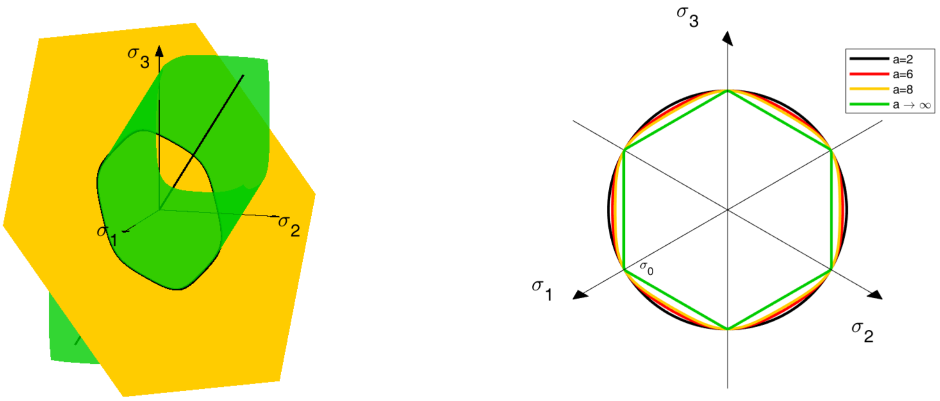

(a) Yield surface for a=8

(b) Projection in π-plane for different values of parameter a

Figure 2.7: Hershey yield surface represented in the π-plane.

2.3.2 Anisotropic yield criteria

The anisotropy behavior that is the variation of mechanical properties relative to the direction of loading application has been one of the leading research topics, par excellence, of the mechanical characterization of sheet metal materials used in forming processes.

Such property is influenced by several factors and considering in only metal sheets, has its main cause in cold-rolled and non-recrystallized materials, the heterogeneous plastic deformation induced during the manufacturing process, the crystallographic texture, the percentage of chemical elements and also the thermal and mechanical treatments to which the material was previously submitted.

The influence of anisotropy has been qualified and quantified through several parameters that characterize the distribution of deformations to which the material is requested. One of the most used parameters, which is standardized, is the plastic anisotropy coefficient r, defined by the ratio (equation 2.16) between the transverse strain (ε_2) relative to the loading direction (ε_1) and the thickness strain (ε_3). More recently, the plastic biaxial anisotropy coefficient r_b [40] was introduced, which relates the principal strains (ε_1 and ε_2) on the sheet plane (equation 2.17).

$$r = \frac{\varepsilon_2}{\varepsilon_3} = -\frac{\varepsilon_2}{\varepsilon_1 + \varepsilon_2} \tag{2.16}$$

$$r_b = \frac{\varepsilon_2}{\varepsilon_1} \tag{2.17}$$

One essential key of a yield function is the ability to describe and to predict the evolution of the plastic anisotropy coefficient, as well as the yield stress in the plane of the sheet metal. To evaluate this capability, it is possible to establish relations that define the dependence of the parameters mentioned above, with the angle θ, measured from the rolling direction and presented in the figure 2.8. It should be noted that the principal axes of the sheet, orthotropic axes, define three planes of symmetry. The existence of these symmetry planes makes it only necessary to determine the range from 0° to 90°.

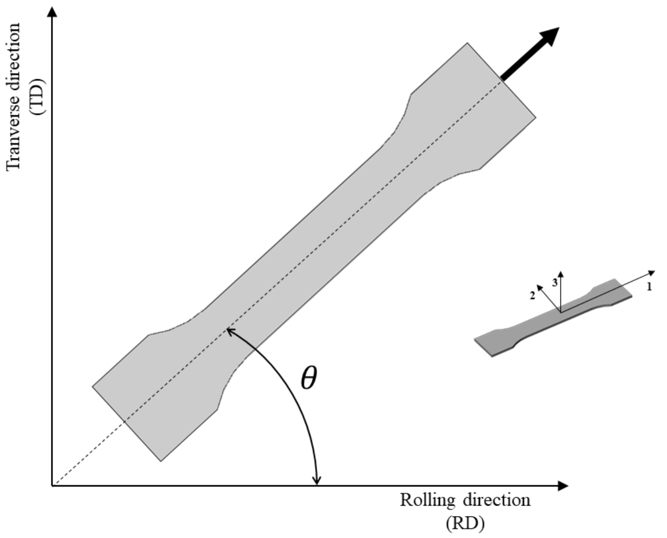

Figure 2.8: Relationship between the yield stress and the direction of loading in the plane of the sheet metal.

Defining σ_θ as the yield stress corresponding to the direction with the angle θ relative to the rolling direction, the tensor components for a uniaxial loading can be expressed as follows:

$$\begin{cases} \sigma_{xx} = \sigma_\theta \cdot cos^2\theta \\ \sigma_{yy} = \sigma_\theta \cdot sin^2\theta \\ \sigma_{xy} = \sigma_{yx} = \sigma_\theta \cdot cos\theta \cdot sin\theta \end{cases} \tag{2.18}$$

In the following sections, yield functions used to describe the anisotropic behavior of metal materials are presented.

2.3.2.1 Hill'48

In 1948, *Hill* introduced a generalization of the *von Mises* quadratic isotropic criterion for anisotropic materials [41]. When the axes of the coordinate system match with the axes of orthotropy, the yield criterion is given by the following equation:

$$\begin{aligned} 2\phi(\boldsymbol{\sigma}) = F(\sigma_{yy}-\sigma_{zz})^2 + G(\sigma_{zz}-\sigma_{xx})^2 + H(\sigma_{xx}-\sigma_{yy})^2 + \\ 2\left(L\cdot{\sigma_{yz}}^2 + M\cdot{\sigma_{zx}}^2 + N\cdot{\sigma_{xy}}^2\right) = \overline{\sigma_f}^2 \end{aligned} \tag{2.19}$$

where F, G, H, L, M e N are the material anisotropic parameters of *Hill 48'*, σ_{xx}, σ_{yy} and σ_{zz} are the stresses in the rolling direction (x), transversal direction (y) and in thickness direction (z), respectively, being σ_{xy}, σ_{yz} and σ_{zx} the shear stress components.

If $F = G = H = 0.5$ and $N = 1.5$, the *Hill' 48* criterion can be reduced to the *von Mises* criterion, assuming also $L = M = 1.5$.

For the plane stress state condition ($\sigma_{zz} = \sigma_{yz} = \sigma_{zx} = 0$), the yield criterion can be expressed as follows:

$$F\cdot\sigma_{yy}^2 + G\cdot\sigma_{xx}^2 + H(\sigma_{xx}-\sigma_{yy})^2 + 2\cdot N\cdot{\sigma_{xy}}^2 = \overline{\sigma_f}^2 \tag{2.20}$$

Applying the equation 2.9 to the yield criterion (equation 2.19), the following associations are obtained, relating the strain increment components with the stress components.

$$\begin{bmatrix} d\varepsilon_x^p \\ d\varepsilon_y^p \\ d\varepsilon_z^p \\ d\gamma_{xy}^p \\ d\gamma_{yz}^p \\ d\gamma_{zx}^p \end{bmatrix} = d\lambda \begin{bmatrix} H+G & -H & -G & 0 & 0 & 0 \\ -H & H+F & -F & 0 & 0 & 0 \\ -G & -F & G+F & 0 & 0 & 0 \\ 0 & 0 & 0 & 2N & 0 & 0 \\ 0 & 0 & 0 & 0 & 2L & 0 \\ 0 & 0 & 0 & 0 & 0 & 2M \end{bmatrix} \begin{bmatrix} \sigma_{xx} \\ \sigma_{yy} \\ \sigma_{zz} \\ \sigma_{xy} \\ \sigma_{yz} \\ \sigma_{zx} \end{bmatrix} \tag{2.21}$$

where $1/2\gamma_{ij} = \varepsilon_{ij}$.

If the established relationships in equation 2.18 and in equation 2.20 were taken into account, the effective stress can be expressed as:

$$\overline{\sigma_f}^2 = \sigma_\theta^2\left[F sin^4\theta + G cos^4\theta + H\left(cos^2\theta - sin^2\theta\right)^2 + 2\cdot N cos^2\theta\cdot sin^2\theta\right] \tag{2.22}$$

for the case of $\overline{\sigma_f} = \sigma_0$, the evolution of effective stress with the angle relative to the rolling direction comes:

$$\sigma_\theta = \sigma_0 \left[F sin^4\theta + G cos^4\theta + H \left(cos^2\theta - sin^2\theta\right)^2 + 2\cdot N cos^2\theta \cdot sin^2\theta\right]^{-\frac{1}{2}} \tag{2.23}$$

Following a similar procedure, the evolution of anisotropy coefficient with the orientation (angle relative to the rolling direction) of the sheet metal, assuming the volume consistency ($\varepsilon_{xx} + \varepsilon_{yy} + \varepsilon_{zz} = 0$), is translated as:

$$r_\theta = \frac{F sin^4\theta + G cos^4\theta + H \left(cos^2\theta - sin^2\theta\right)^2 + 2\cdot N cos^2\theta \cdot sin^2\theta}{F sin^2\theta + G cos^2\theta} - 1 \tag{2.24}$$

The method for *Hill' 48* criterion parameters identification is based on yield stresses using the equation 2.25 and assuming that G+H=1.

$$\begin{cases} F = \dfrac{\sigma_0^2}{2}\cdot\left(\dfrac{1}{\sigma_{90}^2} + \dfrac{1}{\sigma_b^2} - \dfrac{1}{\sigma_0^2}\right) \\[2ex] G = \dfrac{\sigma_0^2}{2}\cdot\left(-\dfrac{1}{\sigma_{90}^2} + \dfrac{1}{\sigma_b^2} + \dfrac{1}{\sigma_0^2}\right) \\[2ex] H = \dfrac{\sigma_0^2}{2}\cdot\left(\dfrac{1}{\sigma_{90}^2} - \dfrac{1}{\sigma_b^2} + \dfrac{1}{\sigma_0^2}\right) \\[2ex] N = \dfrac{1}{2}\cdot\dfrac{\sigma_0^2}{\tau_{xy}^2} \end{cases} \tag{2.25}$$

where σ_0 and σ_{90} are the angles 0° and 90°, relative to the rolling direction, respectively; σ_b the biaxial yield stress (for thin metal sheets it is very difficult to measure the tensile yield stress in the through-thickness direction) and τ_{xy} the yield stress obtained from a shear test.

Several authors started to use another approach for the calculation of the parameter N by using the yield stress σ_{45}, as expressed in equation 2.26. This method is used due to the difficulty in carrying out and obtaining data from shear tests.

$$N = \frac{\sigma_0^2}{2} \cdot \left(\frac{4}{\sigma_{45}^2} - \frac{1}{\sigma_b^2} \right) \tag{2.26}$$

Another method used for the identification of the Hill'48 parameters and commonly applied, is based on the plastic anisotropy coefficients, for 0°, 45° and 90°, relative to the rolling direction, i.e., r_0, r_{45} e r_{90}, respectively. The identification of the parameters is given by:

$$G + H = 1 \Rightarrow G = \frac{1}{r_0 + 1}; \quad \frac{H}{G} = r_0; \quad F = \frac{H}{r_{90}}; \quad N = (F + G)\left(r_{45} + \frac{1}{2}\right) \tag{2.27}$$

With this yield function it is also possible to predict the behavior for a biaxial stress state, in which the yield stress and the biaxial anisotropy coefficient are given by:

$$\begin{cases} \sigma_b = \sigma_0 \sqrt{\frac{1}{F+G}} \\ \\ r_b = \frac{F}{G} \end{cases} \tag{2.28}$$

2.3.2.2 Yld'89

The yield criterion *Yld89*, proposed by *Barlat and Lian* [42], is restricted to the modelling of the anisotropy associated with plane stress states, being the *Yld89* criterion given by the following equation:

$$\phi(\boldsymbol{\sigma}) = a|K_1 + K_2|^M + a|K_1 - K_2|^M + c|2 \cdot K_2|^M = 2\overline{\sigma_f}^M \tag{2.29}$$

where K_1 and K_2 are variables based on stress tensor components, $\overline{\sigma_f}$ the equivalent stress obtained from the yield function and M is an integer exponent, having the same meaning as the coefficient a used in equation 2.15 by *Hershey*, who concluded that the best approximation of the yield surface was given by $M = 6$ for BCC materials and $M = 8$ for FCC materials [43].

The variables K_1 and K_2 can be obtained from:

$$\begin{cases} K_1 = \frac{\sigma_{xx}+h\cdot\sigma_{yy}}{2} \\ \\ K_2 = \sqrt{\left(\frac{\sigma_{xx}-h\cdot\sigma_{yy}}{2}\right)^2 + (p\cdot\sigma_{xy})^2} \end{cases} \tag{2.30}$$

where the coefficients a, c, h and p are material parameters and can be identified using the anisotropy coefficients (equation 2.31), but also using the yield stress in different directions relative to the rolling direction (equation 2.32).

$$a+c=2; \quad c=2\sqrt{\frac{r_0\cdot r_{90}}{(1+r_0)(1+r_{90})}}; \quad h=\sqrt{\frac{r_0}{r_{90}}\cdot\frac{(1+r_0)}{(1+r_{90})}} \tag{2.31}$$

$$a+c=2 \quad (for \quad \overline{\sigma_f}=\sigma_0); \quad a=2\frac{\left(\frac{\sigma_0}{\tau}\right)^M-(1-h)^M}{1+h^M-(1-h)^M}; \quad h=\frac{\sigma_0}{\sigma_{90}} \tag{2.32}$$

where p, for stress based identification method, is given by:

$$p=\frac{\sigma_0}{\tau}\left(\frac{2}{2a-2^M c}\right)^{\left(\frac{1}{M}\right)} \tag{2.33}$$

The strain increment components of Yld'89 criterion are identified using the same methodology present in Hill'48 criterion, and can be written as:

$$
\begin{aligned}
d\varepsilon_{xx}^{p} = d\lambda \frac{\partial \phi(\boldsymbol{\sigma})}{\sigma_{xx}} = d\lambda M \Bigg[& a\left(K_1 - K2\right)\left|K_1 - K2\right|^{M-2}\left(\frac{1}{2} - \frac{\sigma_{xx} - h\sigma_{yy}}{4K_2}\right) \\
& + a\left(K_1 + K2\right)\left|K_1 + K2\right|^{M-2}\left(\frac{1}{2} + \frac{\sigma_{xx} - h\sigma_{yy}}{4K_2}\right) \\
& + 2^{M} c K_2^{M-1} \frac{\sigma_{xx} - h\sigma_{yy}}{4K_2} \Bigg]
\end{aligned}
$$

$$
\begin{aligned}
d\varepsilon_{yy}^{p} = d\lambda \frac{\partial \phi(\boldsymbol{\sigma})}{\sigma_{yy}} = d\lambda M \Bigg[& a\left(K_1 - K2\right)\left|K_1 - K2\right|^{M-2}\left(\frac{h}{2} + h\frac{\sigma_{xx} - h\sigma_{yy}}{4K_2}\right) \\
& + a\left(K_1 + K2\right)\left|K_1 + K2\right|^{M-2}\left(\frac{h}{2} - h\frac{\sigma_{xx} - h\sigma_{yy}}{4K_2}\right) \\
& - 2^{M} c K_2^{M-1} h\frac{\sigma_{xx} - h\sigma_{yy}}{4K_2} \Bigg]
\end{aligned}
\tag{2.34}
$$

$$
\begin{aligned}
d\varepsilon_{xy}^{p} = d\lambda \frac{\partial \phi(\boldsymbol{\sigma})}{\sigma_{xy}} = d\lambda M \Big\{ & \left[\left(K_1 + K2\right)\left|K_1 + K2\right|^{M-2} - a\left(K_1 - K2\right)\left|K_1 - K2\right|^{M-2} \right. \\
& \left. + 2^{M} c K_2^{M-1} p^{2} \frac{\sigma_{xy}}{2K_2} \right]
\end{aligned}
$$

To described the evolution of yield stresses for different orientations relative to the rolling direction of the material, first, the variables K_1 and K_2 must be rearranged using the relations of equation 2.18 and equation 2.30, giving the following expressions:

$$
\begin{cases}
K_1 = \frac{\sigma_\theta \cdot cos^2\theta + h \cdot \sigma_\theta \cdot sin^2\theta}{2} \\
\\
K_2 = \sqrt{\left(\frac{\sigma_\theta \cdot cos^2\theta - h \cdot \sigma_\theta \cdot sin^2\theta}{2}\right)^2 + \left(p \cdot \sigma_\theta \cdot cos\theta \cdot sin\theta\right)^2}
\end{cases}
\tag{2.35}
$$

Since σ_θ is common for both parameters, a variable change is possible in order to simplify the equation 2.29 as a function of the equivalent stress for different angles relative to the rolling direction . In this way, the transformation takes the following form:

$$\begin{cases} K_1 = \sigma_\theta \cdot S_1 \Rightarrow S_1 = \frac{cos^2\theta + h \cdot sin^2\theta}{2} \\ \\ K_2 = \sigma_\theta \cdot S_2 \Rightarrow S_2 = \sqrt{\left(\frac{cos^2\theta - h \cdot sin^2\theta}{2}\right)^2 + (p \cdot cos\theta \cdot sin\theta)^2} \end{cases} \tag{2.36}$$

Applying the equation 2.36 in the equation 2.29, it is possible to obtain an expression for the determination of effective stress with the angle relative to the rolling direction, assuming that $\overline{\sigma_f} = \sigma_0$.

$$\begin{aligned} 2\sigma_0^M = & \ \sigma_\theta^M \cdot \left[a|S_1 + S_2|^M + a|S_1 - S_2|^M + c|2 \cdot S_2|^M\right] \Leftrightarrow \\ \Leftrightarrow \sigma_\theta = & \ \sigma_0 \cdot \left(\frac{2}{a|S_1 + S_2|^M + a|S_1 - S_2|^M + c|2 \cdot S_2|^M}\right)^{\frac{1}{M}} \end{aligned} \tag{2.37}$$

The same methodology is applied to predict the evolution of anisotropy plastic coefficient with the orientation of the sheet metal. Taking into consideration the equations 2.16 and 2.34 the following expression is retrieved:

$$r_\theta = -\frac{R_2}{R_1 + R_2} \tag{2.38}$$

where R_1 e R_2 are obtained by the following form:

$$\begin{cases} R_1 = d\varepsilon_{xx}^p \cdot cos^2\theta + d\varepsilon_{yy}^p \cdot sin^2\theta + 2d\varepsilon_{xy}^p \cdot sin\theta \cdot cos\theta \\ \\ R_2 = d\varepsilon_{xx}^p \cdot sin^2\theta + d\varepsilon_{yy}^p \cdot cos^2\theta - 2d\varepsilon_{xy}^p \cdot sin\theta \cdot cos\theta \end{cases} \tag{2.39}$$

Note that the plastic multiplier ($d\lambda$) and coefficient M present in equation 2.34 are simplified and not used in the equation 2.39, because they are equal and common factors in the numerator and denominator. Additionally, the variables K_1 and K_2 present also the in equation 2.34 can be replaced by S_1 and S_2 since σ_θ is also simplified based on the same rule.

2.3.2.3 Yld'91

In 1991, Barlat *et al.* proposed an extension of Hershey's isotropic function, knows as Yld'91 function [44], which is a general 6 component yield criterion to describe the orthotropic anisotropy present in metallic materials. The Yld'91 non-quadratic function is given by:

$$\phi(\boldsymbol{\sigma}) = |S_1 - S_2|^m + |S_2 - S_3|^m + |S_3 - S_1|^m = 2\overline{\sigma_f}^m \tag{2.40}$$

where S_1, S_1 and S_3 are the principal values of the isotropic equivalent stress tensor $\boldsymbol{S}$ and the exponent m recommend to be equal to 6 or 8 for BCC and FCC materials, respectively.

The stress tensor $\boldsymbol{S}$ is defined by a linear transformation $\boldsymbol{L}$ applied on the Cauchy stress tensor $\boldsymbol{\sigma}$, such that:

$$\boldsymbol{S} = \boldsymbol{L} \cdot \boldsymbol{\sigma} \Leftrightarrow \begin{bmatrix} S_{xx} \\ S_{yy} \\ S_{zz} \\ S_{yz} \\ S_{zx} \\ S_{xy} \end{bmatrix} = \frac{1}{3} \begin{bmatrix} c+b & -c & -b & 0 & 0 & 0 \\ -c & a+c & -a & 0 & 0 & 0 \\ -b & -a & b+a & 0 & 0 & 0 \\ 0 & 0 & 0 & f & 0 & 0 \\ 0 & 0 & 0 & 0 & g & 0 \\ 0 & 0 & 0 & 0 & 0 & h \end{bmatrix} \cdot \begin{bmatrix} \sigma_{xx} \\ \sigma_{yy} \\ \sigma_{zz} \\ \sigma_{yz} \\ \sigma_{zx} \\ \sigma_{xy} \end{bmatrix} \tag{2.41}$$

where a, b, c, f, g and h are the anisotropic material coefficients.

The principal values of $\boldsymbol{S}$ can be obtained from the determination of the eigenvalues or using the following approach:

$$\begin{cases} S_1 = 2\sqrt{I_2} cos\left(\dfrac{\theta}{3}\right) = z^{\frac{1}{3}} + \overline{z}^{\frac{1}{3}} \\ \\ S_2 = 2\sqrt{I_2} cos\left(\dfrac{\theta}{3} - \dfrac{2\pi}{3}\right) = w \cdot z^{\frac{1}{3}} + \overline{w} \cdot \overline{z}^{\frac{1}{3}} \\ \\ S_3 = 2\sqrt{I_2} cos\left(\dfrac{\theta}{3} + \dfrac{2\pi}{3}\right) = \overline{w} \cdot z^{\frac{1}{3}} + w \cdot \overline{z}^{\frac{1}{3}} \end{cases} \tag{2.42}$$

where

$$\begin{cases} \theta = arccos\left(\dfrac{I_3}{I_2^{3/2}}\right) \\ \\ z = I_3 + i\sqrt{I_2 - I_3} = I_2^{3/2}\left[cos(\theta) + isin(\theta)\right] \\ \\ w = e^{-2i\pi/3} \\ \end{cases} \tag{2.43}$$

The second (I_2) and third (I_3) stress invariants are given by:

$$\begin{aligned} I_2 &= \frac{S_{xx}^2 + S_{yy}^2 + S_{zz}^2 + 2\left(S_{yz}^2 + S_{zx}^2 + S_{xy}^2\right)}{6} \\ I_3 &= \frac{S_{xx}S_{yy}S_{zz} + 2S_{yz}S_{zx}S_{xy} - \left(S_{xx}S_{yz}^2 + S_{yy}S_{zx}^2 + S_{zz}S_{xy}^2\right)}{2} \end{aligned} \tag{2.44}$$

For the prediction of equivalent stress evolution with the angle relative to the rolling direction, the following expression can be considered:

$$\sigma_\theta = \sigma_0 \cdot \left(\frac{|S_1 - S_2|^m + |S_2 - S_3|^m + |S_3 - S_1|^m}{2}\right)^{-\frac{1}{m}} \tag{2.45}$$

The strain increment components, necessary for the representation of the plastic anisotropy coefficient as a function of the orientation angle (like equation 2.38 using equation 2.39), result from the derivatives of the yield function in relation to the stress tensor components, expressed as:

$$\phi\left(\boldsymbol{\sigma}\right) = 2\overline{\sigma_f}^m \Longrightarrow \frac{\partial \overline{\sigma_f}}{\partial \sigma_{ij}} = \frac{1}{2m \cdot \overline{\sigma_\theta}^{m-1}} \frac{\partial \phi}{\partial \sigma_{ij}} \tag{2.46}$$

where:

$$\frac{\partial \phi}{\partial \sigma_{ij}} = \sum_{k=1}^{3} \sum_{l=2}^{3} \sum_{m=1}^{6} \frac{\partial \phi}{\partial S_k} \frac{\partial S_k}{\partial I_l} \frac{\partial I_l}{\partial s_m} \frac{\partial s_m}{\partial \sigma_{ij}} \tag{2.47}$$

2.3.2.4 CPB06

Cazacu *et al.* [45] proposed a plasticity criterion with a special focus on materials with a hexagonal compact (HC) structure. The yield function, designated as CPB06, allows the description of the stress differential phenomenon and is given by:

$$\phi\left(\boldsymbol{\sigma}\right) = \left(|\Sigma_1| - k\Sigma_1\right)^a + \left(|\Sigma_2| - k\Sigma_2\right)^a + \left(|\Sigma_3| - k\Sigma_3\right)^a = K \tag{2.48}$$

where k is a material parameter that describes the effect of stress differential, the parameter a is integer and positive, which allows greater flexibility to this criterion, and Σ_1, Σ_2 and Σ_3 are the eigenvalues of the transformed tensors ($\boldsymbol{\Sigma} = \boldsymbol{C} \cdot \boldsymbol{\sigma}$), being C_{ij} the anisotropic material parameters.

The physical meaning of the material parameter k can be obtained from uniaxial tests. In fact, according to the proposed criterion, it is expressed by the ratio between uniaxial tensile (σ_t) and uniaxial compression (σ_c) yield stresses as:

$$k = \frac{1-h}{1+h} \quad being \quad h = \left[\frac{2^a - 2\left(\dfrac{\sigma_t}{\sigma_c}\right)^a}{\left(2\dfrac{\sigma_t}{\sigma_c}\right)^a - 2}\right]^{\frac{1}{a}} \tag{2.49}$$

For any integer value of a and $k = 0$, there is no difference between the response in tension or compression. In particular, for $a = 2$ and $k = 0$, this criterion is reduced to the von Mises criterion.

The principal values of Σ, for a thin sheet case, are determined using the following expressions:

$$\begin{aligned}
\Sigma_1 &= \frac{1}{2}\left(\Sigma_{xx} + \Sigma_{yy} + \sqrt{\left(\Sigma_{xx} + \Sigma_{yy}\right)^2 + 4\Sigma_{xy}^2}\right) \\
\Sigma_2 &= \frac{1}{2}\left(\Sigma_{xx} + \Sigma_{yy} - \sqrt{\left(\Sigma_{xx} + \Sigma_{yy}\right)^2 + 4\Sigma_{xy}^2}\right) \\
\Sigma_3 &= \Sigma_{zz}
\end{aligned} \tag{2.50}$$

where

$$\begin{aligned}
&\Sigma_{xx} = \frac{1}{3}\Big[(2\cdot C_{11} - C_{12} - C_{13})\,\sigma_{xx} + (-C_{11} + 2\cdot C_{12} - C_{13})\,\sigma_{yy}\Big] \\
&\Sigma_{yy} = \frac{1}{3}\Big[(2\cdot C_{12} - C_{22} - C_{23})\,\sigma_{xx} + (-C_{12} + 2\cdot C_{22} - C_{23})\,\sigma_{yy}\Big] \\
&\Sigma_{zz} = \frac{1}{3}\Big[(2\cdot C_{13} - C_{23} - C_{33})\,\sigma_{xx} + (-C_{11} + 2\cdot C_{12} - C_{13})\,\sigma_{yy}\Big] \\
&\Sigma_{xy} = C_{66}\cdot\sigma_{xy}
\end{aligned} \tag{2.51}$$

The yield function expressed in equation 2.48 can be reduced to the yield stress (σ_0), obtained from the uniaxial tensile test along rolling direction, being also a reference value for the equivalent stress using the following form:

$$\sigma_0 = \left[\frac{K}{(|\Phi_1| - k\Phi_1)^a + (|\Phi_2| - k\Phi_2)^a + (|\Phi_3| - k\Phi_3)^a}\right]^{\frac{1}{a}} \tag{2.52}$$

where the constants of $\Phi_{1,2,3}$ can be calculated from:

$$\begin{aligned}
&\Phi_1 = \frac{1}{3}(2\cdot C_{11} - C_{12} - C_{13}) \\
&\Phi_2 = \frac{1}{3}(2\cdot C_{12} - C_{22} - C_{23}) \\
&\Phi 3 = \frac{1}{3}(2\cdot C_{13} - C_{23} - C_{33})
\end{aligned} \tag{2.53}$$

To predict the material yield stress (σ_θ) for different angles relative to the rolling direction, the equation 2.18 is applied into equation 2.55 and rearranging the equation 2.52 the following form is given:

$$\sigma_\theta = \sigma_0 \left[\frac{K}{(|\Phi_1| - k\Phi_1)^a + (|\Phi_2| - k\Phi_2)^a + (|\Phi_3| - k\Phi_3)^a}\right]^{-\frac{1}{a}} \tag{2.54}$$

considering for that

$$
\begin{aligned}
\Sigma_{xx} &= \frac{1}{3}\left[(2\cdot C_{11}-C_{12}-C_{13})\,cos\theta^2+(-C_{11}+2\cdot C_{12}-C_{13})\,sin\theta^2\right]\\
\Sigma_{yy} &= \frac{1}{3}\left[(2\cdot C_{12}-C_{22}-C_{23})\,cos\theta^2+(-C_{12}+2\cdot C_{22}-C_{23})\,sin\theta^2\right]\\
\Sigma_{zz} &= \frac{1}{3}\left[(2\cdot C_{13}-C_{23}-C_{33})\,cos\theta^2+(-C_{11}+2\cdot C_{12}-C_{13})\,sin\theta^2\right]\\
\Sigma_{xy} &= C_{66}\cdot sin\theta\cdot cos\theta
\end{aligned}
\tag{2.55}
$$

The strain increment components, necessary for the representation of the plastic anisotropy coefficient as a function of the orientation angle result from the derivatives of the yield function in relation to the stress tensor components, expressed as:

$$
d\varepsilon_{ij}^{p} = \frac{K_{\theta}^{\frac{1-a}{a}}}{a}\frac{\partial\phi}{\partial\sigma_{ij}} \tag{2.56}
$$

where:

$$
\frac{\partial\phi}{\partial\sigma_{ij}} = \sum_{k=1}^{3}\sum_{l=2}^{3}\sum_{m=1}^{6}\frac{\partial\phi}{\partial\sum_k}\frac{\partial sum_k}{\partial I_l}\frac{\partial I_l}{\partial s_m}\frac{\partial s_m}{\partial\sigma_{ij}} \tag{2.57}
$$

2.3.3 Non-associated flow rule - NAFR

In general, the development of plasticity criteria is based on the associated flow rule (AFR), in which the yield and plastic potential functions are identical and follow the assumption of normality, as shown in figure 2.9(a).

Of the implemented criteria in the numerical simulation of sheet metal forming processes, most are governed by the associated flow rule, and the results obtained show a good similarity with the experimental data. However, studies have shown that for some anisotropic materials, both steel and aluminum alloys, the accuracy of the plastic behavior prediction would need to be improved.

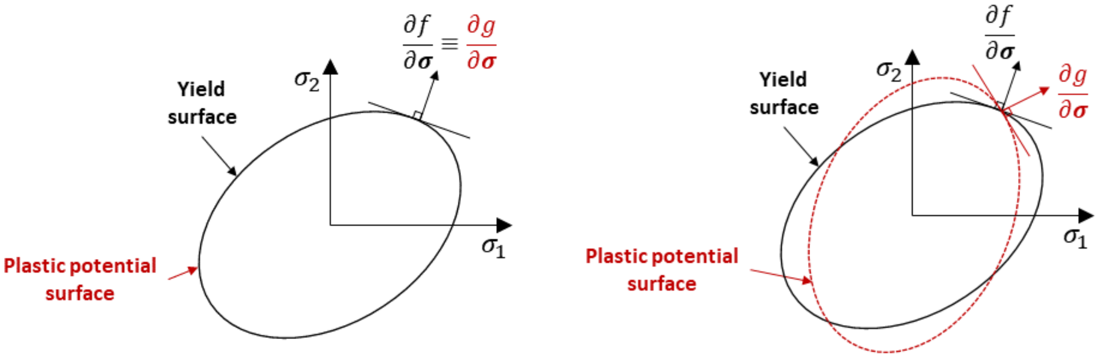

(a) Associated flow rule (b) Non-associated flow rule

Figure 2.9: Different types of plastic flow directionality.

This fact is due to the limitation of the AFR law in describing the yield stresses and the plastic anisotropic coefficients simultaneously through only one function, as shown in figure 2.10.

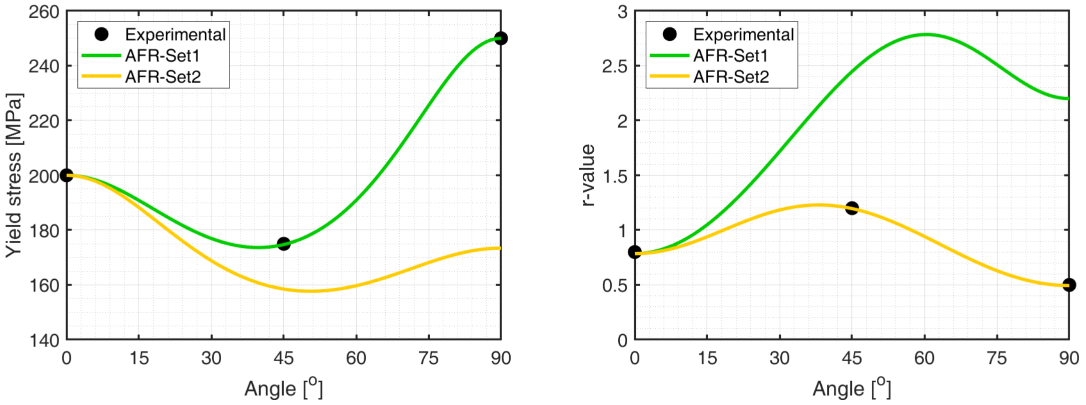

(a) Yield stresses (b) Plastic anisotropic coefficients

Figure 2.10: Prediction of the yield stresses and r-values for different orientations relative to the rolling direction based on AFR Hill'48 function using two sets of parameters

As seen in figure 2.10, the yield stresses are well modeled by the set of parameters *AFR-Set1*, but the plastic anisotropic coefficients are not correctly predicted. In the case of the *AFR-Set2*, the anisotropy coefficients are properly described, but the evolution of yield stresses does not show any agreement with the experimental points.

To overcome the challenge of modeling the anisotropic behavior of metallic materials with accuracy, some more advanced and sophisticated models have been proposed to predict the behavior of the material in these two aspects (yield stress and anisotropy coefficients) [40, 46, 47, 48]. Although the accuracy can be improved, the identification process of the parameters also becomes more complex, as more experimental data is needed, increasing the required work, verification time and the computational cost.

In order to overcome the limitations of the associated flow rule, recently, increasing attention has been given to the non-associated flow rule (NAFR), and several approaches have been proposed [36, 49, 50], where the yield surface and the plastic potential surface are described by two unrelated and independent functions (figure 2.9(b)). This approach allows the possibility of describing the material's behavior with higher accuracy, as shown in figure 2.11.

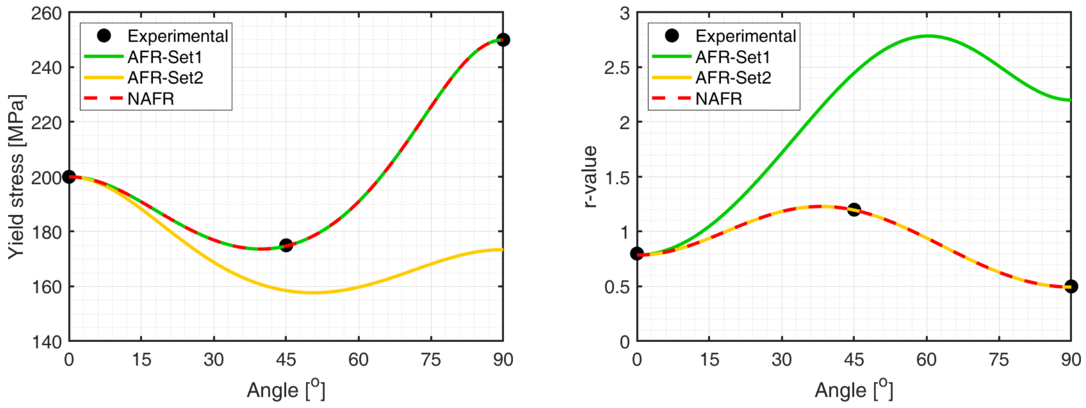

(a) Yield stresses

(b) Plastic anisotropic coefficients

Figure 2.11: Comparison of the yield stresses and r-values predictions for different orientations relative to the rolling direction based on AFR and NAFR Hill'48 function.

As seen from the predictions in figure 2.11, it is possible to describe both yield stresses and anisotropy coefficients. Since there are two functions for NAFR, the constitutive coefficients can also be separated, one set for the yield surface and another for the plastic potential surface. This independence provides a reduction in difficulty and complexity in the identification process of such parameters when compared with the AFR [36]. However, for both cases, the complexity of mathematical formulations increases with an increase in the constitutive model flexibility.

Figure 2.12 presents the integration scheme and variables identification process used in the formulation of NAFR.

Usually, for the AFR law the plastic multiplier is equal to the equivalent plastic strain increment ($\Delta\lambda = \Delta\bar{\varepsilon}^p$) and the following scheme can be used in a AFR formulation, assuming that $\frac{\partial\psi}{\partial\boldsymbol{\sigma}} = \frac{\partial\phi}{\partial\boldsymbol{\sigma}}$ and $\frac{g(\boldsymbol{\sigma})}{f(\boldsymbol{\sigma})} = 1$. Although, for the case of NAFR this does not happen anymore ($\Delta\lambda \neq \Delta\bar{\varepsilon}^p$ because $\frac{\partial\psi}{\partial\boldsymbol{\sigma}} \neq \frac{\partial\phi}{\partial\boldsymbol{\sigma}}$ and $\frac{g(\boldsymbol{\sigma})}{f(\boldsymbol{\sigma})}$ can take any positive value), so a more complex and precise approach is needed [50, 51], as expressed from equation 2.65 to 2.68. Finally, the consistency condition ensures that the stress state remains on the yield surface during plastic deformation.

1) Elastic predictor

i) Given an elastic trial strain $\varepsilon^e_{n+1} = \varepsilon^e_n + \Delta\varepsilon^e$, evaluate elastic trial stress:

$$\boldsymbol{\sigma}^{trial}_{n+1} = \boldsymbol{\sigma}_n + \boldsymbol{D} : \Delta\boldsymbol{\varepsilon}^e \tag{2.58}$$

ii) Check plastic consistency:

$$if \qquad \phi\left(\boldsymbol{\sigma}^{trial}_{n+1}, \overline{\varepsilon}^p_n\right) = f\left(\boldsymbol{\sigma}^{trial}_{n+1}\right) - \sigma_Y\left(\overline{\varepsilon}^p_n\right) \leq 0 \tag{2.59}$$

$$\boldsymbol{\sigma}_{n+1} = \boldsymbol{\sigma}^{trial}_{n+1} \tag{2.60}$$

$$\overline{\varepsilon}^p_{n+1} = \overline{\varepsilon}^p_n \tag{2.61}$$

$$\boldsymbol{\varepsilon}^p_{n+1} = \boldsymbol{\varepsilon}^p_n \tag{2.62}$$

$$go \quad to \quad 3) \tag{2.63}$$

$$else \quad go \quad to \quad 2)$$

2) Plastic corrector by solving the system for the unknowns

i) Newton-Raphson method is computed for each step *i* as follow:

$$d\Delta\lambda = \frac{\phi\left(\boldsymbol{\sigma}_{n+1}, \overline{\varepsilon}^p_n\right)^i}{\left(\frac{\partial\phi}{\partial\boldsymbol{\sigma}} : \boldsymbol{D} : \frac{\partial\psi}{\partial\boldsymbol{\sigma}} + H\frac{g(\boldsymbol{\sigma})}{f(\boldsymbol{\sigma})}\right)^i_{n+1}} \tag{2.64}$$

$$\boldsymbol{\sigma}^{i+1}_{n+1} = \boldsymbol{\sigma}^i_{n+1} - d\Delta\lambda\left(\boldsymbol{D} : \frac{\partial\psi}{\partial\boldsymbol{\sigma}^i_{n+1}}\right) \tag{2.65}$$

$$\Delta\lambda^{i+1}_{n+1} = \Delta\lambda^i_{n+1} + d\Delta\lambda \tag{2.66}$$

$$\Delta\overline{\varepsilon}^p_{n+1} = \Delta\lambda^{i+1}_{n+1}\left(\frac{g(\boldsymbol{\sigma})}{f(\boldsymbol{\sigma})}\right)^i_{n+1} \tag{2.67}$$

$$\overline{\varepsilon}^{p(i+1)}_{n+1} = \overline{\varepsilon}^{p(i)}_{n+1} + \Delta\overline{\varepsilon}^p_{n+1} \tag{2.68}$$

$$if \qquad \phi\left(\boldsymbol{\sigma}^{i+1}_{n+1}, \overline{\varepsilon}^{p(i+1)}_{n+1}\right) \cong 0 \tag{2.69}$$

$$Update \quad variables$$

$$else \quad go \quad to \quad i)$$

3) Return

Figure 2.12: State update procedure for NAFR implementation.

2.4 Damage - models and criteria

Currently there is an emphasis on automobile industry related with weight reduction of automotive body, safety and vehicle fuel economy, due to restrictions on the environmental gas emissions [52]. To accomplish this goal, a new generation of materials is used. However, their lower formability in sheet forming operations, leading to premature fracture, is challenging the numerical simulation in prediction of such material behavior [53].

In the classic theory of plasticity, a hardening law combined with a plasticity criterion is enough to evaluated and analyze the behavior of a metallic component in any engineering area when subject to a loading condition that leads to a point before the material forming limit. However, for a stress state that leads to plastic deformation, above the limits of formability (e.g., strains higher than uniform deformation (beginning of necking) in the case of the uniaxial tensile), the changes that occur in the material microstructure are no longer negligible, playing an essential role in ductile fracture prediction.

The damage represents the physical process of a cumulative degradation of a material that can lead to its macroscopic collapse, which is related to the density of its internal defects. Such phenomenon is the result of the nucleation, growth and coalescence of voids present in the microstructure [53, 54]. The amount of degradation depends on the type of material, the loading condition that is subjected, its application, among other factors. In terms of macroscopic properties, the degradation is associated with the decrease of stiffness, strength and ductility, being indicators used to quantify the degradation level, as well as to calibrate constitutive model parameters applied in the prediction of the onset of damage and consequent fracture.

The numerical validation of critical strains in sheet metal forming processes is still very often based on the classic forming limit diagrams and such analysis cannot take into consideration the variation of strain paths and microscopic ductile damage behavior [55]. The scientific community has made an increasing effort to improve the understanding of the damage initiation phenomenon and the corresponding accumulation of ductile materials. In this context, several damage models have been proposed based on different approaches.

Recently, Stoughton and Yoon [56] described a new path independent failure criterion, based on the combination of stress-based FLD and Tresca's criterion, to predict necking and fracture in sheet metal forming processes, however, it still needs some improvements.

As alternative to previous approach, several damage models based on stress states are used to predict failure during the forming process [57, 58, 59]. Bai and Wierzbicki

[60, 61] studied and evaluated different groups of damage models, and classified them as empirical, physics based and phenomenological models. However, to measure experimentally internal damage variable is extremely challenging, therefore other variables are considered and the stress state can be characterized as a function of: triaxiality η, hydrostatic pressure p, and the Lode angle parameter $\overline{\theta}$ (figure 2.13).

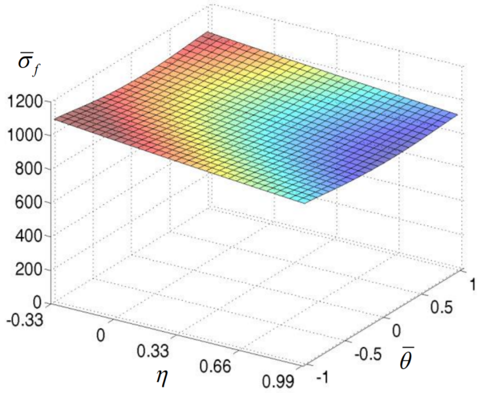

Figure 2.13: Equivalent stress as a function of triaxiality and Lode angle parameters.

Triaxiality is defined as the ratio between the mean stress (σ_m) and the equivalent stress ($\overline{\sigma}$) obtained from von Mises yield function:

$$\eta = \frac{\sigma_m}{\overline{\sigma}} \tag{2.70}$$

The hydrostatic pressure is defined as the opposite value of the mean stress ($p = -\sigma_m$). The Lode angle parameter is the ratio of the third and second stress tensor invariants or can be directly related to the normalized value of the third invariant of the deviatoric stress tensor using the following equation:

$$\overline{\theta} = 1 - \frac{2}{\pi} arccos(\xi) \quad , \quad with \quad \xi = \frac{3\sqrt{3}}{2} \frac{J_3}{(J_2)^{3/2}} \tag{2.71}$$

According to the previous definition, the Lode angle parameter varies between -1 (compression) and 1 (tension). For a plane stress case ($\sigma_3 = 0$), the Lode angle parameter is a function of the stress triaxiality (figure 2.14) [62] by:

$$\overline{\theta} = 1 - \frac{2}{\pi} arccos\left[-\frac{27}{2}\eta\left(\eta^2 - \frac{1}{2}\right)\right] \qquad for \quad -2/3 \leq \eta \leq 2/3 \tag{2.72}$$

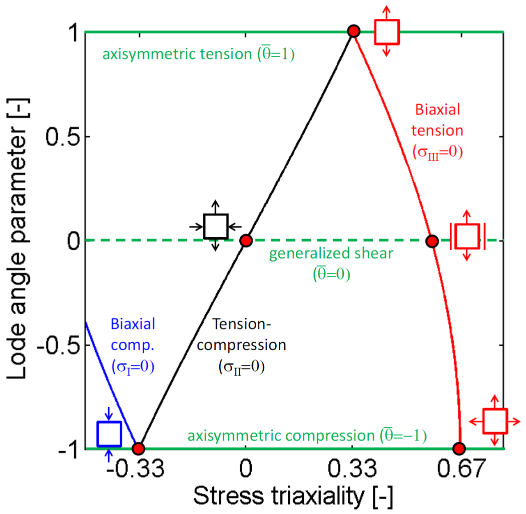

Figure 2.14: Lode angle parameter as a function of the stress triaxiality for plane stress conditions [62].

Constitutive models for damage prediction are predominantly applied to the manufacturing process design, but can also be used in the troubleshooting area, process safety and operative learning field. Unfortunately, the development of mathematical physics based constitutive models that are robust, accurate and precise, and at the same time fast and flexible, is still very challenging. Besides the classification announced by Bai and Wierzbicki [60], damage models can be divided into two main categories: coupled and uncoupled models.

In the case of coupled models, generally, some of the constitutive parameters have a physical meaning since they are related to properties and characteristics inherent to the material, which sometimes implies the need for more complex and challenging experimental tests to identify such parameters. On the other hand, in the case of uncoupled models, there is no direct physical relationship with the constitutive parameters, whose identification can be carried out through simple experimental tests (e.g., uniaxial tensile or bending tests). This is one of the main reasons that make uncoupled models interesting and frequently used, both in the sheet metal forming industry and in scientific researches.

In general, coupled damage models can be developed from physical or phenomenological observations. On the other hand, uncoupled damage models are generally empirical or also phenomenological based on observations. Nevertheless, as previously above, the level of accuracy and complexity of the models must always be adequately adjusted so that it is able to describe the behavior of a material for a given request.

2.4.1 Coupled models

In coupled damage models, both physics based or phenomenological, the degradation of the mechanical strength, also known as softening, is due to the presence of voids in the microstructure of ductile materials. These models are well-known in the scientific area, since it is possible to couple material plasticity with damage, and consequently, fracture.

For physics based models (e.g. GTN damage model), the influence of voids is commonly represented by the material porosity or void volume fraction. In other hand, phenomenological models (e.g. Lemaitre and Chaboche damage models) are usually related with the mean density of forces that actuate in the resistant area.

2.4.1.1 GTN

The model for the description of damage and fracture proposed by Gurson [63] was developed based on homogenization theory, considering spherical and cylindrical voids. To describe material degradation, a single microstructural variable is defined, the void volume fraction, which take into account the nucleation, growth and coalescence of voids during loading, as shown in figure 2.15.

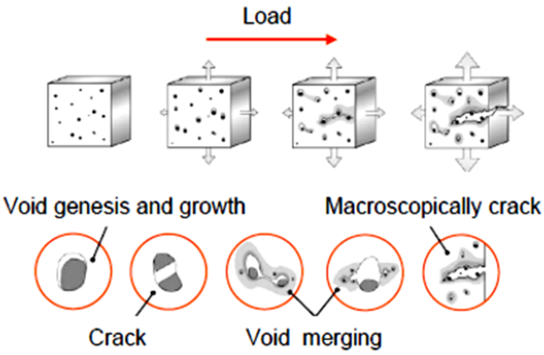

Figure 2.15: Schematic representation of the process of nucleation, growth and coalescence of voids [64].

Several improvements were proposed by many researchers, due to the restrictions of the original model, being the Tvergaard [65] and Needleman [66] contribution, known as GTN model, the most influential and regularly used. They modified the original porosity variable (f) to a new porosity parameter (f^*), which take into consideration the effect of void nucleation and coalescence process, which is triggered by constant f_c representing critical void volume fraction. The corresponding GTN damage model yield function is expressed by:

$$\phi = \left(\frac{\overline{\sigma}}{\sigma_Y}\right)^2 + 2q_1 f^* cosh\left(\frac{3}{2}q_2\frac{\sigma_H}{\overline{\sigma}}\right) - \left(1 + q_3 f^{*2}\right) \tag{2.73}$$

where q_1, q_2 and q_3 are model parameters, $\overline{\sigma}$ and σ_Y are the equivalent von Mises and flow stress, respectively, and σ_H the hydrostatic stress.

The modified porosity parameter f^* is calculated by:

$$f^* = \begin{cases} f & f \leq f_c \\ f_c + \dfrac{1/q_1 - f_c}{f_F - f_c}(f - f_c) & f > f_c \end{cases} \tag{2.74}$$

where f_F is the volume void fraction at fracture and f_c is the critical volume void fraction.

The evolution law of porosity is given by the sum $\dot{f} = \dot{f}_G + \dot{f}_N$, accounting for void growth rate $\dot{f}_G$ and nucleation $\dot{f}_N$, and each variable is expressed by:

$$\begin{aligned} \dot{f}_G &= (1 - f)\, tr\left(\dot{\boldsymbol{\varepsilon}}_p\right) \\ \dot{f}_N &= \frac{f_N}{S_N\sqrt{2\pi}} exp\left[-\frac{1}{2}\left(\frac{\dot{\varepsilon}_p - \varepsilon_N}{S_N}\right)^2\right]\dot{\varepsilon}_p \end{aligned} \tag{2.75}$$

where f_N is volume fraction, ε_N and S_N are the mean strain for void nucleation and corresponding standard deviation, while $\dot{\varepsilon}_p$ defines plastic strain rate and $tr\left(\dot{\boldsymbol{\varepsilon}}_p\right)$ the hydrostatic component of the plastic strain rate tensor.

Over the past decades, some improvements were made to the original Gurson or GTN constitutive models, to take into account effects such as the void size [67, 68], void shape [69], kinematic hardening [70], the micro voids shear localization [71, 72, 73], among others [74].

2.4.1.2 Lemaitre

To avoid a micromechanical approach Lemaitre damage model [54] adopts a thermodynamical framework and assumes the principle of strain equivalence, by substituting in the constitutive equations of the virgin material the Cauchy stress tensor $\boldsymbol{\sigma}$ by the effective stress tensor represented as:

$$\tilde{\boldsymbol{\sigma}} = \frac{\boldsymbol{\sigma}}{1-D} \tag{2.76}$$

where D is an a isotropic damage internal variable identified as an effective surface density of microdefects at the faces of a material representative volume element.

The damage variable D can assume values between 0 (undamaged state) and 1 (rupture of the element into two parts). The evolution law for the internal damage variable is defined as:

$$\dot{D} = \frac{\dot{\gamma}}{1-D}\left(\frac{Y}{S}\right)^{s} \tag{2.77}$$

where S is damage denominator and s is the damage exponent, being $\dot{\gamma}$ the plastic consistency parameter and Y the damage energy release rate, which can be given by:

$$Y = \frac{1}{2E\left(1-D\right)^{2}}\left[\left(1-\nu\right)\boldsymbol{\sigma}:\boldsymbol{\sigma} - \nu\left(tr\left(\boldsymbol{\sigma}\right)\right)^{2}\right] \tag{2.78}$$

where E and ν are the Young modulus and Poisson ratio, respectively.

2.4.2 Uncoupled models

Uncoupled damage models can connect failure with plastic behavior, although it is not possible in the opposite away. Like in coupled damage models, plasticity is also affected by the voids present in the material.

The basis of many uncoupled damage models, either empirical or phenomenological, is the stress triaxiality [75, 76], being a function of the strain at failure. The crack occurs when a critical strain value is reached, which is a result of the integral of a cumulative strain path function. This postulation became the origin of a series of proposed and regularly used constitutive damage models, being the damage initiation criteria the major difference between them.

These types of models can take into account shear fracture, being one fundamental attribute for sheet metal forming processes.

2.4.2.1 Johnson-Cook

As the plastic deformation proceeds, the damage model proposed by Johnson-Cook [77] takes into account the path dependency by accumulating damage. Due to their relative simplicity, this model uses a limited number of constants and strain at fracture $\overline{\varepsilon_f}$ is primarily dependent on stress triaxiality η, plastic strain rate $\dot{\varepsilon_p}$ and temperature θ. The general expression for the strain at fracture is given by:

$$\overline{\varepsilon_f} = \left(d_1 + d_2 \cdot e^{d_3 \eta}\right) \left[1 + d_4 ln \left(\frac{\dot{\varepsilon}_p}{\dot{\varepsilon}_0}\right)\right] (1 + d_5 \theta) \tag{2.79}$$

where d_1, d_2, d_3, d_4, d_5 are material parameters and where is evident the exponential dependence of the strain at fracture on triaxiality η, this one being defined as a function of hydrostatic stress and equivalent von Mises stress.

The criterion for failure is met when the following condition is satisfied:

$$D = \int \frac{\Delta \overline{\varepsilon}^p}{\overline{\varepsilon_f}} = 1 \tag{2.80}$$

being D the damage variable and $\Delta\varepsilon_p$ the equivalent plastic strain increment.

2.4.2.2 Hosford-Coulomb

Mohr and Marcadet [78] proposed a phenomenological ductile damage model applied to metallic materials, known as the Hosford-Coulomb model. Such model aims to predict ductile fracture in industrial practice, based on the assumption that the onset of fracture is imminent with the formation of a primary or secondary band of localization. In this ductile damage model, the strain at fracture is a function of triaxiality and Lode angle parameter, and it is expressed by:

$$\overline{\varepsilon_f} = b (1+c)^{\frac{1}{n}} \left(\{\frac{1}{2} [(f_1 - f_2)^a + (f_2 - f_3)^a + (f_3 - f_1)^a]\}^{\frac{1}{a}} + c (2\eta + f_1 + f_3) \right)^{-\frac{1}{n}} \tag{2.81}$$

The expressions given by f_i are trigonometric functions dependent on the Lode angle parameter, allowing the transformation of coordinates,

$$\begin{aligned} f_1 &= \frac{2}{3} cos\left[\frac{\pi}{6}\left(1-\overline{\theta}\right)\right] \\ f_2 &= \frac{2}{3} cos\left[\frac{\pi}{6}\left(3+\overline{\theta}\right)\right] \\ f_3 &= -\frac{2}{3} cos\left[\frac{\pi}{6}\left(1+\overline{\theta}\right)\right] \end{aligned} \tag{2.82}$$

where the Lode angle parameter lies within the triaxiality range of [-2/3 2/3] for a plane stress condition.

The Hosford-Coulomb ductile damage model has four parameters: a, b, c and n. Based on engineering experience, the authors propose to assume the exponent n equal to 0.1, since small adjustments of the parameters a and b can usually attenuate the effect of this guess on the strain to fracture. The parameters are directly related with experimental equivalent plastic strain to fracture values, using the following expressions:

$$\begin{aligned} \overline{\varepsilon_f}^{ST} &= b\left(\sqrt{3}\frac{1+c}{\left(1+2^{a-1}\right)^{\frac{1}{a}}}\right)^{\frac{1}{n}} \\ \overline{\varepsilon_f}^{UT} &= b \\ \overline{\varepsilon_f}^{PST} &= b\left(\sqrt{3}\frac{1+c}{\left(1+2^{a-1}\right)^{\frac{1}{a}}+2c}\right)^{\frac{1}{n}} \\ \overline{\varepsilon_f}^{BT} &= b \end{aligned}$$

Taking into account the previous relationships, parameter b is calculated directly using the $\overline{\varepsilon_f}^{UT}$ or $\overline{\varepsilon_f}^{BT}$ experimental values, then allowing the identification of parameter c, also using the $\overline{\varepsilon_f}^{ST}$ and $\overline{\varepsilon_f}^{PST}$ (equation 2.83). Parameter a must be identified based on an implicit iterative method using equation 2.84 and within the $1 \leq a \leq 2$ to guarantee uniqueness of the solution.

$$c = \frac{1 - \left(\frac{\overline{\varepsilon_f}^{PST}}{\overline{\varepsilon_f}^{ST}} \right)^n}{\frac{2}{\sqrt{3}} \left(\frac{\overline{\varepsilon_f}^{PST}}{b} \right)^n + \left(\frac{\overline{\varepsilon_f}^{PST}}{\overline{\varepsilon_f}^{ST}} \right)^n - 1} \tag{2.83}$$

$$\left(1 + 2^{a-1}\right)^{\frac{1}{a}} = \sqrt{3}\,(1+c) \left(\frac{b}{\overline{\varepsilon_f}^{ST}} \right)^n \tag{2.84}$$

(This page was deliberately left blank)

Chapter 3

Materials, characterization and formability

This chapter presents the proposed sheet metal materials, which were used for this research. Additionally, its mechanical characterization is defined, the corresponding constitutive models are used and the methodology to obtain its parameters. Adequate experimental tests are selected and performed, having in mind the validation and assessment of models which will be implemented and developed.

(This page was deliberately left blank)

3.1 Dual-phase steels - 500, 600 and 780 grades

In this research, advanced high strength steel (AHSS) produced by SSAB company were used, namely three grades of dual-phase (DP) steel sheets (DP500, DP600 and DP780), with an initial thickness of 0.8 mm. Table 3.1 lists the percentage of alloying elements present in each material chemical composition.

Table 3.1: Chemical composition [%] of the dual-phase steels: DP500, DP600 and DP780.

Material	C	Si	Mn	P	S	Cr	Ni	Mo	V	Ti	Cu	Al	Nb	B	N	EC[1]
DP500	0.079	0.31	0.65	0.003	0.003	0.03	0.03	0.0	0.01	0.0	0.01	0.038	0.0	0.0003	0.003	0.20
DP600	0.089	0.20	0.85	0.014	0.004	0.03	0.03	0.0	0.01	0.0	0.01	0.046	0.019	0.0003	0.004	0.24
DP780	0.138	0.20	1.52	0.011	0.002	0.03	0.03	0.0	0.02	0.0	0.01	0.038	0.014	0.0002	0.003	0.40

The alloy elements in dual-phase steels have different types of purposes. Carbon (C) strengthens the martensite and determines the phase distribution, also acting as an austenite stabilizer. Silicon (Si) promotes ferrite transformation and manganese (Mn) is a ferrite solid solution strengthener. Additionally, micro-alloying elements such as Vanadium (V) or Nitrogen (N) can be used as precipitation strengtheners, but also in the refinement of the microstructure. The small amount of Nb in the DP600 and DP780 materials promotes finer grains and a more homogeneous distribution on DP microstructure, resulting in a higher strength and better ductility [79].

To visualize the microstructure of the dual-phase steels, a scanning electron microscopy (SEM) was performed in the material samples. The microstructures of these steels observed by SEM are shown in figure 3.1. Additionally, table 3.2 presents the average grain size values of the ferrite and the percentage of martensite content for each dual-phase steel, determined from microstructural observations.

Table 3.2: Average size of ferritic grains (D) and volume percentage of martensite (V_M) for the initial materials

Material	D [μm]	V_M [%]
DP500	21.8	13
DP600	10.1	18
DP780	5.9	25

---

[1] $EC = C + \frac{Mn}{6} + \frac{Ni+Cu}{15} + \frac{Cr+Mo+V}{5}$

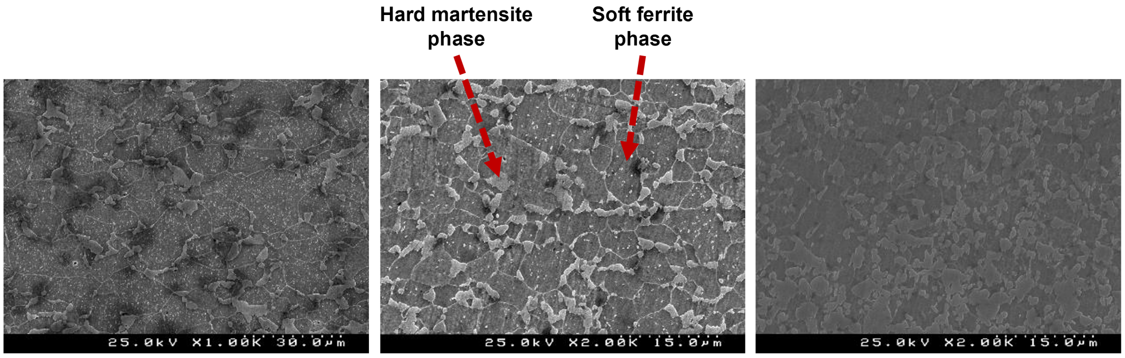

(a) DP500 (b) DP600 (c) DP780

Figure 3.1: Initial microstructure obtained from SEM of the dual-phase steels.

As seen in the figure 3.1 and listed in table 3.2, the dual-phase steels present a soft ferrite matrix with small islands of martensite particles (lighter areas). From DP500 to DP780, the average grain size decreases (22, 10 and 6 μm respectively) and in an opposite way, the volume fraction of martensite content increases, from 13% to 21% and 37%, respectively.

Such values indicate that DP500 should be the material with higher ductility but lower strength. In contrast, DP780 shall be the steel with higher strength, but its ductility shall be compromised due to the smaller ferrite grain size.

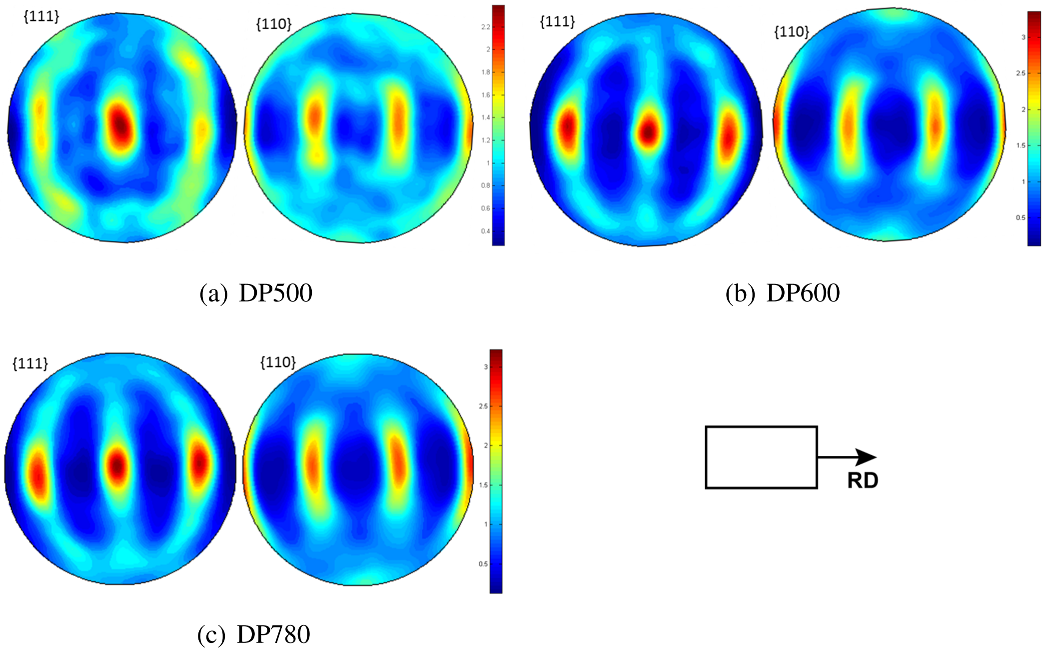

(a) DP500 (b) DP600

(c) DP780

Figure 3.2: Experimental pole figures {111} and {110} from initial materials; RD - rolling direction of the sheet.

Pole figures from ferritic grains obtained by EBSD (Electron backscatter diffraction) show the existence of a γ fiber (111<uvw>) type crystallographic texture with a reinforcement of the 111<110> component (figure 3.2), which is typical of rolled steel sheets [80].

In the following sections, a detailed description and analysis of material behavior is performed.

3.2 Mechanical characterization

This section gives the description of the experimental test methodologies employed for the mechanical characterization of the three grades of dual-phase steel.

Different types of mechanical tests have been performed in order to study and obtain different material properties. Monotonic uniaxial tensile and compression tests were conducted at various loading orientation to the sheet rolling direction. The anisotropic plastic coefficients (r-values) were also determined for the same loading conditions of tensile tests. Additionally, hydraulic bulge tests and stacked disc compression tests were performed to obtain the biaxial stress-strain flow curve and the biaxial anisotropy, respectively.

Each one of these experimental tests has been performed at least three times, except the compression tests, thus leading to more than 200 tests in total. Yet, depending on the complexity of the elasto-plastic constitutive models, only a fraction of these tests are needed to completely identify and model the material behavior. Also, the goals to perform such amount of trials include the validation of hardening models and the improvement of description of the plastic anisotropy, in addition to ensuring repeatability of the results or understanding their dispersion.

3.2.1 Uniaxial tensile test

The uniaxial tensile test is a standard experimental test and the one used to determine the fundamental mechanical properties of materials. Within these properties, the most relevant are the modulus of elasticity (E), coefficient of Poisson (ν), yield stress of the material (Re or $Rp_{0.2}$), ultimate tensile strength (Rm), elongation after rupture (A), as well as, the anisotropy coefficients of the material (important property in case of metal sheets, due to the manufacturing process).

Uniaxial tensile tests are usually performed monotonically until the fracture of material, at a constant strain rate. However, it is possible to perform the test at different strain rates and different stress states, using strategies such as multiple loading cycles and relaxation periods to capture and characterize a specific behavior of the material.

The experimental test is performed at a constant speed, which will lead to an increase of the applied force to the specimen (material hardening) with increasing elongation. The evolution of the material elongation shall be recorded by the extensometer placed in the area of the useful length of the specimen that is being tested.

3.2.1.1 Stress-strain flow curves

The tensile tests for the selected materials were performed according to ASTM E8M [81]. Five different loading conditions were defined, i.e., different directions relative to the rolling direction (0^o, 22.5^o , 45^o , 67.5^o and 90^o). The geometry of the specimens was obtained by machining a rectangular strip. The experimental conditions of the test are given in table 3.3.

Table 3.3: Experimental conditions of uniaxial tensile tests.

Loading directions	5
Number of experiments for each direction	3
Crosshead speed (grip)	5 mm/min
Data acquisition	20 Hz
Clip gage initial length - l_0	50 mm
Temperature	23 ^{o}C
Relative humidity	56%

The specimens were tested at room temperature with a constant crosshead speed, resulting in an initial strain rate on the order of $1e^{-3}$ s^{-1}, until the material rupture on a 100 kN hydraulic testing machine (MTS 810). For the acquisition of elongation in the uniform section of the specimen, and therefore measurement of corresponding strains, an extensometer with an initial length of 50 mm was used. In order to guarantee the repeatability of the results, several tests were performed for each material and loading direction, making a total of 45 tests. For a clear and easier analysis of the stress-strain flow curves obtained from the performed uniaxial tensile tests, only one result for each loading direction is shown in figure 3.3. All data can be consulted in the appendix A, where the 45 obtained tests results are plotted and repeatability observed.

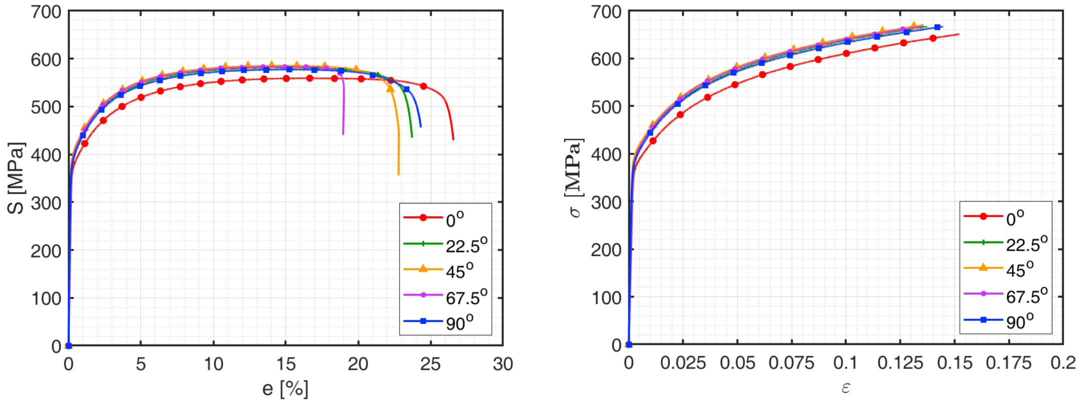

(a) DP500

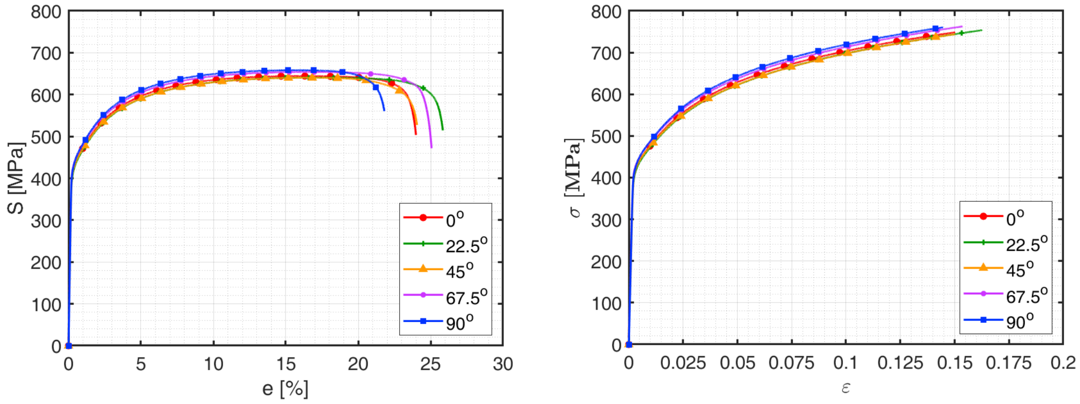

(b) DP600

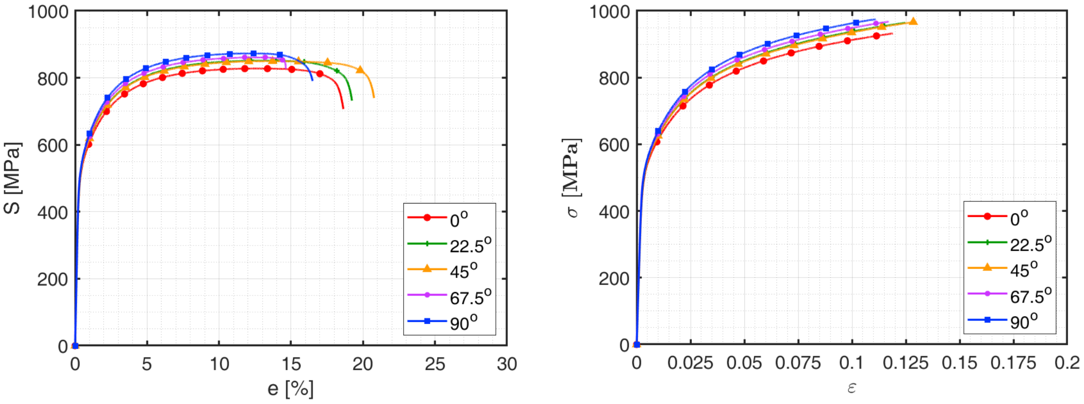

(c) DP780

Figure 3.3: Experimental engineering stress-strain curves (left) and true stress-strain curves (right) for different loading directions.

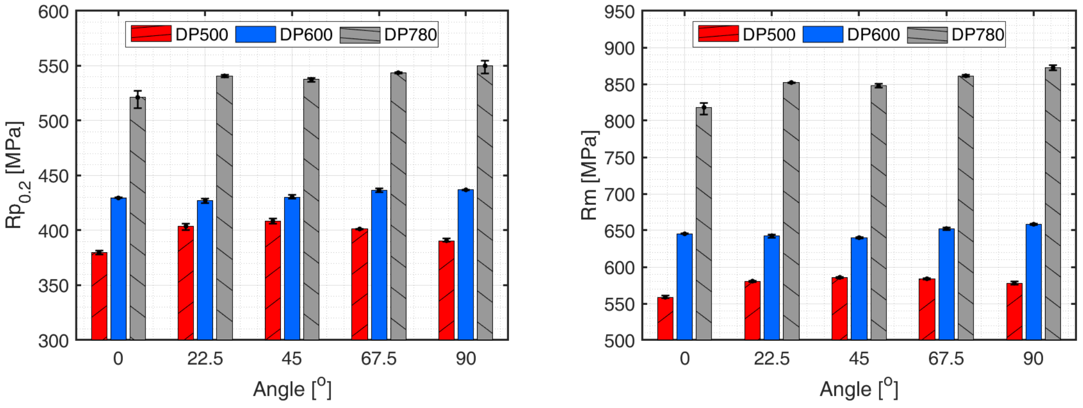

(a) Yield stress (0.2% offset)

(b) Ultimate tensile strength

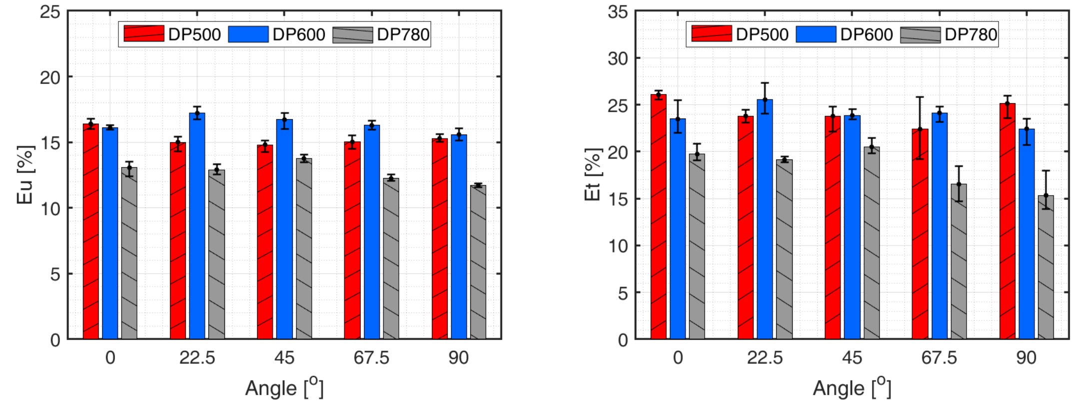

(c) Uniform elongation

(d) Total elongation

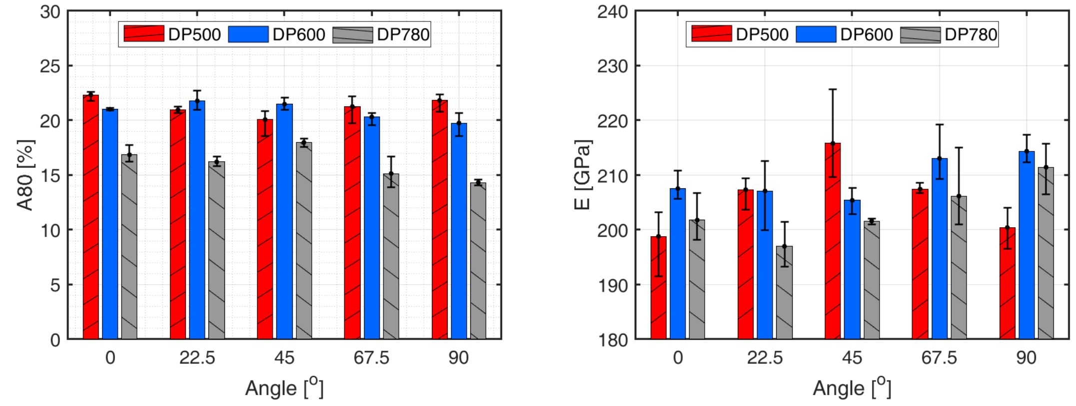

(e) A80

(f) Elasticity modulus

Figure 3.4: Average mechanical properties obtained from uniaxial tensile test and corresponding result dispersion for the three AHSS dual-phase steels.

Figure 3.3 shows that the obtained engineering stress-strain curves of the three AHSS grades evaluated become almost flat for maximum force, thus meaning a reduced strain hardening, after an initial stage of high hardening behavior, at initial yielding.

Another property that can be observed in figure 3.3 is the material strength, either its yield stress or ultimate tensile strength. As expected, DP780 exhibits a higher yield point than the DP500 and DP600 (figure 3.4(a)), but a lower ductility. This behavior can be explained by the higher percentage of hard martensite phase in the material microstructure.

On the other hand, when analyzing figures 3.3 and 3.4, DP600 steel, although having higher strength than DP500, has its deformation limits on similar level to DP500, not following an usual rule of 'increasing strength, decreasing ductility', which is followed by DP780 (e.g. figures 3.4(c) and 3.4(d)).

Although the selected dual-phase steels have different ultimate tensile strength values, the flow stress curves show a relatively high slope at lower strains, meaning that this AHSS exhibit a higher initial work hardening.

Table 3.4: Mechanical properties of dual-phase steels obtained from tensile tests for different angles relative to the rolling direction.

Material	Angle [^{o}]	$Rp_{0.2}$ [MPa]	Rm [MPa]	e_u [%]	$A80$ [%]
DP500	0	379.7	558.7	16.4	22.3
	22.5	403.8	580.6	15.0	21.0
	45	408.5	585.9	14.8	20.1
	67.5	401.3	583.9	15.0	21.3
	90	390.6	577.8	15.3	21.8
DP600	0	429.6	645.3	16.1	21.0
	22.5	427.3	642.7	17.2	21.8
	45	430.4	640.0	16.7	21.5
	67.5	436.6	652.5	16.3	20.3
	90	437.0	658.4	15.6	19.8
DP780	0	521.2	818.2	13.1	16.9
	22.5	540.8	852.1	12.9	16.2
	45	537.6	847.5	13.8	18.0
	67.5	543.7	861.3	12.2	15.1
	90	550.0	872.3	11.7	14.3

One difficulty faced during the uniaxial tensile tests was the necking occurrence and corresponding failure of the material outside of the gage measurement length. This effect occurred for DP600 specimens for 67.5° relative to the rolling direction. However, additionally samples have been tested, so that all the needed data could be collected.

3.2.1.2 Determination of anisotropic r-values

Usually, sheet metal materials may have mechanical properties dependent on loading direction, which suggests that some anisotropy exists. The strain plastic anisotropy of a sheet metal can be characterized, under plane stress conditions, through uniaxial tensile tests carried out on specimens taken from various angles relative to the rolling direction in the sheet plane. The parameter commonly used to characterize this behavior is the anisotropic r-value and it is defined as the ratio between the true plastic strain in the width (ε_{22}^{p}) to the strain in the thickness (ε_{33}^{p}), as shown in following expression:

$$r = \frac{\frac{w}{w_0}}{\frac{t}{t_0}} = \frac{\varepsilon_{22}^{p}}{\varepsilon_{33}^{p}} \tag{3.1}$$

where w_0, t_0 and w, t represent, respectively, the initial width and thickness, and the width and thickness at the defined instant.

The thickness true plastic strain is calculated from the principle of volume constancy, thus, the equation 3.1 can be simplified as:

$$r = \frac{\varepsilon_{22}^{p}}{\varepsilon_{33}^{p}} = -\frac{\varepsilon_{22}^{p}}{\varepsilon_{11}^{p} + \varepsilon_{22}^{p}} \tag{3.2}$$

where ε_{11}^{p} is the true plastic strains in the axial direction of the specimen.

The methodology mentioned in the standard [82] to continuously measure the strains is performed by using extensometers in both axial and transverse directions during the tensile test. Another alternative is using a manual procedure, where a grid pattern is created on specimen surface. The material is stretched up to a certain deformation level and manually one measures the corresponding strains. Often these measurements are taken at a particular value of strain, e.g. at $e = 15\%$. Despite being a widely used methodology, the accuracy of anisotropy measurement may be compromised by the lack of information in the plastic regime, since only one point is obtained.

To improve the accuracy and the amount of information on material anisotropic behavior, in this research, the evaluation of the true plastic strains and corresponding r-values is performed through the technique of digital image correlation (DIC), which allows the measurement of the deformation field evolution for a defined area on the specimen.

In order to perform the experimental tests, it is necessary to prepare the specimens for DIC analysis. In DIC, it is required to paint the specimen surface in white and then create a random black speckle pattern on (average speckle size of about 50 μm), as illustrated in figure 3.5. This pattern will allow the DIC cameras to detect the black dots and then capture their relative displacements.

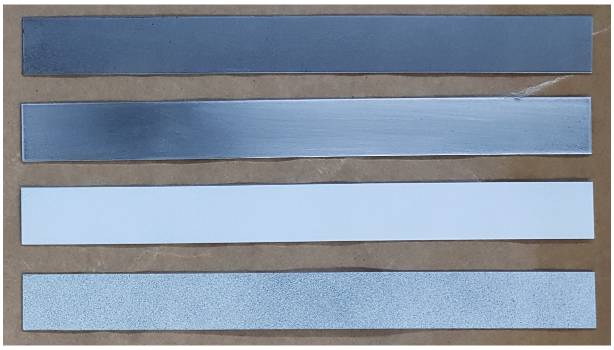

Figure 3.5: Specimen preparation for r-value measurement using DIC.

The experiments were performed on a 300 kN testing machine (Instron 5900R) at an initial strain rate of 1e^{-3} s^{-1}. To measure the strain field, images were taken at a frequency of 20 Hz with a 5MP camera (Basler acA2440-75um, 2448x2048 pixels) in conjunction with a high resolution lens (Fujinon HF50HB-1B, f2.3/50 mm). The commercial software VIC-2D.v6 was used to compute the strain field (logarithmic Hencky strains) considering a step size of 7 and a set size of 25 for a defined region of interest. In table 3.5 it is defined the list of main principal experimental conditions applied for determination of anisotropic r-values of current dual-phase steels.

Table 3.5: Experimental conditions used for r-value determination.

Loading directions	5
Number of experiments for each direction	3
Crosshead speed (grip)	5 mm/min
Data acquisition	20 Hz
Temperature	23 ^{o}C
Relative humidity	53%

Figure 3.6 presents the experimental relationship between thickness strain and transverse strain during the tensile test for each defined loading direction and material. Using

a linear regression to fit the experimental points, the corresponding anisotropic r-value is determined from the line slope. Additionally, table 3.6 shows the measured experimental r-values obtained from the linear fitting in figure 3.6, as well as, the corresponding normal anisotropy ($\overline{R}$) and planar anisotropy (ΔR).

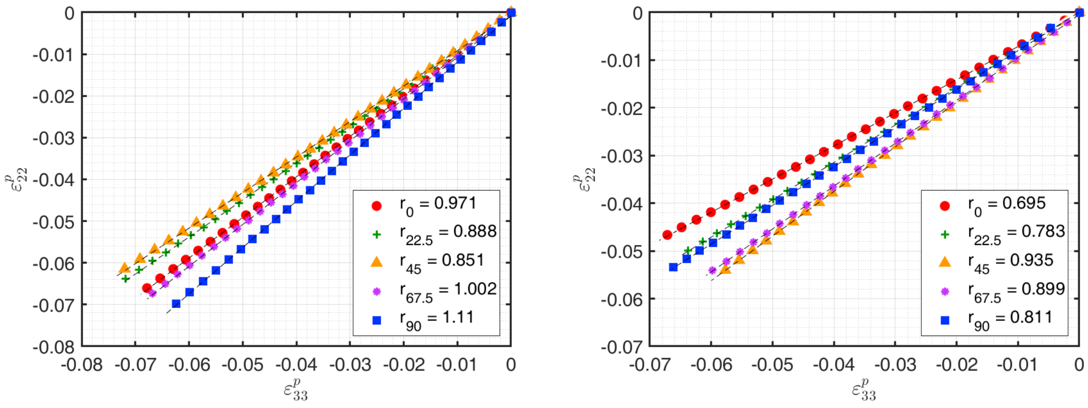

(a) DP500 (b) DP600

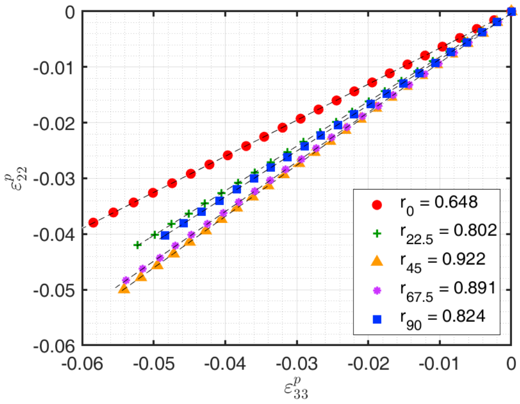

(c) DP780

Figure 3.6: Evolution of transverse and thickness plastic strain and corresponding anisotropic coefficient for five angles relative to the rolling direction.

Table 3.6: Measured experimental anisotropy coefficients of dual-phase steels using DIC techniques.

Material	r_0	$r_{22.5}$	r_{45}	$r_{67.5}$	r_{90}	$\overline{r}$	Δr
DP500	0.971	0.888	0.851	1.002	1.110	0.946	0.190
DP600	0.695	0.783	0.935	0.899	0.811	0.844	-0.182
DP780	0.648	0.802	0.922	0.891	0.824	0.829	-0.186

In order to evaluate and analyze the results obtained by DIC, a comparison was performed (figure 3.7) with the data obtained through the standard manual procedure defined in the corresponding standard. The plastic strain ratios were measured only for 0^o, 45^o and 90^o relative to the rolling direction. The attained axial strain level was 0.14, 0.12 and 0.09 for DP500, DP600 and DP780, respectively.

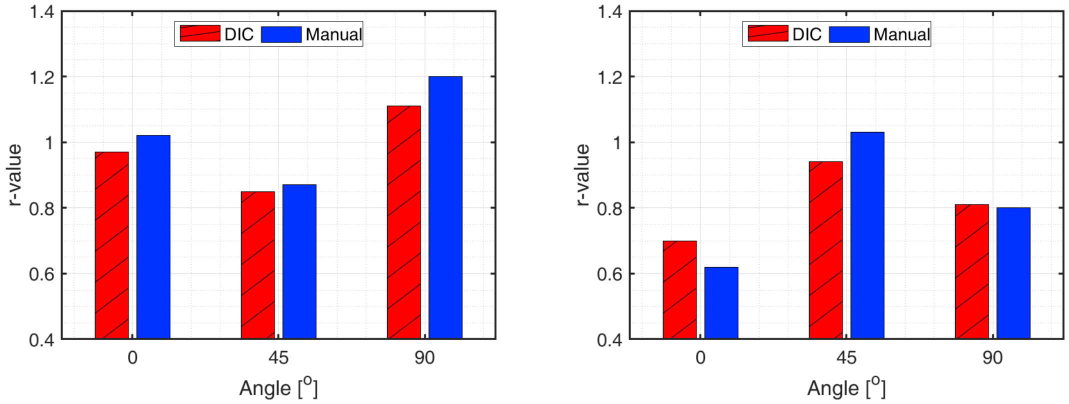

(a) DP500 (b) DP600

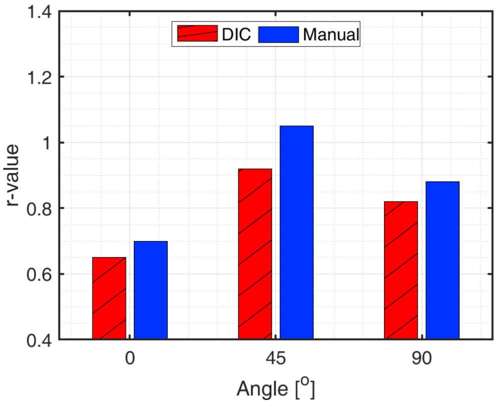

(c) DP780

Figure 3.7: Comparison of obtained r-value coefficients using DIC techniques and the standard manual procedure.

As seen in figure 3.7, there is a small difference between the obtained values using the classic method and DIC. In general, the r-values obtained by the classic approach are higher than those obtained from DIC. However, if the ratio between the true plastic strains along the width and thickness of the specimen remains constant during the axial deformation, as verified in figure 3.6, how can such difference be explained?

After an exhaustive analysis of the deformation field using the DIC images from the experimental test, it is possible to verify the existence of deformation bands in the measurement area, as shown in figure 3.8.

Since in the standard manual procedure, it is necessary to define a grid of points on the surface of the specimen, the distance between them can include different axial strains. If the distance between the points is higher than the band, an average plastic strain will be computed, which leads to an increase of the corresponding anisotropic coefficient, as the one observed in figure 3.7.

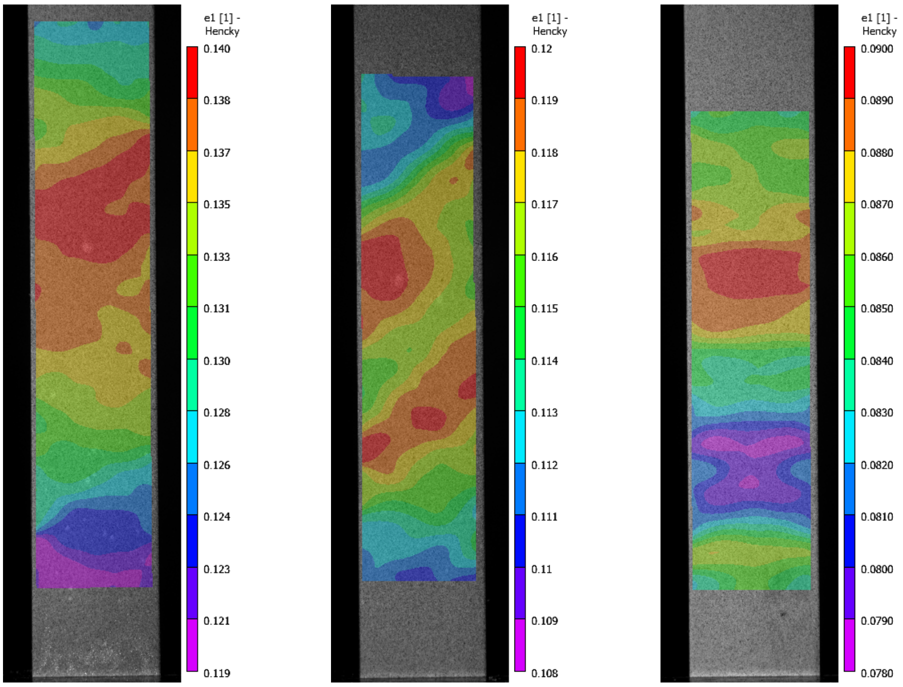

(a) r_0 for DP500 (b) r_{45} for DP600 (c) r_{90} for DP780

Figure 3.8: Axial true strain (ε_{11}) field obtained from DIC of dual-phase steels.

3.2.1.3 Temperature induced by plastic deformation

In the sheet metal forming process, the transformation speeds of the materials depend on the technological process and the equipment to be used. A uniaxial tensile test can be carried out at different strain rates to simulate the actual processing conditions of the materials. However, it must be taken into account that the plastic deformation generates heat and, consequently, an increase of specimen temperature [83, 84, 85].

A main objective of this section is to investigate and evaluate the temperature evolution associated with specimen plastic deformation for different strain rates using the three dual-phase steel grades. Uniaxial tensile tests for the selected materials were performed according to ASTM E8M [81] along the rolling direction. To measure the specimen temperature, non-contact infrared thermography (IFR) techniques were applied simultaneously with DIC. Such methodology allows the acquisition of the surface specimen temperature field evolution for an area of interest. The major challenge, when using these techniques together, is the correct location of the white light used to capture DIC images so that, it does not interfere with the use of infrared thermal camera optical field. Figure 3.9(a) shows the experimental apparatus needed to perform the tensile test under these conditions.

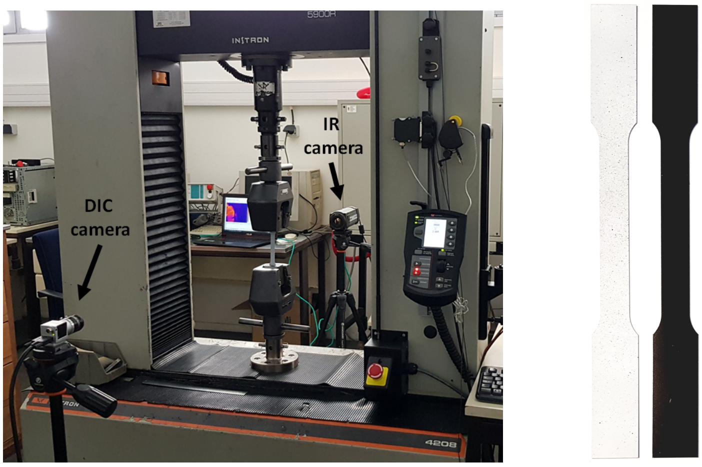

(a) Experimental apparatus (b) Specimen surface

Figure 3.9: Experimental setup used to measure the strain fields and temperature evolution.

Also, both surfaces of the specimen must be carefully prepared. To obtain and acquire accurate results from IFR, the corresponding surface must be coated with matt black, to ensure an emissivity nearly to 1, while for DIC, a black speckle pattern is painted on top of matt white, as presented in figure 3.9(b). A FLIR A325 thermographic camera was used to measure the temperature field having an accuracy of $\pm$ 2 ^{o}C and a response time lower than 12 ms, while for the DIC a 5 MPixel camera (Basler acA2440-75um, 2448x2048 pixels) in conjunction with a high resolution lens (Fujinon HF50HB-1B, f2.3/50 mm). The commercial ThermaCAM Researcher Pro software was used to acquire the images and compute the temperature field, whilst the VIC-2D was considered to obtain the strain field.

The specimens were tested at room temperature with three crosshead speeds (0.49, 5 and 79.5 mm/min), resulting in an initial strain rate on the order of $1.6e^{-4}$, $1.6e^{-3}$ and $1.6e^{-2}$ s^{-1} respectively, up to the fracture, on a Instron 5900R testing machine using a 100 kN load cell. A summary of the experimental conditions is given in table 3.7.

Table 3.7: Experimental conditions of uniaxial tensile tests.

Crosshead speed (grip)	0.49, 5 and 79.5 mm/min
Data acquisition	3.75, 7.5 and 60 Hz
Clip gage initial length (DIC) - l_0	50 mm
Temperature	23.6 ^{o}C
Relative humidity	54%

However, when the machine crosshead speed is constant, the deformation speed (strain rate) decreases as the specimen increases its length, but for small variations in the length, the change in the strain rate value is not significant and can be assumed to be constant. Figure 3.10 presents the temperature evolution measured in specimen surface with engineering strain considering different crosshead speeds for the dual-phase steels.

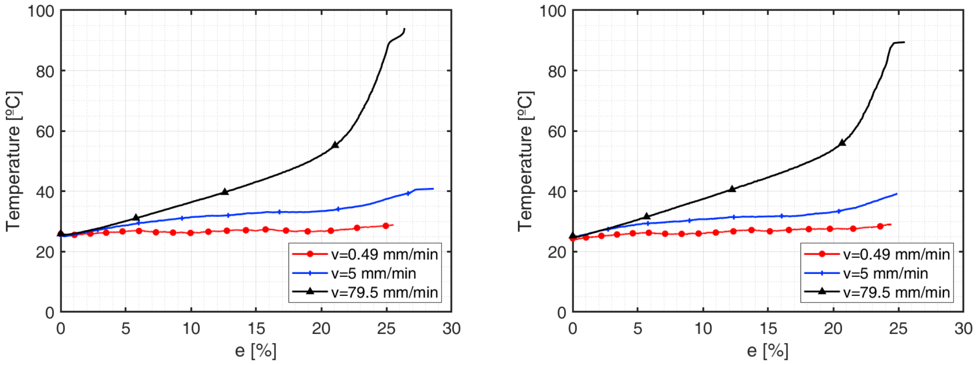

(a) DP500 (b) DP600

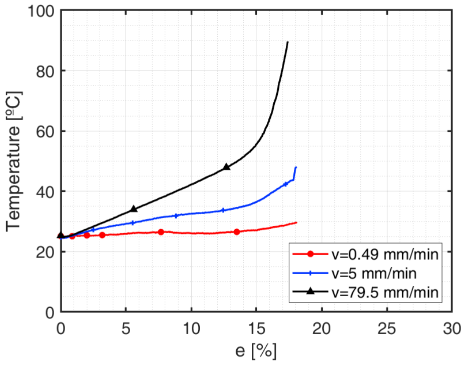

(c) DP780

Figure 3.10: Temperature evolution with engineering strain considering different crosshead speeds for the dual-phase steels.

Figure 3.10 shows the evolution of temperature, measured in the fracture zone of the specimen, as a function of the engineering strain. For the lowest crosshead speed (v = 0.49 mm/min) and therefore, a lower initial strain rate, the temperature distribution in the analyzed section remained almost constant for the three materials. This can be explained by the heat dissipation by convection to the air and by conduction through the grips. However, for the other two strain rates, there is a gradual increase in temperature that occurs in all tested materials. For these cases, the heat dissipation rate will be much lower than the heat generated by mechanical work.

With the increase of strain rate from $1.6e^{-4}$ to $1.6e^{-3}$, there is an average increase of 13.5 °C in the specimen, being more evident for the higher strain rate ($1.6e^{-2}$), where temperatures between 77°C and 94 °C are registered and an average increase in temperature of 44.1°C compared to the previous situation. In all cases, the maximum temperature occurs in the area where the fracture occurs, corresponding to what is expected, since it is the area where the highest deformations are measured.

This relationship between the temperature and plastic strain can be seen in figures 3.11, 3.12 and 3.13 for the different strain rates, respectively. The moment before the material fracture, the infrared thermographic images show an increase in the temperature in the center of the specimen towards the ends, similar to the behavior observed in the strain field obtained by the digital image correlation.

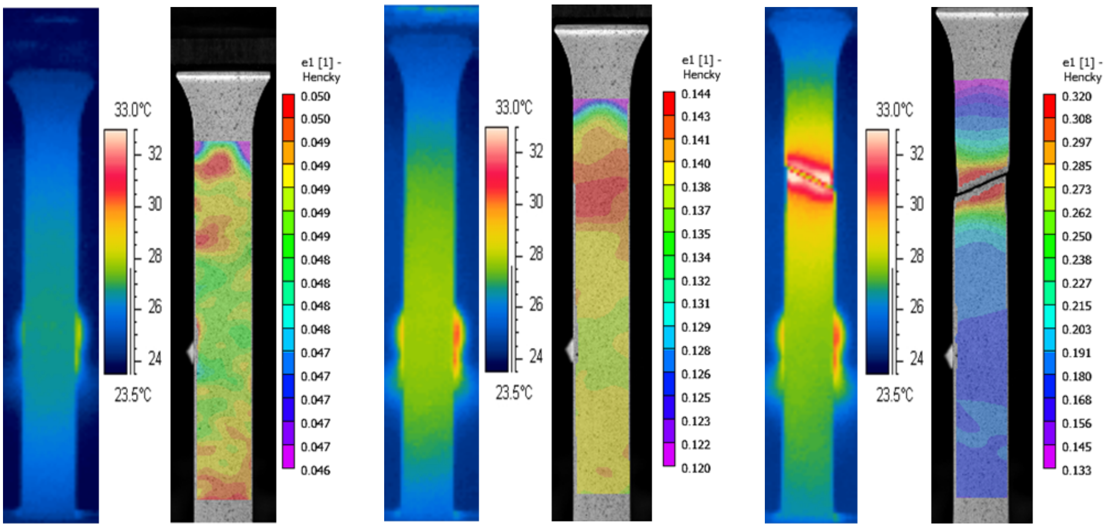

(a) e=5%　(b) e=15%　(c) Fracture

Figure 3.11: Evolution of temperature and true strain (ε_1) fields with deformation of DP600 for a crosshead speed of 0.49 mm/min.

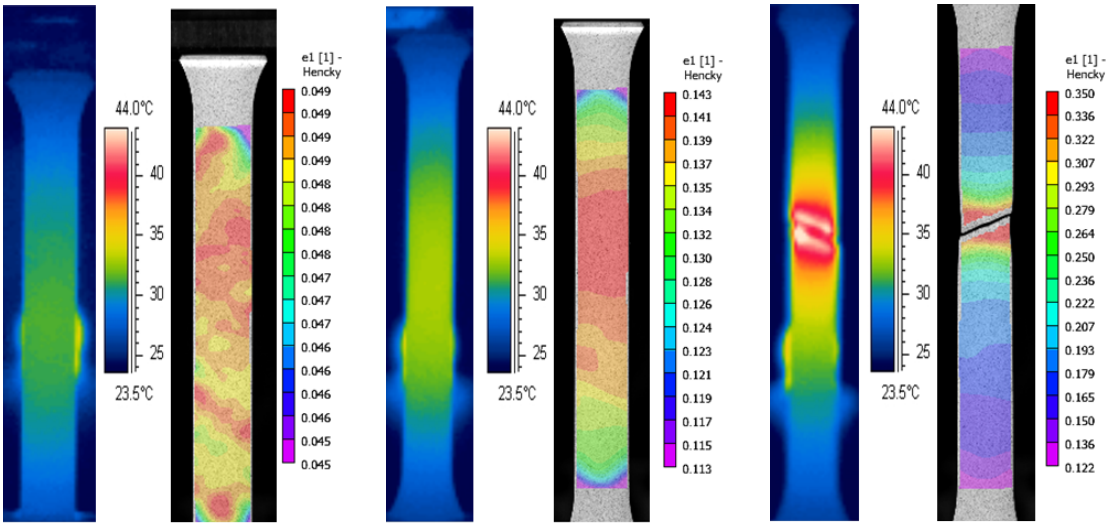

(a) e=5% (b) e=15% (c) Fracture

Figure 3.12: Evolution of temperature and true strain (ε_1) fields with deformation of DP600 for a crosshead speed of 5 mm/min.

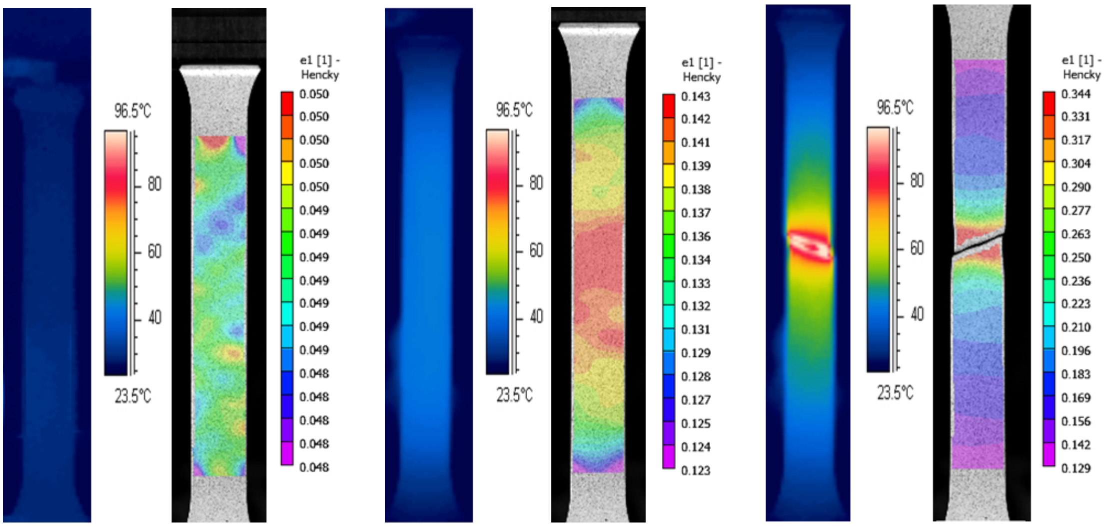

(a) e=5% (b) e=15% (c) Fracture

Figure 3.13: Evolution of temperature and true strain (ε_1) with deformation of DP600 for a crosshead speed of 79.5 mm/min.

Another analyzed result was the evolution of temperature as a function of the normalized engineering strain $\frac{e}{e_{max}}$, where e_{max} corresponds to maximum attained engineering strain value for each experiment. Since in the previously observed data, the maximum temperatures were similar for the same experimental conditions, regardless of the tested material. The obtained temperature evolution curves are shown in figure 3.14 for each considered strain rate.

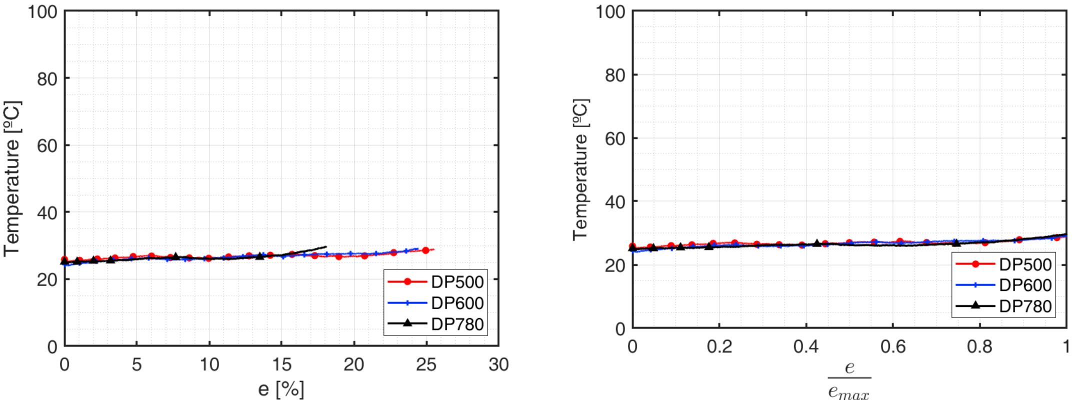

(a) v=0.49 mm/min (b) v=0.49 mm/min with normalized eng. strain

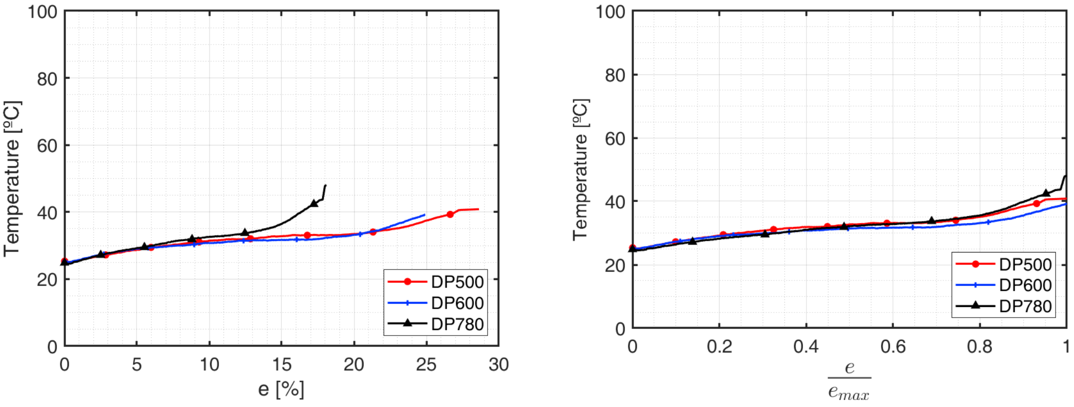

(c) v=5 mm/min (d) v=5 mm/min with normalized eng. strain

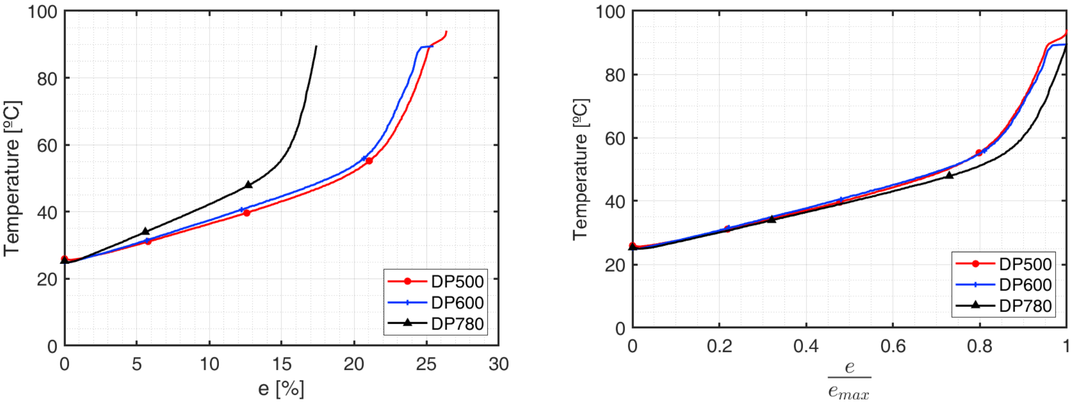

(e) v=79.5 mm/min (f) v=79.5 mm/min with normalized eng. strain

Figure 3.14: Comparison of temperature evolution with engineering strain of the dual-phase steels for the same crosshead speed.

As seen, the increase in temperature seems to be related only with specimen strain rate, independently the material strength or ductility when the normalized engineering strain is considered. For the same experimental conditions, the response and corresponding increase in temperature of the three dual-phase steels is almost identical for the entire range, even the maximum attained temperature values show a good agreement between the different materials. Also, for the analyzed strain rate values, the stress-strain curves for each material are very close, i.e., the dual-phase steels do not exhibit strain rate effect, as shown in figure 3.15.

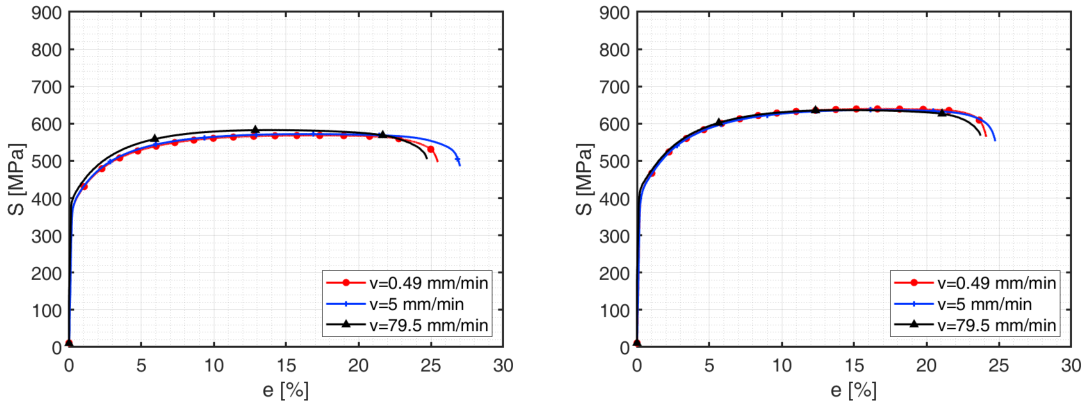

(a) DP500 (b) DP600

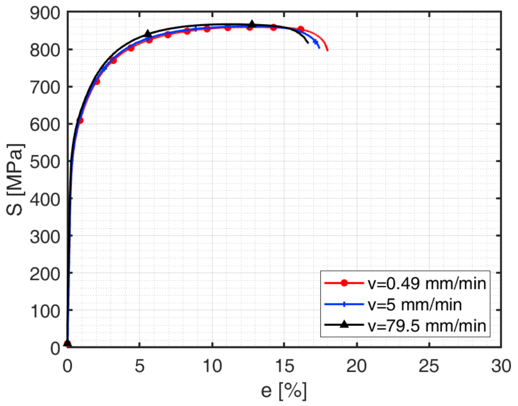

(c) DP780

Figure 3.15: Comparison of engineering stress-strain curves of the dual-phase steels for different crosshead speeds.

3.2.2 Hydraulic bulge test

Although the uniaxial tensile test is the most used in the mechanical characterization of sheet metal materials, it should be noted that the obtained deformation limits there are not those which the material can withstand if other loading conditions are applied. Due to the plastic instability that appears in the uniaxial tensile test, the stress-strain curve can only be defined for lower values of true strain, when compared to different loading conditions, such biaxial loading. Therefore, such experimental tensile test data will need to be extrapolated to characterize the material at higher values of strain, which can give different results, according to the extrapolation method.

An alternative solution is to perform biaxial hydraulic bulge tests since this type of loading allows obtaining more experimental information about the material behavior, with higher values of plastic deformation when compared to the tensile test, thus improving its mechanical hardening characterization.

The biaxial hydraulic bulge is a test whose design and configuration promotes the material to be in a biaxial stress state. This state is achieved by sealing and restricting a circular sheet along its perimeter and injecting oil under pressure into the central underside zone. With this mechanical characterization test, it is possible to obtain the biaxial stress-strain curve of the tested material. In case of the available equipment, which was used during this research, the specimen is deformed plastically using hydraulic pressure [86, 87], as shown in figure 3.16, yet other means can be used to obtain the same effect [88, 89].

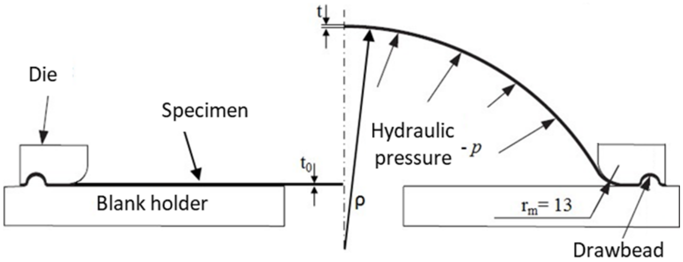

Figure 3.16: Representative scheme of the hydraulic bulge test and its key variables (dimensions in mm) - adapted from [87].

Additionally, an advantage of using the biaxial hydraulic test is the lack of contact (and therefore no friction) in the area of characterization interest, which makes the analytical solution less complicated.

The experimental set consists of a circular die and a circular blank holder, which restrict the specimen at its periphery during the test by means of a drawbead, which also prevents any leakage of oil. The dimensions of the tools used in the experimental test are presented in table 3.8 [90].

Table 3.8: Tools dimensions of the hydraulic bulge test.

Parameter	Value [mm]
Die diameter - ϕ_{die}	150
Die radius - r_m	13
Drawbead diameter - $\phi_{drawbead}$	190
Specimen diameter	250

The acquisition of the fundamental data for the characterization of the material is performed by a measurement system, which acquires the values and its evolution during the deformation process [91]. In order to obtain the biaxial stress-strain curve based on the experimental data, the membrane theory is used.

The biaxial bulge test is used to characterize materials with low thicknesses (typical values below 2 mm), being the case of metal sheets. This range of values, coupled with the size of the die diameter, shall correspond to ratios of bulge diameter to sheet thickness, which are advised to be higher than 100 [92] or higher than 50 [93]. In this way, the bending effects in the test can be neglected and therefore the stresses along the thickness (σ_3) are assumed to be zero.

Based on the previous concepts, a relationship between the variables of hydraulic pressure (p), sheet thickness at each instant (t), the radius of curvature (ρ) and biaxial stress (σ_b) is established. Since the stresses in the principal directions are assumed to be equal ($\sigma_1 = \sigma_2$), as well as, the radii of curvature ($\rho_1 = \rho_2$) when considering the case of axissymmetry, the expression that translates the previous relation is the following:

$$\sigma_b = \frac{p \cdot \rho}{2 \cdot t} \tag{3.3}$$

The determination of the radius of curvature (ρ) and the thickness of the specimen (t) at the pole can be obtained by a measurement system, shown in figure 3.17(a), or using the digital image correlation, as mentioned also in the ISO standard [94].

The calculation of the radius of curvature is given by a simple geometric construction, expressed as:

$$\rho = \frac{\left(\frac{Dcv}{2}\right)^2 + h^2}{2 \cdot h} - \frac{t}{2} \tag{3.4}$$

where h is the measured distance between the displacement transducer and the support of the spherometer, and Dcv the diameter established by the spherometer, as shown in the diagram of figure 3.17(b).

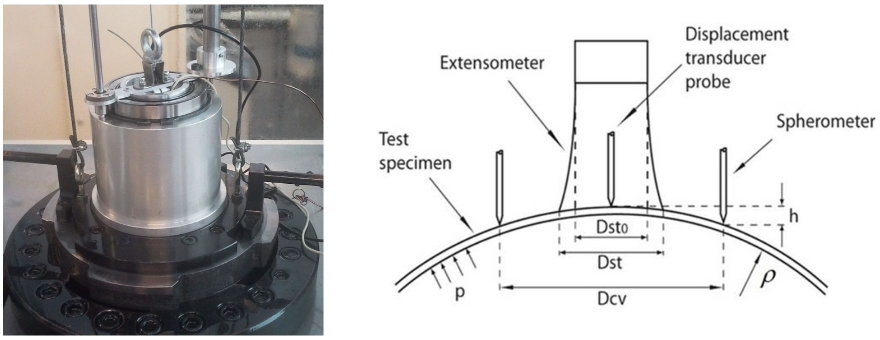

(a) Mechanical measurement system

(b) Scheme of the mechanical measurement system

Figure 3.17: Experimental device for measurement and acquisition of fundamental variables during the biaxial hydraulic bulge test.

The acquisition of these variables is carried out on the outer surface of the sheet metal, however, the membrane theory only applies to the neutral axis [92], thereby half of the thickness is removed at the calculated radius [95].

Finally, the thickness of the sheet metal is calculated using equation 3.5, measuring the initial thickness (t_0) and determining the value of the thickness strain (ε_t). The thickness of the material (t) will decrease, which is calculated by:

$$t = t_0 \cdot e^{-\varepsilon_t} \tag{3.5}$$

The reduction of the thickness in the specimen concentrates in the center and can be considered a geometric restriction since the fracture will occur in such area. Assuming that the material as incompressible, i.e., the sum of all strains is zero and therefore the volume of material remains constant during the experimental test, the thickness strain (ε_t), also known as biaxial strain (ε_b), can be determined based on the following expression, considering the strains in the sheet plane ($\varepsilon = \varepsilon_1 = \varepsilon_2$):

$$\varepsilon_b = \varepsilon_t = -2 \cdot \varepsilon \tag{3.6}$$

where ε is the membrane strain.

The value of membrane strain is obtained by measuring the expansion of a circle whose initial diameter is D_{st_0}. For the acquisition of such variable, a strain gage is used in the measurement system, which follows the plastic deformation of the sheet metal throughout the experimental test. As the diameter of the circle increases, taking a value of D_{st}, the membrane strain is given by:

$$\varepsilon = ln\left(\frac{D_{st}}{D_{st_0}}\right) \tag{3.7}$$

3.2.2.1 Equi-biaxial stress-strain curve

In order to obtain the biaxial stress-strain curve of the dual-phase steel sheet materials, the equations 3.3 and 3.6 are used. Experimental characterization tests were performed with a constant pressure increment and controlled ambient temperature. The test conditions are given in table 3.9.

Table 3.9: Experimental conditions used in hydraulic bulge test.

Parameter	Value
Specimen diameter	250 mm
Hydraulic pressure increment	1 bar/s
Room temperature	23 ^{o}C
Relative humidity	56 %

Figure 3.18 presents the obtained biaxial stress-strain curves for the materials used in this research, as well as, the evolution of hydraulic bulge pressure with specimen pole total height.

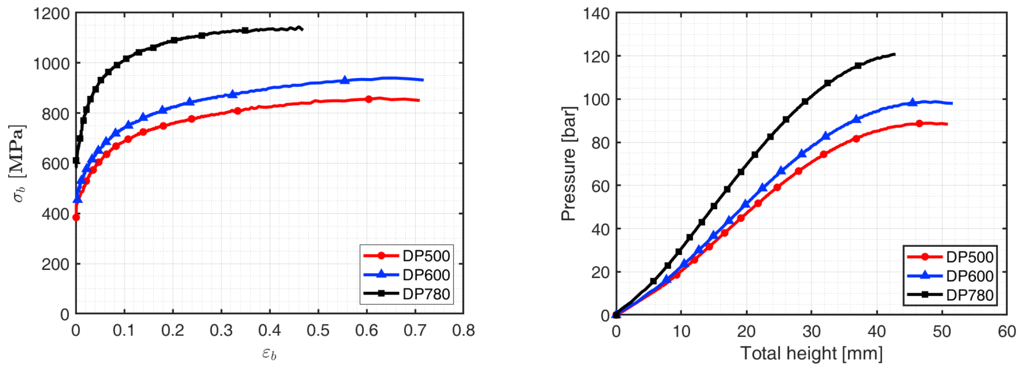

(a) Equi-biaxial stress-strain curves

(b) Evolution of pressure with pole height

Figure 3.18: Obtained biaxial stress-strain and pressure vs. height curves for the studied dual-phase steels (DP500, DP600 and DP780).

As already seen in the tensile test, DP780 steel is the material with the highest strength, being the DP500 the material with the lowest one. However, the plastic deformation ability is higher in the DP500 than in the DP780, as expected. A balance between strength and formability is seen by DP600 steel, since its characteristics lie between the other two materials, although its behavior on ductility is very similar to DP500. These results are related to the microstructure of the material since the DP500 is the material that presents a lower percentage of martensite and consequently lower mechanical strength.

Table 3.10 presents some variables acquired during the experimental tests for each analyzed material.

Table 3.10: Obtained properties from hydraulic bulge test for the different dual-phase steels.

Material	Burst pressure [bar]	Total height [mm]	Biaxial stress [MPa]
DP500	88.4	52.7	414.8
DP600	98.0	51.7	442.6
DP780	120.8	42.9	585.1

3.2.2.2 Transformation of stress-strain biaxial bulge curve and combination with tensile data

One advantage of using the biaxial hydraulic bulge test is the ability to obtain information and data of the material behavior for higher levels of plastic deformation when compared to those obtained with the tensile test. This advantage makes it possible to extend the hardening curve of the material using the biaxial curve. However, due to the different stress states present in each test, the stress-strain curves cannot be directly compared and/or combined.

After performing these two experimental tests, there are two hardening curves for the same material ($\sigma = f(\varepsilon)$ corresponds to uniaxial tensile test along the sheet rolling direction and $\sigma_b = f(\varepsilon_b)$ corresponds to the biaxial hydraulic bulge test curve). Therefore, it is necessary a transformation of the biaxial curve into an equivalent one, based on the equivalent plastic work per unit volume (W). This methodology has been used by several researchers with satisfactory results [88, 96, 97].

Although, this process could be carried out in inverse order, the standard (and commonly used) hardening curve of the material is the stress-strain curve from the uniaxial tensile test along the rolling direction.

Defining Wu and Wb as the equivalent plastic work of uniaxial tensile test and bulge test, respectively, it is possible to establish a link between the two curves when both equivalent plastic works take the same value ($Wu = Wb$), i.e.:

$$\begin{cases} \sigma \rightarrow W_u = W_b \rightarrow \sigma_b \\ \\ \varepsilon \rightarrow W_u = W_b \rightarrow \varepsilon_b \end{cases} \tag{3.8}$$

Assuming the incompressibility of the material and considering that the stress state at the pole is such that $\sigma_1 = \sigma_2 = \sigma_b$, the stress-strain data from both tests are related by the following expression:

$$\frac{\sigma}{\sigma_b} = \frac{\varepsilon_b}{\varepsilon} = k \tag{3.9}$$

where k is a constant.

The relationship between the equivalent plastic work and stress-strain data and the methodology for its calculation can be obtained from the integration of $\sigma = f(\varepsilon)$ for the entire plastic domain, being translated by equation 3.10.

$$W(\varepsilon) = \int_{\varepsilon_i}^{\varepsilon_f} \sigma(\varepsilon) \cdot d\varepsilon \tag{3.10}$$

Since there is no $\sigma = f(\varepsilon)$ function that fully translates the relationship between these the two variables, a trapezoidal rule is used to simplify the integral present in the equation 3.10, where:

$$W(\varepsilon) \approx \sum_{i=1}^{i=n-1} (\varepsilon_{i+1} - \varepsilon_i) \cdot \frac{\sigma_{i+1} + \sigma_i}{2} \tag{3.11}$$

Taking into consideration the principle of equivalent plastic work, several methods can be used to determine the "optimum" value of k parameter, as shown in figure 3.19. However, based on studies in the literature [88, 96, 97], the method that provides the best results is for the equivalent plastic work that corresponds to the maximum attained value of stress and strain in the tensile test ($\sigma_{max} \rightarrow W_{u_{max}} = W_b \rightarrow \sigma_b \Rightarrow k = \frac{\sigma_{max}}{\sigma_b}$), as shown in figure 3.19(a).

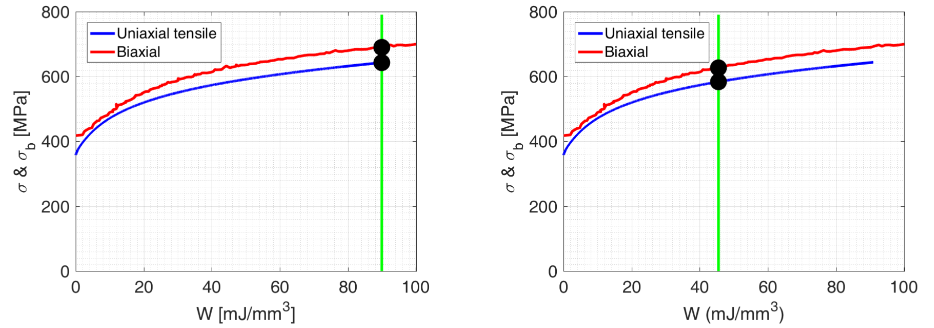

(a) Maximum equivalent plastic from tensile test

(b) Half of equivalent plastic from tensile test

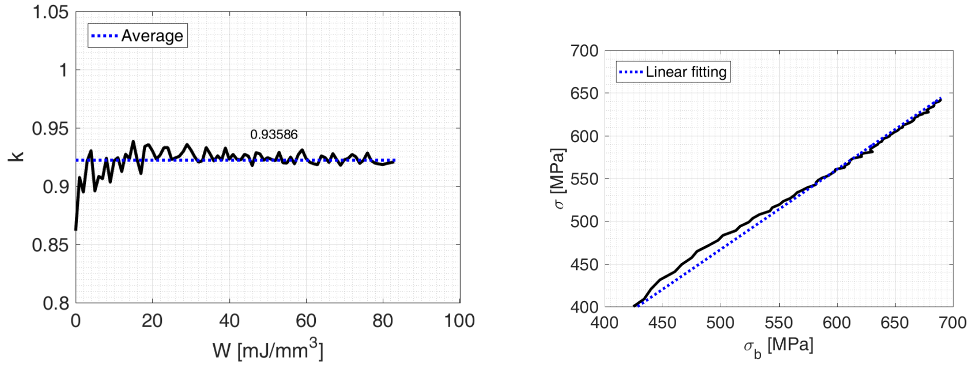

(c) Average k parameter

(d) Stress relation

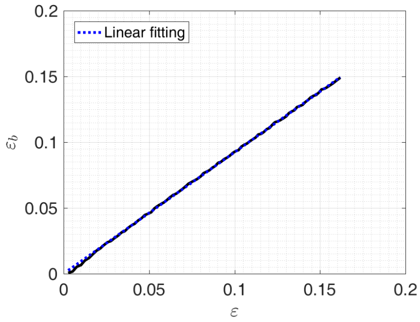

(e) Strain relation

Figure 3.19: Relation between equivalent plastic work and stress/strain obtained from each test (uniaxial tensile, bulge) by using the methodologies.

Such transformation enables the combination of the hardening curves by including the converted bulge data in the equivalent stress-strain curve. This allows a better identification of the constitutive law parameters that reproduce the mechanical hardening behavior, which is used as an input in numerical simulation. The hardening stress-strain curves using the converted biaxial are shown in figure 3.20, for each dual-phase steel under this study, considering the identified parameter k present in table 3.11.

Table 3.11: Obtained properties from hydraulic bulge test for the different dual-phase steels.

Material	DP500	DP600	DP780
k	0.898	0.955	0.874

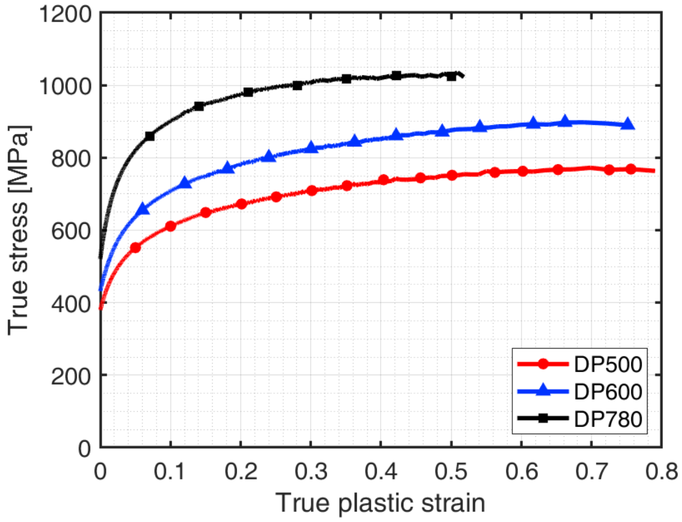

Figure 3.20: Equivalent stress-strain curves using the converted biaxial bulge data and combined with tensile test results.

It can be observed that implementing such methodology, there is good continuity for the extension of the hardening curve based on the bulge test, for the dual-phase steels.

3.2.3 Compression test

The compression test consists of the uniaxial application of a compressive load on a specimen. One result obtained from this test is the relationship between the linear deformation, obtained by measuring the distance between the platens or grips that compress the specimen, as a function of the load applied at each instant. The uniaxial compression test is standardized in the scientific community, according to the standard ASTM E9-19 [98] and it can be applied to cylindrical or sheet specimens.

Besides the yield stress that can be obtained from the stress-strain curve, the compression test also allows the determination of material anisotropy using round discs. These properties are essential, especially if the material presents some stress differential (SD) effect, i.e., tension-compression asymmetry.

In the following sections, uniaxial in-plane compression tests were performed to evaluate the yield stresses of the dual-phase steels for the rolling and transverse directions. Additionally, stacked disc compression tests were conducted to obtain the biaxial anisotropy of the materials. The acquired information is used in the calibration process of parameters for constitutive models and to improve the description of the material behavior.

3.2.3.1 Uniaxial in-plane stress-strain curve

Performing uniaxial in-plane compression tests on sheet metal specimen is a real challenge. When a sheet is subjected to compressive loads, the buckling tends to be more significant due to its slenderness. This phenomenon is intensified, especially when the ratio between the reference length and thickness of the specimen is high.

In recent years, several researchers have proposed several solutions to overcome the buckling effects in compression tests. The objectives are to maximize the compression strains and to allow a uniform distribution of stresses and strains throughout the area of analysis.

The most common method is to use an anti-buckling device that applies a lateral compressive load to stabilize the specimen during plastic deformation [99, 100, 101, 102]. The lateral stability is achieved with the use of supports between the specimen, but the measurement of the strain field is more complicated, without forgetting the friction between the contact surfaces, which may influence the obtained results, no matter how much effort is made to minimize its effect. On the other hand, some authors modify the geometry of the specimen [103, 104, 105], through miniaturization techniques, decreasing the ratio between the reference length and the sheet initial thickness. As expected, the lower the ratio between length and thickness, the higher is the level of compression strains measured without instability. The use of miniaturized test specimens for mechanical characterization has intrinsic difficulties, mainly in the accurate measurement of load forces and strain fields.

In this work, compression tests of miniaturized specimens were performed using an equipment (figure 3.21(a)) developed specifically for this type of request [105]. Two different loading conditions were defined, rolling and transverse direction (0^o and 90^o). The geometry of the specimens, shown in figure 3.21(b), was obtained by machining a rectangular strip. The experimental conditions of the test are given in table 3.12.

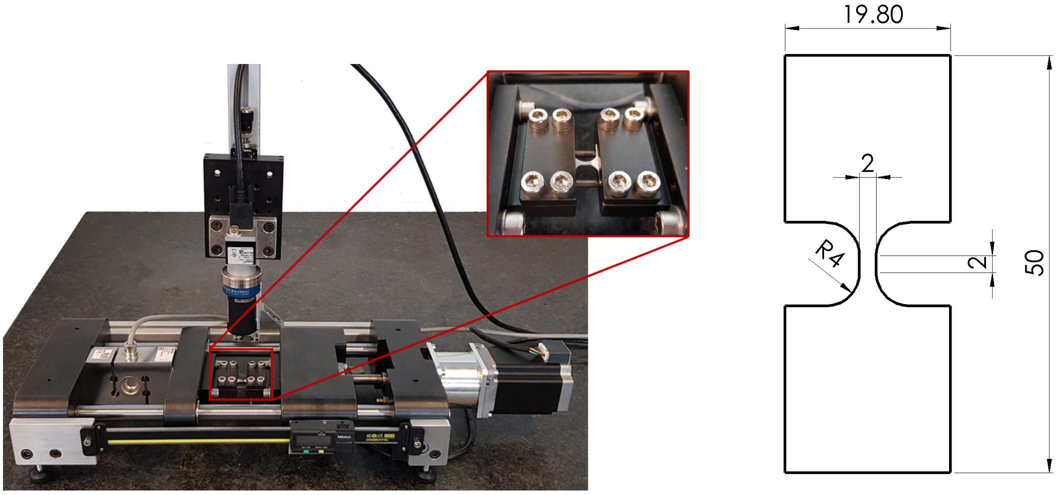

(a) MSTD equipment and DIC apparatus (b) Specimen geometry

Figure 3.21: Experimental setup used to perform MSTD (Mini Sample Tester Device) and corresponding geometry.

Table 3.12: Experimental conditions of uniaxial tensile tests.

Loading directions	2
Crosshead speed (grip)	0.5 mm/min
Data acquisition	10 Hz
Clip gage initial length - l_0	1.5 mm
Temperature	23 ^{o}C
Relative humidity	52%

The specimens were tested at room temperature with a constant crosshead speed on a 5 kN testing machine (MSTD - Mini Sample Tester Device). For the acquisition of elongation in the uniform section of the specimen, and therefore measuring of corresponding strains, the digital image correlation was considered. Due to the size of the in-plane uniform area, the average speckle size is lower than 15 μm. The DIC images were taken with a 5 MPixel camera (Basler acA2440-75um, 2448x2048 pixels) in conjunction with a telecentric lens (Infaimon OPE-TC-23-09, 45 mm). The commercial software VIC-2D.v6 was used to compute the strain field (logarithmic Hencky strains) considering a step size of 7 and a set size of 25 for a defined region of interest. The stress-strain flow curves obtained from the performed uniaxial compression tests are presented in figures 3.22, 3.23 and 3.24.

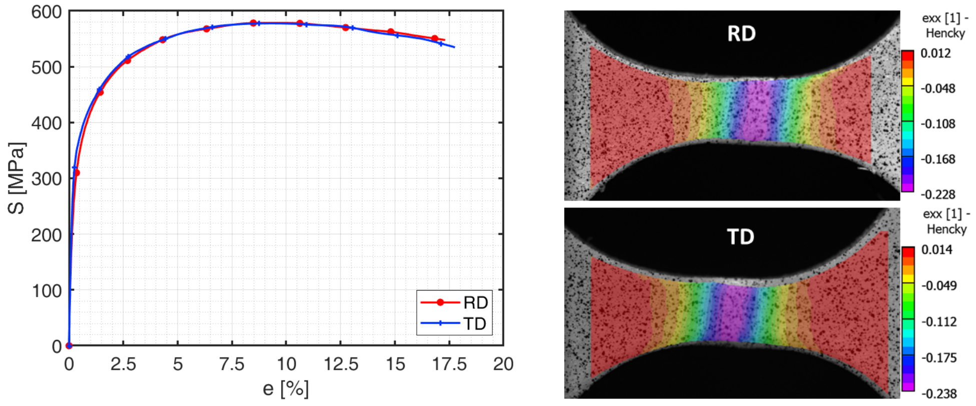

(a) Eng. stress-strain curve

(b) Strain field

Figure 3.22: Stress-strain curves and true strain (ε_1) field obtained from DP500 uniaxial compression tests.

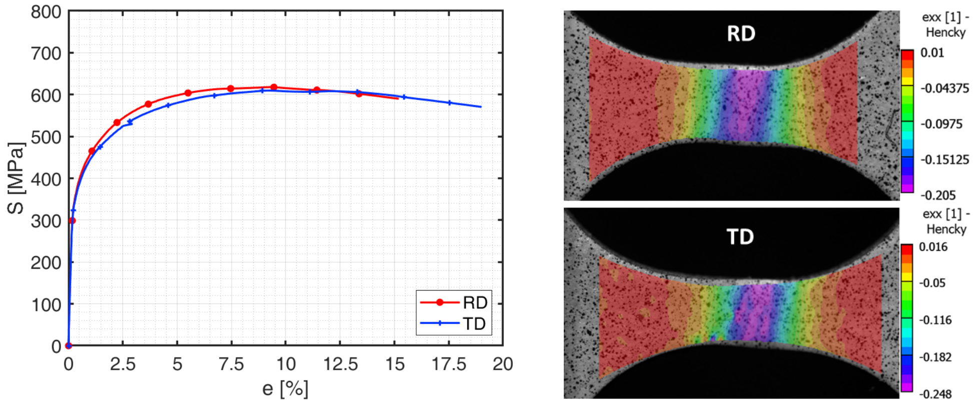

(a) Eng. stress-strain curve

(b) Strain field

Figure 3.23: Stress-strain curves and true strain (ε_1) field obtained from DP600 uniaxial compression tests.

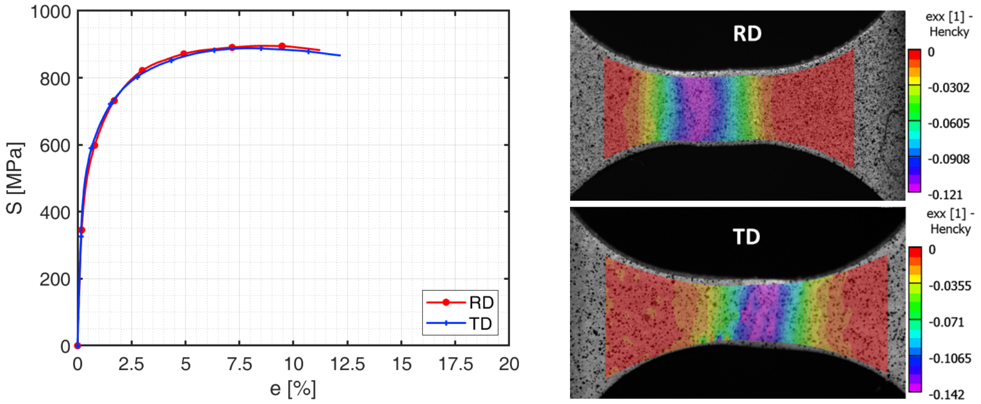

(a) Eng. stress-strain curve (b) Strain field

Figure 3.24: Stress-strain curves and true strain (ε_1) field obtained from DP780 uniaxial compression tests.

The figure figures 3.22, 3.23 and 3.24 show that these results with mini-samples have a hardening evolution very similar to the results obtained by the uniaxial tensile test with the standard sample dimensions. It is also observed that in compression the reached strain values were lower than in tensile, mainly due to the buckling phenomenon. Since the cross-section area is theoretical identical between the dual-phase steels, the behaviors are not very different. However, locally, the measured true strains have higher values, as seen in figures 3.22(b), 3.23(b) and 3.24(b).

Moreover, with these results, it is possible to identify the yield stresses of the material for a compressive stress state, allowing a better identification of the constitutive model parameters and improving the material behavior description. The yield stresses obtained from the compression tests for the rolling and transverse directions of each dual-phase steel are given in table 3.13.

Table 3.13: Yield stresses [MPa] obtained from uniaxial compression tests.

Loading directions	Material		
	DP500	DP600	DP780
RD	346.7	381.0	509.1
TD	358.7	386.2	534.0

3.2.3.2 Stacked disc - r$_b$ value

The stacked disc compression test, which corresponds to a through-thickness loading, is equivalent to an equibiaxial stress state, concerning the work hardening. A material property that can be measured is the biaxial plastic anisotropy [40]. This coefficient is also known as r_b and is defined as:

$$r_b = \frac{\varepsilon_{22}^{p}}{\varepsilon_{11}^{p}} \tag{3.12}$$

In this work, stacked disk compression tests were performed in order to obtain the biaxial anisotropy coefficient of the studied dual-phase steels, which is a requirement for some anisotropic yield models.

For the identification of such property, discs with an initial diameter of 10 mm were stacked and loaded in compression using two polished parallel platens. The discs were obtained from a punching machine in order to guarantee that all stacked discs had the same cross-section area and concentric.

Other important care in this type of test is the assembly process. During the assembly, all the contact interfaces, either between discs surfaces or between the contact points of upper and lower tools with the specimen, were well-lubricated with graphite grease. Additionally, a teflon foil with 0.15 mm was considered in the contact interface between platens and the specimen. Concentricity and axial alignment were also ensured in order to avoid any deviation from axial compression loading and to deform homogeneous the specimens under frictionless conditions.

Figure 3.25 shows an assembled stacked specimen that was obtained by pilling up five discs. The choice of 5 discs is related to the structural integrity of the specimen, because the use of stacks with a higher number of discs generates instability problems, by triggering the sliding between them.

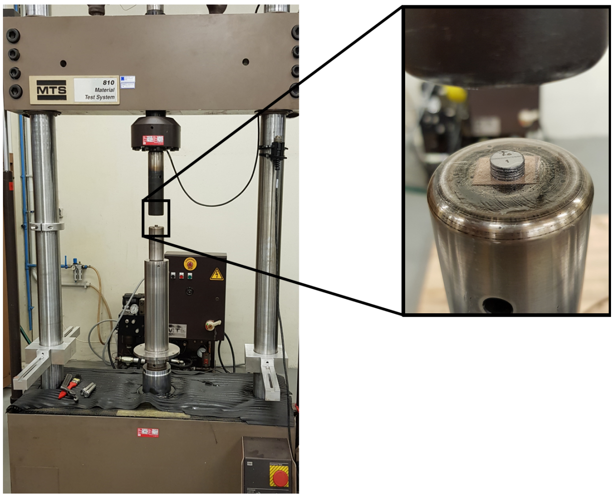

Figure 3.25: Experimental apparatus and dual-phase steel specimen between the compression platens.

To obtain the respective in-plane strain components (ε_{11}^{p} and ε_{22}^{p}), the diameters of each disc were measured before and after deformation. Also, the through-thickness strain (ε_{33}^{p}) was measured by considering the initial and final thickness. All of the true plastic strain components were calculated as:

$$\begin{cases} \varepsilon_{11}^{p} = & ln\frac{d_{RD}}{d_{RD_0}} \\ \varepsilon_{22}^{p} = & ln\frac{d_{TD}}{d_{TD_0}} \\ \varepsilon_{33}^{p} = & ln\frac{t}{t_0} \end{cases} \tag{3.13}$$

where d_{RD} and d_{TD} are the diameters associated with rolling and transverse direction of the sheet, respectively.

For a better description of the material behavior regarding the biaxial r_b coefficient, the specimens were subjected to different levels of plastic strain. However, the acquisition or direct measurement of strains is hugely complicated, and to obtain different amounts of plastic deformation, different maximum load values were established since the experimental test is performed in a load control mode. To impose the biaxial compression loading a hydraulic MTS 810 test machine with a 100 kN load cell was used.

The force range was defined between 70 kN and 90 kN, in order to guarantee a displacement that enables reaching the plastic regime. As the maximum imposed load is limited by the load cell (100 kN), the failure of the specimen when the maximum load capacity is reached was not attained. The test conditions are given in table 3.14 and figure 3.27 presents the strains measured in the specimen located in the middle (figure 3.26) for the three applied load levels to the dual-phase steels.

Table 3.14: Experimental conditions used in stacked disc compression test.

Parameter	Value
Initial disc diameter	10 mm
Number of stacked discs	5
Cross-head speed	1 mm/min
Applied force	70 kN (only for DP500) 80 kN (only for DP600 and DP780) 85 kN 90 kN

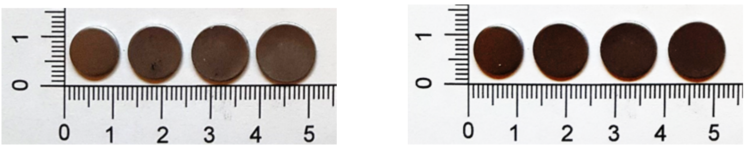

(a) DP500 (b) DP600

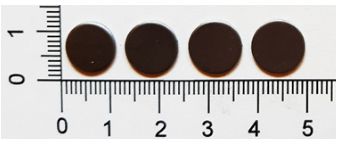

(c) DP780

Figure 3.26: Comparison between initial disc (before deformation) and the middle disc after deformation for the different applied conditions (force increase from left to the right for each material).

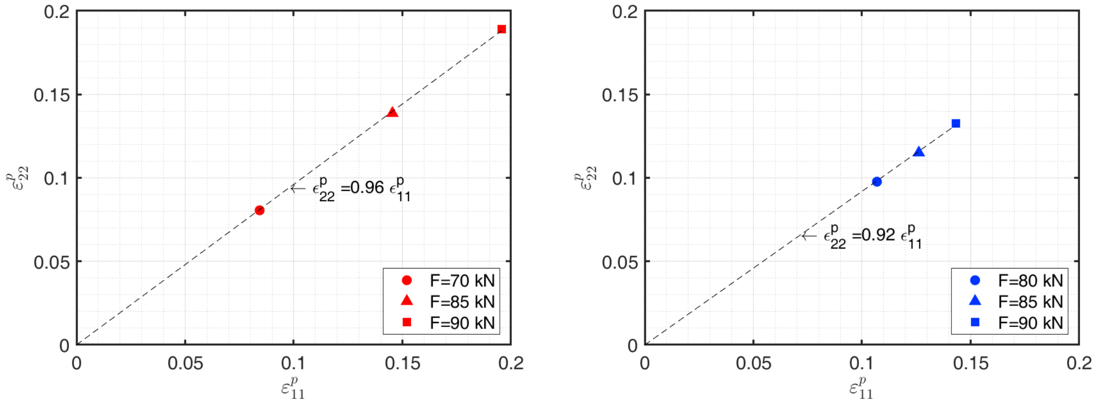

(a) DP500 (b) DP600

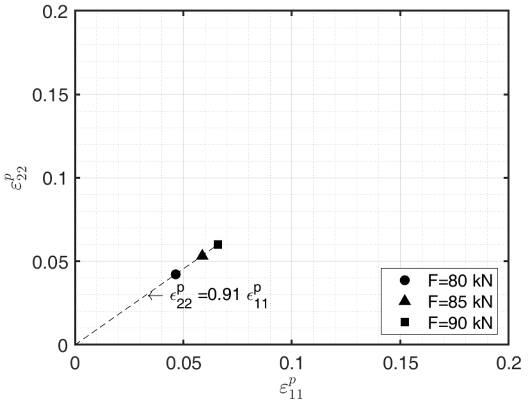

(c) DP780

Figure 3.27: Longitudinal and transverse strain relation of five circular stacked discs obtained from axial compression test of dual-phase steels.

As seen in figure 3.27, the transverse strains (ε_{22}^{p}) were plotted as a function of the longitudinal strains (ε_{11}^{p}) and a linear fit for all load cases was performed to model the experimental points. The value of r_b was defined as the slope of the linear fit. The experimental value of such parameter was found to be 0.96, 0.92 and 0.91 for DP500, DP600 and DP780, respectively.

Despite the obtained values not being far from the unit (isotropy), all the dual-phase steel exhibit biaxial anisotropy, more evident in the case of DP600 and DP780 than in case of DP500. In general, the studied materials are likely to deform more along to the rolling direction, taking the shape of an ellipse, as seen in figure 3.26. In the opposite direction, the dual-phase steels present some resistance to plastically deform in the transverse direction when subjected to a biaxial compression stress state.

Experimental values of force and displacement were also measured to plot the corresponding evolution, as shown in figure 3.28.

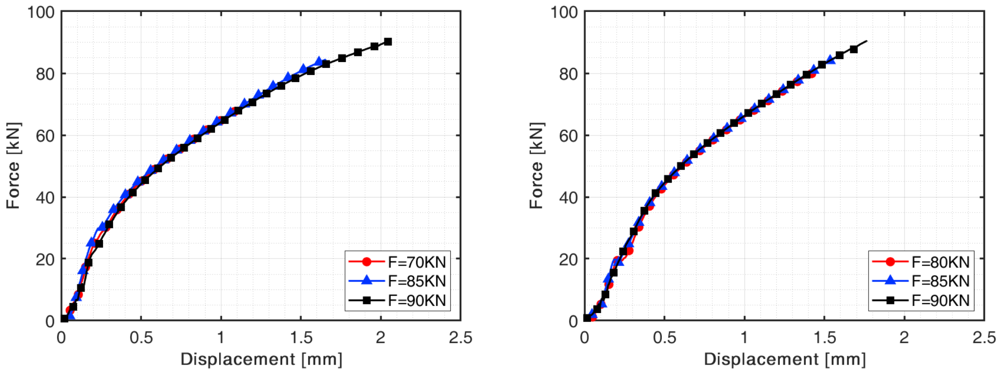

(a) DP500 (b) DP600

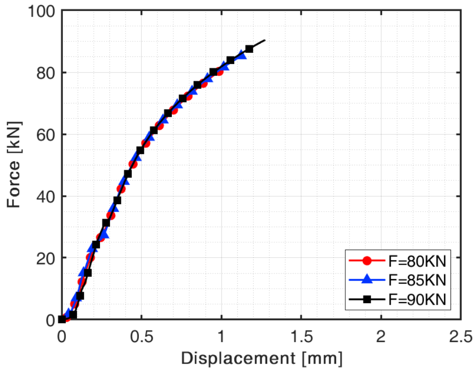

(c) DP780

Figure 3.28: Force vs. displacement curves of five circular stacked discs obtained from dual-phase steels axial compression test.

In the work of Barlat *et. al* [40], disc compression tests were performed using only one disc. In such research, it is stated that the measurements were accurate and reliable, and friction was expected to be low and roughly isotropic. Since the previously presented methodology to obtain the r_b parameter requires the correct stacking of the discs along to the rolling direction, using only one disc simplifies the experimental procedure. Therefore, experimental tests were carried out using one disc for two contact conditions with the tools: without any lubrication (dry) and with graphite grease. The obtained results were compared for the same conditions using a stacked specimen, as shown in figure 3.29.

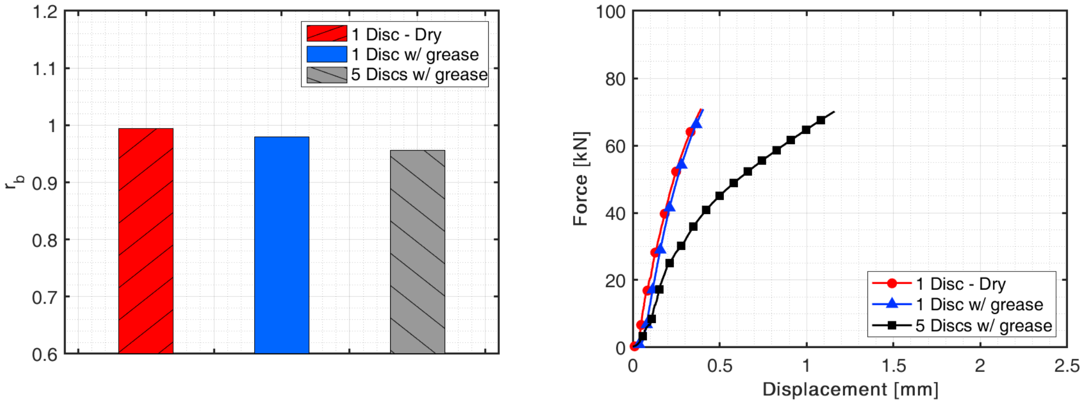

(a) Biaxial r_b anisotropy

(b) Force vs. displacement curves

Figure 3.29: Comparison of r_b value and force vs. displacement curves between one disc and five stacked discs using different lubricant conditions for dual-phase steel DP500.

As seen, the calculated ratio when using only one specimen is almost 1, for both contact conditions. The friction does not allow the material to flow, which could lead to an inaccurate result. That is a main reason why at least five stacked discs should be considered to perform the experimental test, in order to minimize such phenomenon.

3.3 Formability analysis

Sheet metal formability can be defined as the ability of metal to deform without necking or fracture into a desired shape. Every sheet metal can be deformed without failing only up to a certain limit, which is normally known as forming limit curve (FLC). Usually is experimentally determined for defined linear strain paths, by using Marciniak test, where a sheet metal sample is strained by a flat-bottomed cylindrical punch having a frictionless in-plane deformation, or by using Nakajima test, in which the sample is deformed by an hemispherical punch (out-of-plane) and by varying the sample width, different linear strain paths can be obtained.

3.3.1 Nakajima test

Nakajima et al. [106] proposed to use metal sheet strips with different widths, stretched by a hemispherical punch (figure 3.30(a)), to obtain the material forming limit curve. By varying the sample width, different strain paths can be achieved and different limit points can be calculated (figure 3.30(b)).

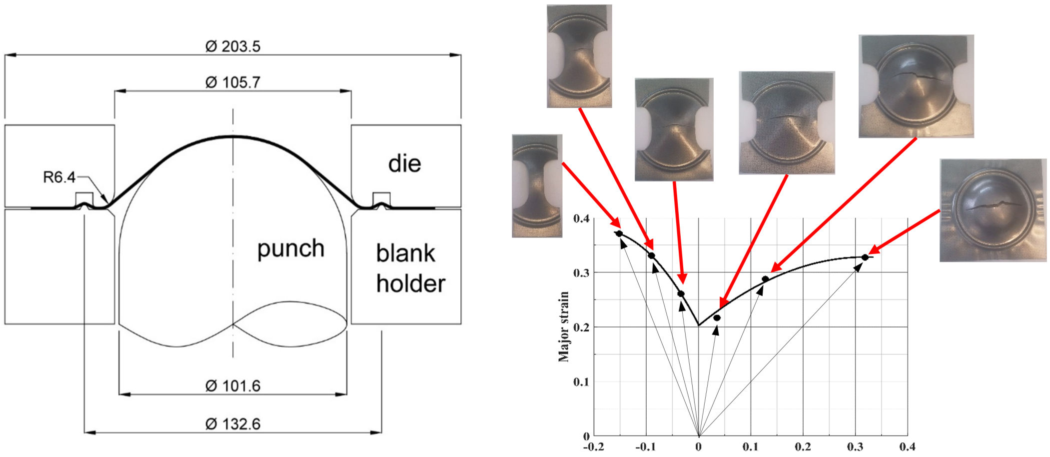

(a) (b)

Figure 3.30: (a) Tool dimensions and FLD setup used in Nakajima tests; (b) Obtained FLC points for different specimen widths.

The Nakajima testing apparatus uses a hemispheric punch of 101.6 mm diameter, a die and a blank holder (figure 3.31). The blank holder includes a drawbead to restrain the blank and also to avoid the stress concentration in the transition from the strip section to the measurement area.

Nakajima test experiments were performed according to the standard ISO 12004-2 [107], to measure the formability of current dual phase steels, as well as obtaining corresponding forming limit curves. Furthermore, this test allows the simulation of conditions very similar to those of the stamping processes, since it takes into accounts the friction between the punch and the sheet metal [108].

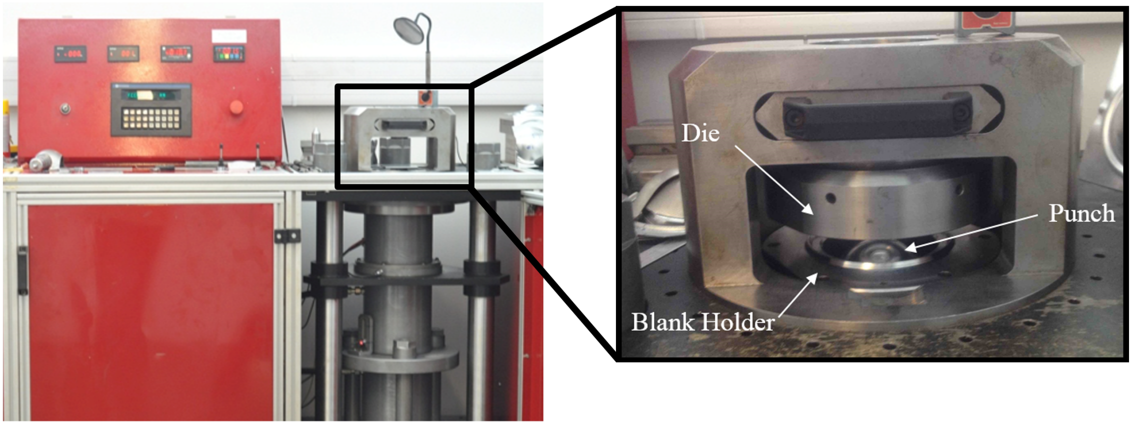

Figure 3.31: Universal testing machine used for Nakajima test and FLD determination.

The experimental points present in the diagram are obtained by measuring a grid with circles applied on the surface of the sheet metal. With the plastic deformation, the circles become ellipses (stretching zone) or increase their diameter (biaxial expansion zone), as shown in figure 3.32.

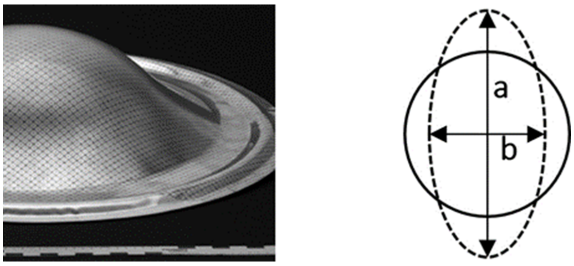

Figure 3.32: Measurement of true principal strains using a grid of circles.

The methodology of experimental determination of the major and minor strains values on the sheet metal surface was performed by measuring a selected reference circle previously and comparing with measurement after the plastic deformation of necking or fracture. The true major and minor strains are determined by the following equations:

$$\varepsilon_{major} = ln\left(\frac{a}{d_0}\right) \tag{3.14}$$

$$\varepsilon_{minor} = ln\left(\frac{b}{d_0}\right) \tag{3.15}$$

where a and b are the major and minor dimensions on the ellipse, respectively, and d_0 the initial diameter of the reference circle.

The specimens defined for testing may vary according to the need and accuracy in the representation of material behavior, but the following widths provide satisfactory results: 25, 50, 75, 100, 125 and 175 mm [109, 110].

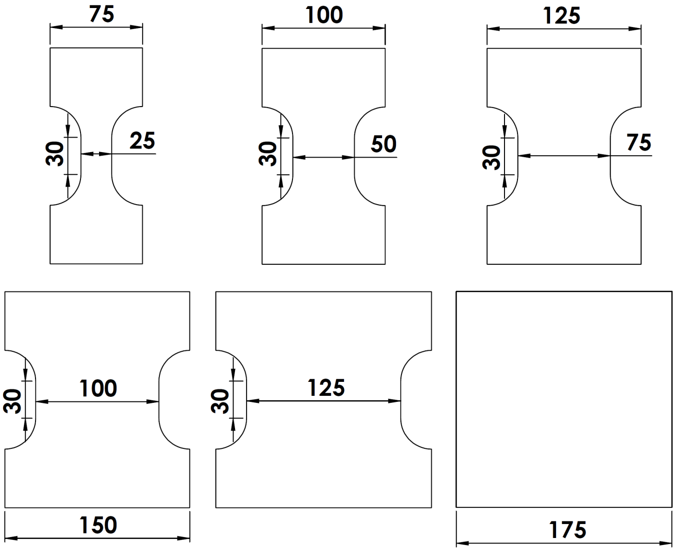

Figure 3.33: Specimen dimensions used in Nakajima experimental tests.

3.3.1.1 Forming limit diagram - FLD

All experimental tests were conducted on a hydraulic machine, as seen in figure 3.31, having the tooling setup with a punch, a die and a blank-holder. The friction between punch and blank was minimized by applying a Teflon foil at the top of the punch, in addition to a lubricant at the sheet surface (Ferrocoat N 6130). Necking or fracture visualization determined the moment to stop the test and proceed to strain measurements of the sample.

The determination of FLC can be done through several methods, but in this research, the method used was the so-called N^{o}5 of Zurich [111], which was set by International Deep Drawing Research Group (IDDRG). This method, which is a variant of Bragard method, applies to measurements performed on grids of tangled circles, applied in this study by an electrochemical etching process. For interpolation, it was followed the recommendation of using the circles whose deformation differences of adjacent circles is less than 5%.

The obtained experimental data points are represented by a curve that has been adjusted using the least squares approximation approach. This methodology performs a fitting for the stretch region and another fitting for the expansion region. Figure 3.34 shows the forming limit curves of the selected dual-phase steels and the corresponding experimental points.

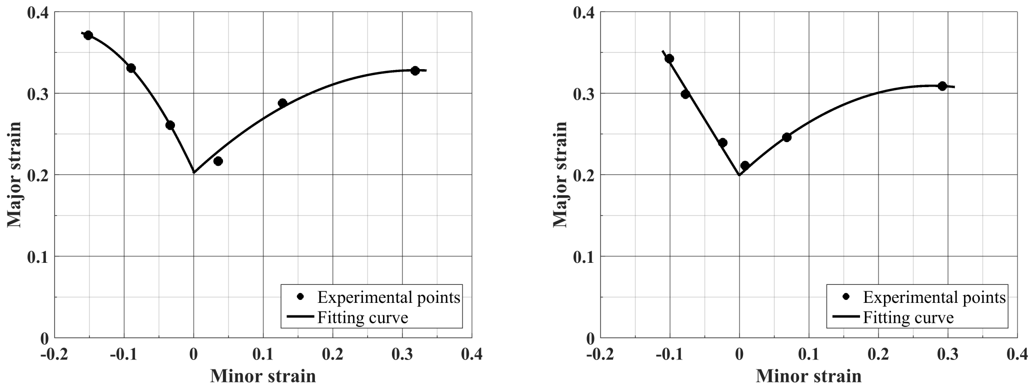

(a) DP500

(b) DP600

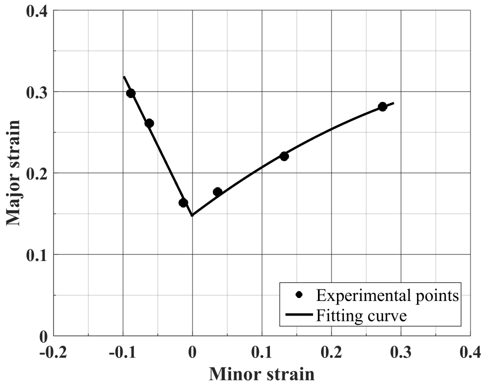

(c) DP780

Figure 3.34: Forming limit curve and corresponding experimental points for the selected materials.

The obtained punch force vs. punch displacement curves are shown in figure 3.35.

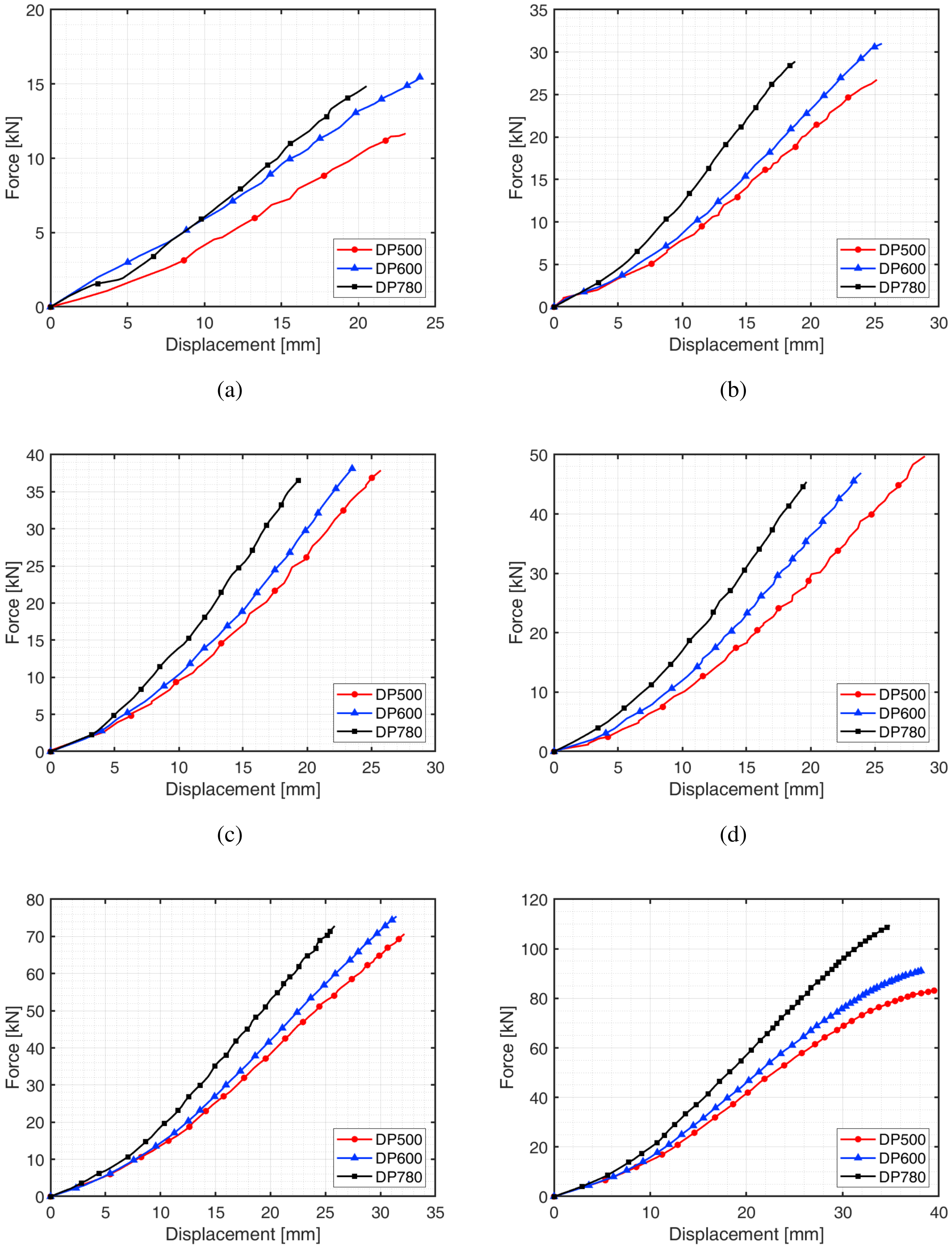

(a)

(b)

(c)

(d)

(e)

(f)

Figure 3.35: Punch force evolution with displacement of each dual-phase steel for the blank widths: a) 25 mm; b) 50 mm; c) 75 mm; d) 100 mm; e) 125 mm; f) 175 mm.

3.3.2 Deep drawing cylindrical cup test

In order to determine the limit drawing ratio (LDR) and evaluate the drawability of the dual-phase materials, experimental deep drawing cylindrical cup tests were performed using a hydraulic testing machine, as shown in figure 3.36(a). The tool setup is composed by four parts: a die, a flat blank holder, a cylindrical punch and a stopper. The punch has 60 mm of diameter while the die diameter is 62.4 mm with a 10 mm radius (figure 3.36(b)).

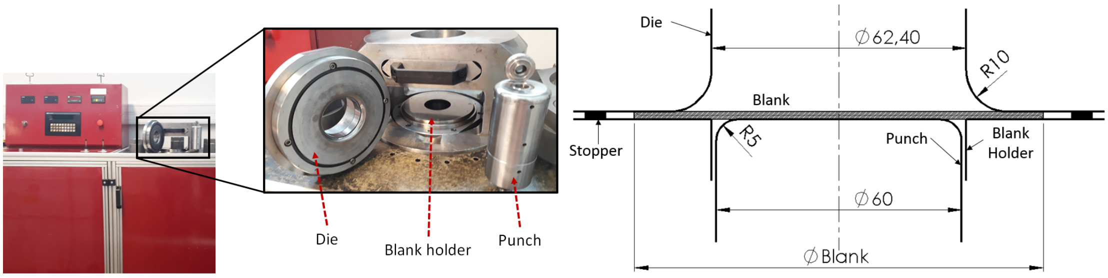

(a) (b)

Figure 3.36: a) Deep drawing cylindrical cup experimental setup; b) tool dimensions in mm.

Limiting drawing ratio (LDR) is defined as the ratio (equation 3.16) between the highest circular blank diameter ($D_{blank_{max}}$) that can be drawn into a cylindrical cup without fracture and the selected punch diameter (D_{punch}).

$$LDR = \frac{D_{blank_{max}}}{D_{punch}} \tag{3.16}$$

Different methodologies can be used to determine the material limiting drawing ratio. One method is drawing several cups, increasing the drawing ratio by small amounts until the limiting drawing ratio is reached. Another method is using the maximum obtained drawing punch force for each defined blank diameter, as presented in figure 3.37.

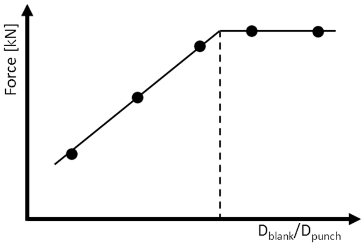

Figure 3.37: Drawing force as a function of blank and punch diameter ratio.

The last method was used since a lower number of experiments is needed to determine the critical blank diameter. The criterion to obtain the LDR is to plot the maximum drawing force as a function of the ratio between blank and punch diameters, as well as, the maximum force attained when fracture occurs.

It is expected that the required force to draw a cup increases linearly with blank diameter until the critical value is exceeded. A horizontal line represents the maximum attained punch force when fracture will occur and the intersection point between the two lines indicates the limiting drawing ratio of the tested material.

To performed the deep drawing cylindrical cup tests, circular specimens with different initial diameters were defined in order to determine the critical drawing diameter for each material. The minimum blank diameter is 105 mm and increments of 10 mm are considered up to the maximum diameter of 135 mm. A stopper ring was produced from the same sheet material of the blank (same thickness), and the purpose is to keep a minimum gap between the blank holder and die, thus preventing or minimizing ironing of blank flanges at the final stage of deep drawing. During the experimental tests, a lubricant was applied to both sides of the circular blank to reduce the friction forces between the blank and tools contact surfaces. The corresponding experimental conditions of the cylindrical cup tests are presented in table 3.15.

Table 3.15: Experimental conditions of deep drawing cylindrical cup tests.

Specimen diameters	105, 115, 125, 135 and additionally 130 mm			
Punch speed	5 mm/s			
Blank holder force		DP500	DP600	DP780
	ϕ105	50 kN	75 kN	75 kN
	ϕ115	75 kN	100 kN	105 kN
	ϕ125	100 kN	110 kN	115 kN
	ϕ135 and ϕ130	100 kN	110 kN	115 kN
Lubricant conditions	15 g/m2 of oil (FERROCOAT N6130)			
Environmental temperature	24 °C			
Humidity	52%			

3.3.2.1 Limit drawing ration - LDR

For the first three initial blank diameters (105, 115 and 125 mm) a fully drawn cup (figure 3.38) was successfully obtained for each dual-phase steel. The experimental evolution of punch force during the cup drawing was measured, as well as, the corresponding displacement for each material and for each defined blank diameter. The obtained punch force vs. punch displacement curves are shown in figure 3.39.

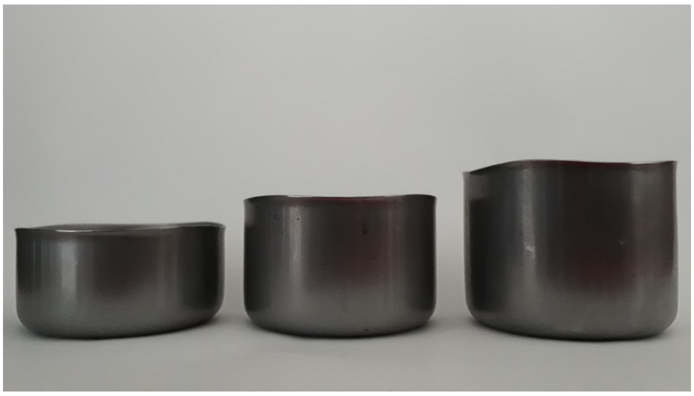

Figure 3.38: Cylindrical cups obtained for DP780 material using a blank diameter of 105, 115 and 125 mm (left to right, respectively).

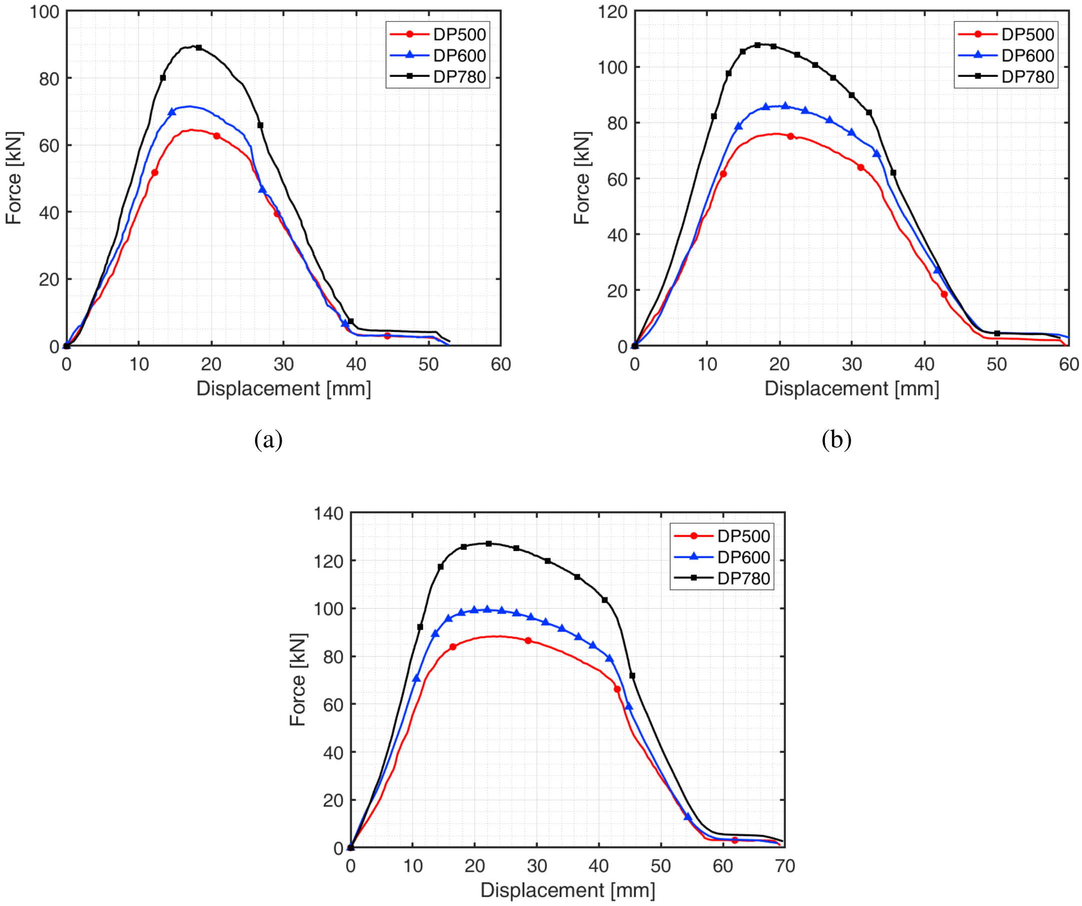

(a) (b)

(c)

Figure 3.39: Punch force evolution with displacement of each dual-phase steel for the blank diameters: a) 105 mm; b) 115 mm; c) 125 mm.

As seen, all the curves for punch force vs. displacement show a similar behavior, wherein DP780 needs a higher punch force in this drawing operation, due to its higher strength, as expected.

When the blank diameter is increased from 125 to 135 mm, it is not possible to draw a cup and fracture occurs near to the punch radius. To reduce the range where the critical diameter would be, the initial blank diameter was decreased from 135 mm to 130 mm and the same result of fracture was obtained, as shown in figure 3.40.

Figure 3.40: Fracture experimental cases when the critical blank diameter was exceeded (DP780 using the blank diameters of 135 mm and 130 mm, left to right, respectively.

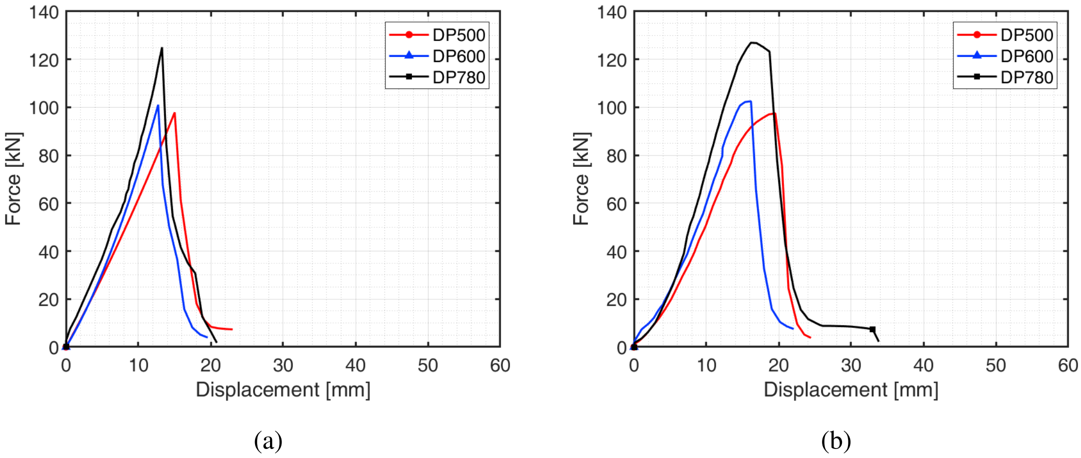

Figure 3.41: Punch force evolution with displacement of each dual-phase steel for the blank diameters: a) 135 mm; b) 130 mm.

This means that the limiting drawing blank diameter should lie between 125 and 130 mm. The corresponding force vs. displacement curves plotted for each blank diameter, are presented in figure 3.41.

Considering the punch force as function of displacement curves for every case, a linear regression is fitted to the maximum punch force of the fully drawn cups, which intersects a horizontal line that corresponds to the maximum load of fracture experiments. The intersection point gives the limiting drawing ratio of the material. Figure 3.42 presents the obtained drawability limits based on the deep drawing cylindrical cup test for each dual-phase steel.

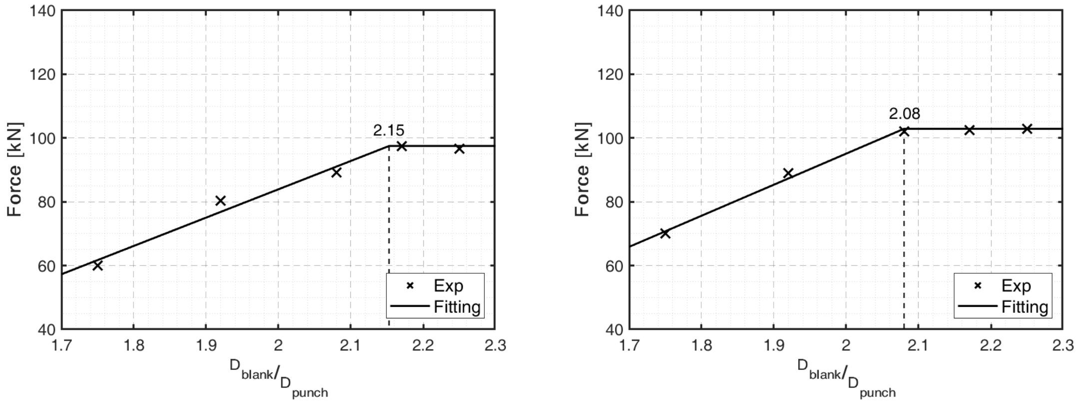

(a) DP500

(b) DP600

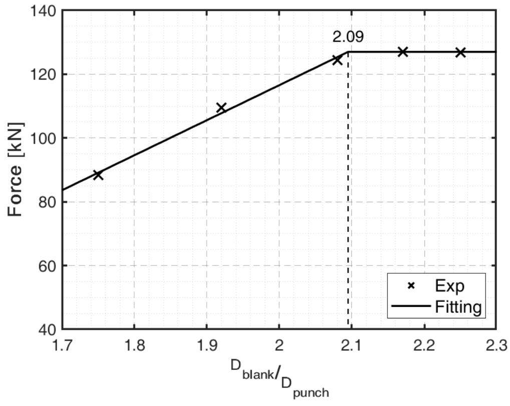

(c) DP780

Figure 3.42: Maximum drawing force as a function of blank and punch diameter ratio.

As mentioned by ASTM E517 standard [82], the average normal anisotropy, $\bar{r}$ parameter, is considered a measure of material drawability. With this in mind, it is possible to observe that the DP500 shows a higher limiting drawing ratio (LDR=2.15), when compared to other DP steels (2.08 for DP600 and 2.09 for DP780), which is consistent with the higher value of planar anisotropy.

3.3.2.2 Earing profiles

Another evaluated result was the earing profile of the cups, which was measured taking as reference the flat bottom of the cup. For this analysis and comparison the blank diameter of 125 mm was selected. The measurements and results will correspond to the cup height, as defined in figure 3.43, with the evolution of the angular direction, as shown in the same figure (anti-clockwise).

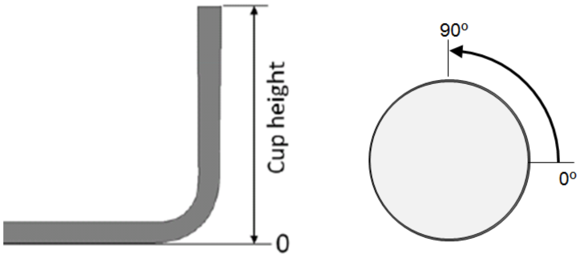

Figure 3.43: The ear height profiles were measured around the cup circumference starting from rolling direction (RD=0°); three anti-clockwise rotations (full 360°) were performed for each cylindrical cup.

The cylindrical cups were measured using a digital dial gauge micrometer and rotating them by means of an electric motor. The corresponding setup is presented in figure 3.44. The measurements acquired with the digital dial gauge micrometer are relative measurements, with the zero-height defined for 0° to the rolling direction. Therefore, additional measurements were needed, in order to obtain the total cup height as defined in figure 3.43. Such additional measurements were acquired using a High Precision Height Gauge, Mitutoyo Heightmatic 600 mm.

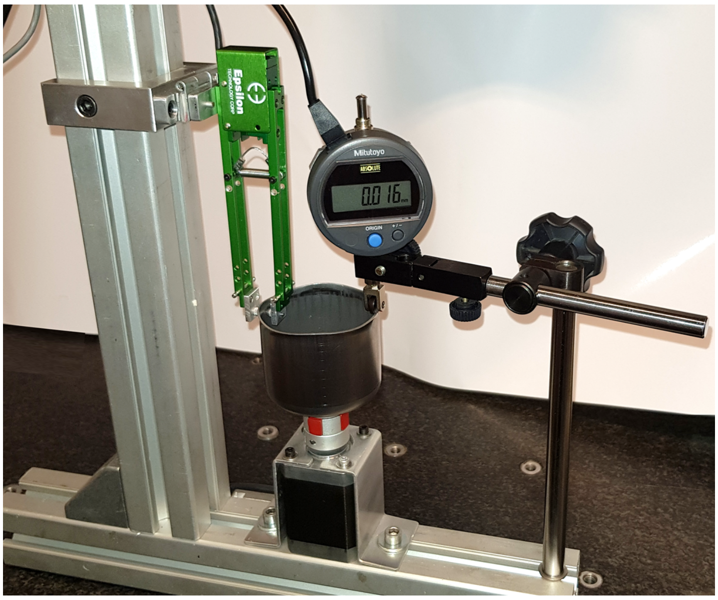

Figure 3.44: Setup for measuring the earing height evolution: the cup is rotated using an electric motor while a digital dial gauge micrometer acquires the data.

In figure 3.45 the obtained height of cup ears are presented, for each dual-phase steel material, considering the initial blank diameter of 125 mm.

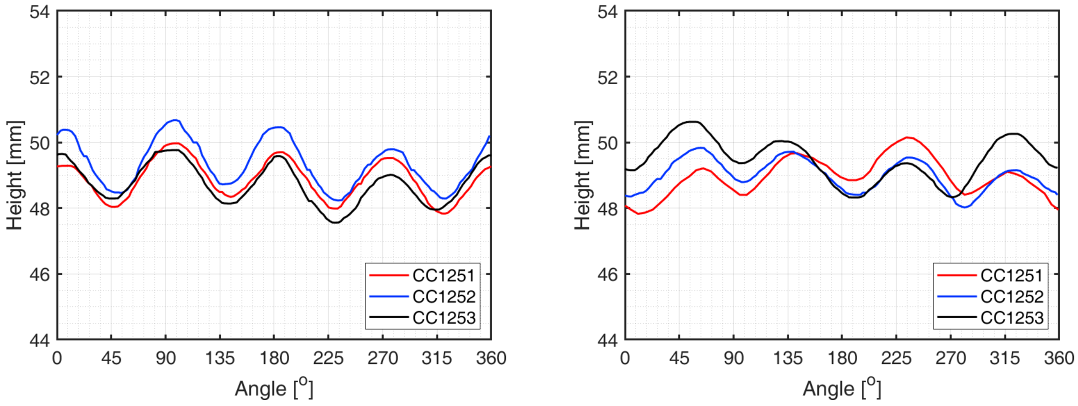

(a) DP500 (b) DP600

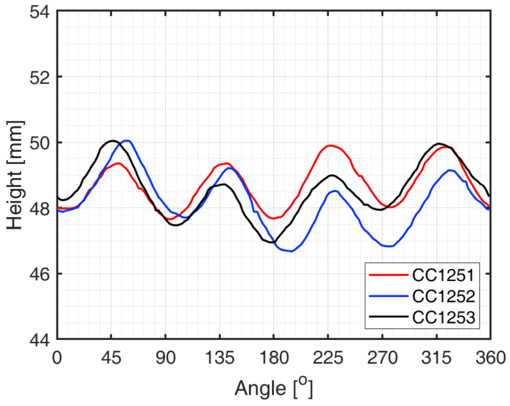

(c) DP780

Figure 3.45: Earing profile for 125 mm blank diameter.

DP500 shows a lower ear height for 45° relative to the rolling direction for both drawing diameters, but the other two materials show a higher value for the same angle. This behaviour is related with the anisotropy coefficient evolution, where the DP600 and DP780 have a similar tendency as opposed to the DP500.

Being considered the planar anisotropy (Δr) a measure of tendency to form ears in the cylindrical cup flange along the direction of the higher r-value [82], the obtained results show a good agreement with the experimentally obtained planar anisotropy coefficients for each material.

The DP500 steel has the highest ear height at 90° relative to the rolling direction, while the both DP600 and DP780 have the highest ear at 45°.

3.3.2.3 Wall thickness distribution

The anisotropy of the material leads to a non-uniform thickness distribution of the cylindrical cup. In this section, a experimental measurement of the thickness distribution of the cup wall is presented, for the final stage of the deep drawing process. Two approaches were considered (figure 3.46): first method corresponds to measurements on sections from planes through cup axis (vertical sections), along rolling, transverse and diagonal; the second method refers to measurements for sections on planes normal to cup axis (horizontal circular sections) and different cup heights.

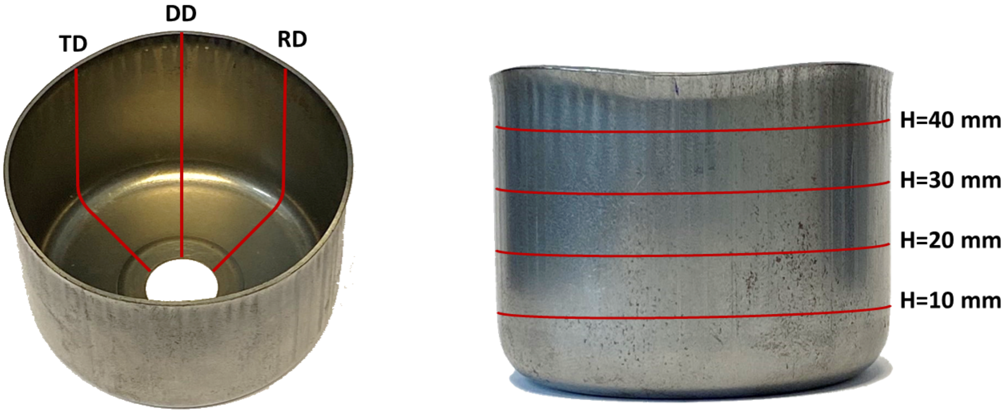

(a) Measurements on sections from planes through cup axis (vertical sections)

(b) Measurements for sections on planes normal to cup axis (horizontal circular sections) and different cup heights

Figure 3.46: Defined sections used to perform the cup thickness measurements.

The sections along perimeter are spaced 5 mm height apart (figure 3.46 only shows 10 mm height apart), with the first cutting section starting at a distance of 10 mm from the base of the cylindrical cup up to 45 mm.

Figure 3.47 shows the behavior of the thickness distribution for the different sections. Considering the figures 3.45 and 3.47, the cup thickness value is related to the section cup height, i.e., a higher wall thickness corresponds to a lower ear height. As seen, the thickness distribution for a height of 45 mm, which is the closest defined section to the cup border, presents a smoother wave behavior when compared with the earing cup profile.

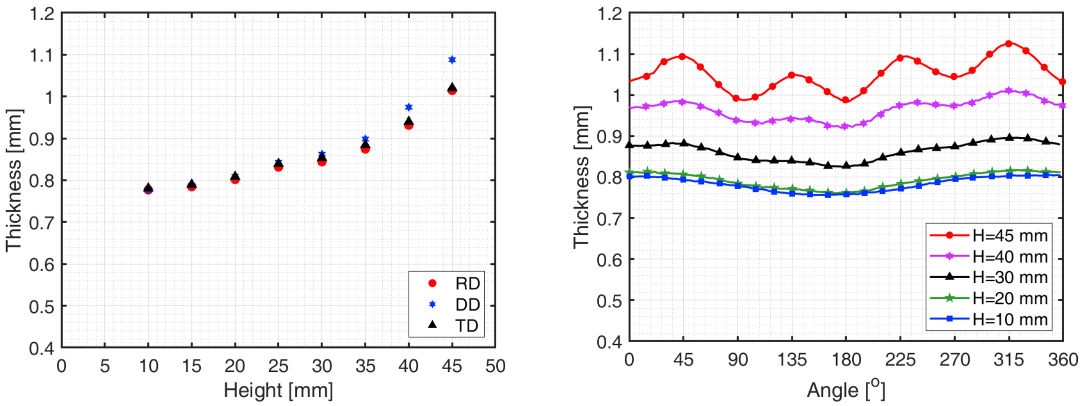

(a) DP500

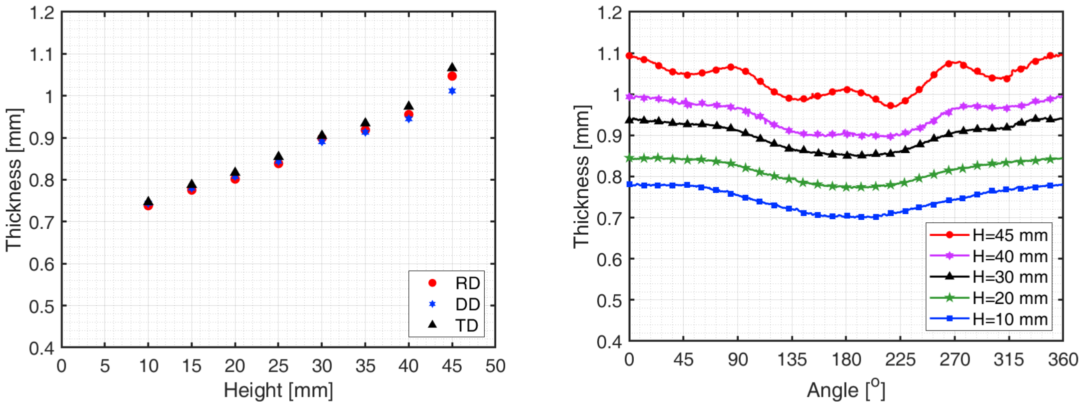

(b) DP600

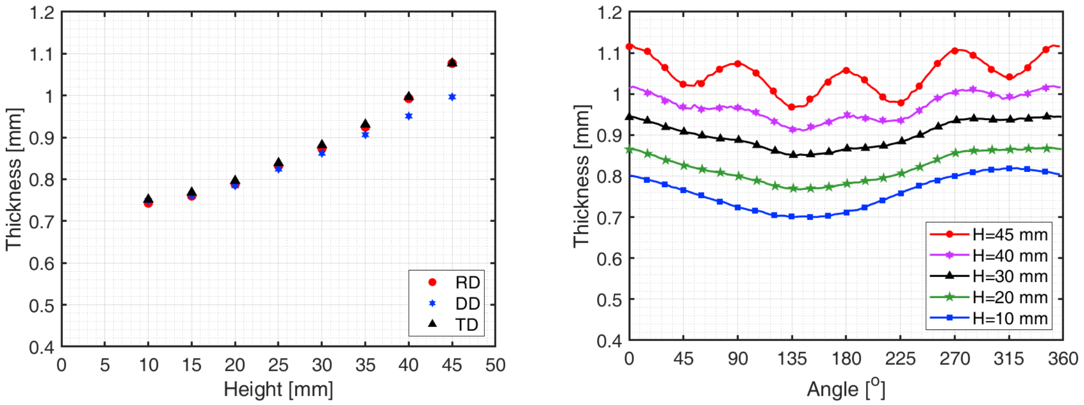

(c) DP780

Figure 3.47: Thickness distribution for vertical section (left) and circular section (right) for DP500, DP600 and DP780 cups (initial blank size = 125 mm).

3.3.3 Fracture at low triaxiality levels

The classic forming limit diagrams can not provide information about the material formability limits for lower values of stress triaxiality, such a shear stress state. The acquired results will allow an improvement in the description of the material behavior using the ductile damage models, especially for the Johnson-Cook (JC) and Hosford-Coulomb (HC) models, since the GTN cannot predict fracture for shear stress states.

In order to obtain the critical strains for a shear loading condition, a specific specimen geometry was considered and used. The geometry of the specimens, shown in figure 3.48(b), was based on the work of [112] and obtained by machining a rectangular strip. The experimental conditions of the test are given in table 3.16.

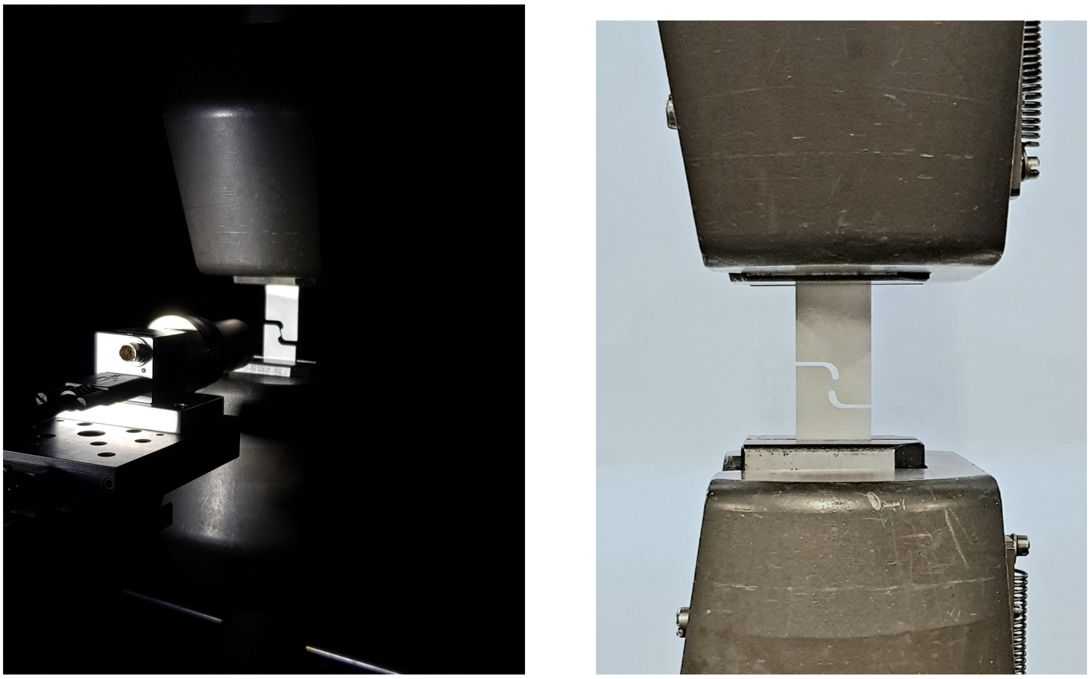

(a) Specimen and DIC camera

(b) Specimen geometry and setup

Figure 3.48: Experimental setup used to perform the shear loading a specific specimen geometry.

Table 3.16: Experimental conditions of shear tests.

Crosshead speed (grip)	0.4 mm/min
Data acquisition	5 Hz
Temperature	24 ^{o}C
Relative humidity	49%

All experiments were performed at room temperature with a constant crosshead speed on a INSTRON 5900R testing machine with a 5 kN load cell. For the acquisition of strain field, the digital image correlation was considered. Due to the size of the in-plane reading area, the average speckle size is lower than 15 μm. The DIC images were taken with a 5 MPixel camera (Basler acA2440-75um, 2448x2048 pixels) in conjunction with a telecentric lens (Infaimon OPE-TC-23-09, 45 mm). The commercial software VIC-2D.v6 was used to compute the equivalent strain. The obtained force vs. displacement curves of the shear loading are presented in figures 3.49, 3.50 and 3.51.

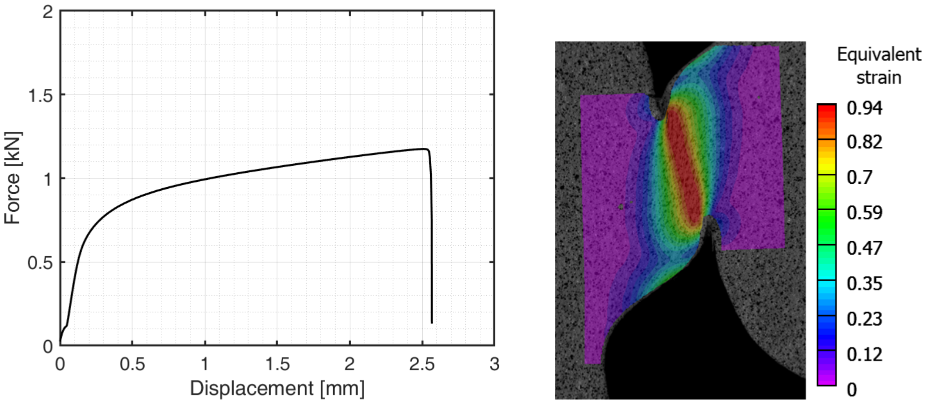

(a) Engineering stress-strain curve (b) Equivalent strain field

Figure 3.49: Force displacement curves and strain field obtained from DP500 shear loading.

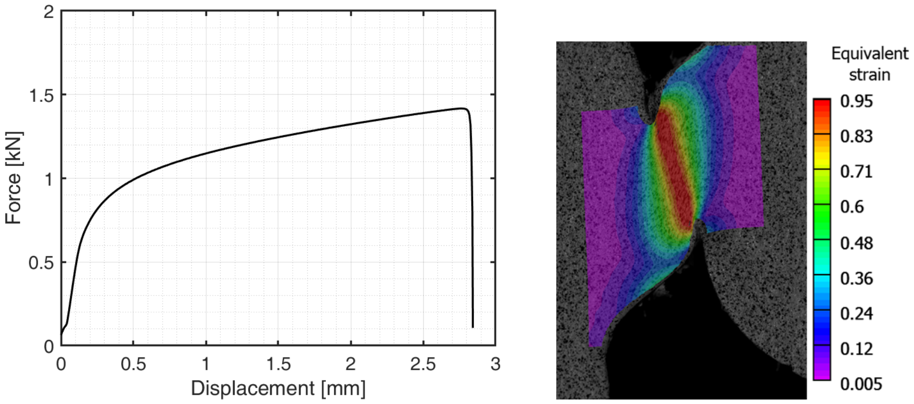

(a) Engineering stress-strain curve (b) Equivalent strain field

Figure 3.50: Force displacement curves and strain field obtained from DP600 shear loading.

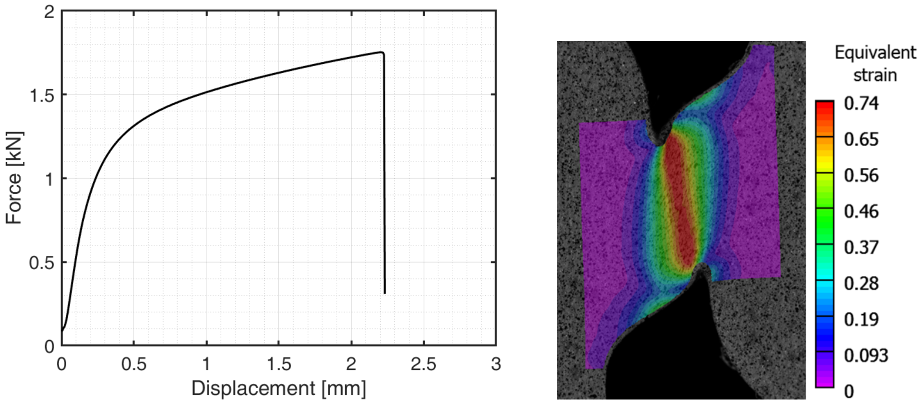

(a) Engineering stress-strain curve (b) Equivalent strain field

Figure 3.51: Force displacement curves and strain field obtained from DP780 shear loading.

Figures 3.49, 3.50 and 3.51 show that the current dual-phase steels present a higher forming limit for a shear stress loading state. It is also observed that the DP500 and DP600 have the same value of equivalent strain, 0.94 and 0.95 respectively, just before the final fracture moment. Also, the DP780 is the material that presents a lower measured strain limit (0.74).

Chapter 4

Identification of constitutive parameters

This chapter is dedicated to the identification process of developed and implemented constitutive model parameters and corresponding material behavior modeling. Isotropic hardening laws are defined, as well as the yield criteria to reproduce the anisotropic behavior. Besides, ductile damage models are defined and considered to predict the degradation of material strength.

(This page was deliberately left blank)

4.1 Optimization procedure and objective function

One of the crucial points for an accurate description of the material's behavior through constitutive models is the correct identification of the associated parameters. This task can be accomplished by adjusting the numerical prediction results to the experimental data using optimization methods, in which the main objective is the minimization of an objective function, as shown in the scheme of figure 4.1 that was implemented in the MATLAB® program.

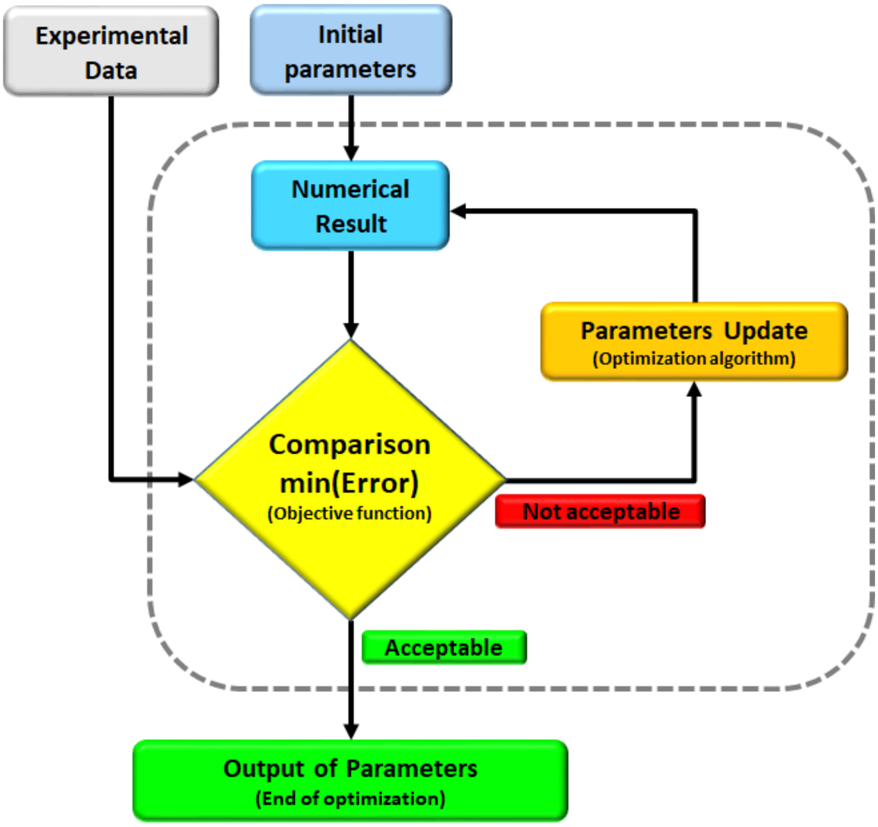

Figure 4.1: Flow chart describing parameter identification based on optimization algorithms and minimization of the error between numerical predictions and experimental values.

In this work, different algorithms were selected and implemented according to the parameters to be identified. In the case of hardening laws, the *fminsearch* function (available in the MATLAB command library) was chosen, in which it finds the minimum of the mean square error (*MSE*) between the hardening law prediction data and the experimental stress-strain curve obtained from the combination of tensile and bulge tests results, by varying the constitutive parameters. The method works independently on how many unknown variables must be identified. The *fminsearch* function uses the Nelder-Mead simplex direct search method algorithm, which does not use numerical or analytic gradients [113].

The identification of the yield criteria parameters is based in the experimental yield stresses (table 3.4 and table 3.10) and the anisotropic coefficients (table 3.6). For the Hill'48 yield criterion, the explicit expressions were used to identify the parameters, nonetheless, in the case of the Yld'91 and CPB06 yield criteria, a Genetic Algorithm was used to minimize an objective function, given the large number of possibilities that exist to minimize the objective function and local minimums. Since the error associated with the yield stresses is higher than the r-values error, the normalized yield stresses were adopted, having the yield stress according to the rolling direction as a reference value.

A similar methodology was adopted in the parameter identification process of the ductile damage models. The goal is the minimization of an objective function, considering the difference between the predicted and experimental strain at failure as a function of the stress triaxiality. However, for cases where no expression directly relates these two variables (without any mathematical manipulation), an inverse numerical analysis, using an optimization algorithm, was developed to obtain the parameters of the damage models. The inverse analysis, implemented on MATLAB®, uses an iterative procedure to obtain the best fitting parameter values that minimize the objective function, based on finite element numerical simulation results.

4.2 Flow curve

In order to predict the hardening behavior of the material for higher values of plastic strain when compared to those obtained by the uniaxial tensile test, constitutive models for hardening (also known as hardening laws) are used. These models react to the evolution of the yield surface, which is characterized by the equivalent stress and depends on the internal variable's evolution of the material.

Since the data from the hydraulic bulge test was considered in this work, the description of the hardening curve had a significant improvement, minimizing the errors that result from extrapolation. The flow curve obtained from the combination of the uniaxial tensile test results with the bulge test data will be used as a reference base for the identification of hardening law parameters. Additionally, a comparison will also be performed between using only the uniaxial tensile test data and the hardening curve that combines the tensile and bulge stress-strain curves.

The identification of parameters for constitutive model is carried out using the optimization method presented in the previous section, implemented in the MATLAB® tool.

Tables 4.1 to 4.3 present the identified parameters for each material. It should be noted that only a few hardening laws were considered, some of them choosen due to its widespread use.

Table 4.1: Identified parameters for hardening laws for DP500, based on experimental stress-strain data.

Hardening law	Parameters				$\sigma_{Y\,(\bar{\varepsilon}^p=0)}$ $[MPa]$
Hollomon	K=829.60		n=0.1336		—
Voce	A=380.80	B=343.03	C=11.303		380.8
Swift	K=832	ε_0=0.0032	n=0.1370		378.6
Swift-Voce	α=0.4502	K=1297.14	ε_0=0.0030	n=0.1455	379
		A=232.87	B=165.13	C=12.065	

Table 4.2: Identified parameters for hardening laws for DP600, based on experimental stress-strain data.

Hardening law	Parameters				$\sigma_{Y\,(\bar{\varepsilon}^p=0)}$ $[MPa]$
Hollomon	K=972.48		n=0.1389		—
Voce	A=432.74	B=405.38	C=11.648		432.7
Swift	K=975.73	ε_0=0.0032	n=0.1426		430.5
Swift-Voce	α=0.4086	K=1328.42	ε_0=0.0021	n=0.2035	430.9
		A=468.13	B=205.85	C=13.588	

Table 4.3: Identified parameters for hardening laws for DP780, based on experimental stress-strain data.

Hardening law	Parameters				$\sigma_{Y\,(\bar{\varepsilon}^p=0)}$ $[MPa]$
Hollomon	K=1164.23		n=0.1155		—
Voce	A=523.26	B=469.85	C=18.149		523.3
Swift	K=1164.25	ε_0=0.0010	n=0.1161		519.1
Swift-Voce	α=0.8328	K=1674.54	ε_0=0.0019	n=0.0530	519.1
		A=-2875.23	B=1051.28	C=18.438	

Considering the parameters presented in tables 4.1 to 4.3, the corresponding hardening evolution curves were plotted and they are shown in figure 4.2.

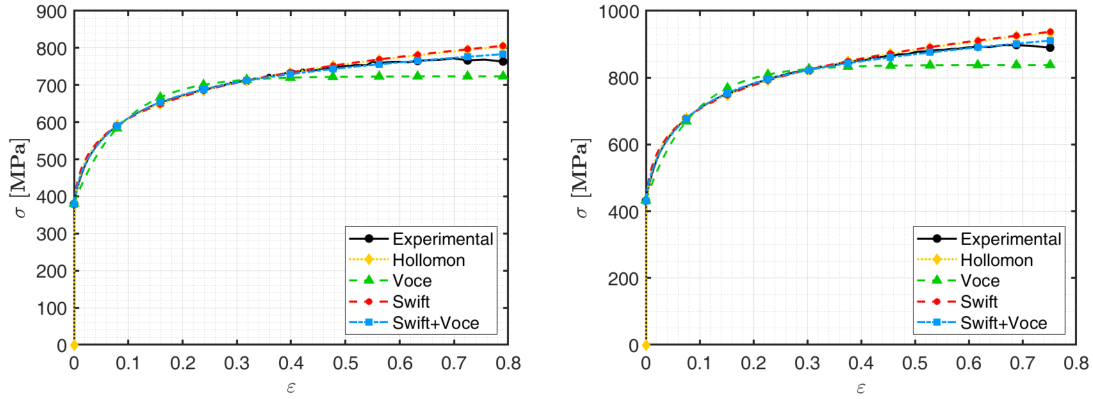

(a) DP500 (b) DP600

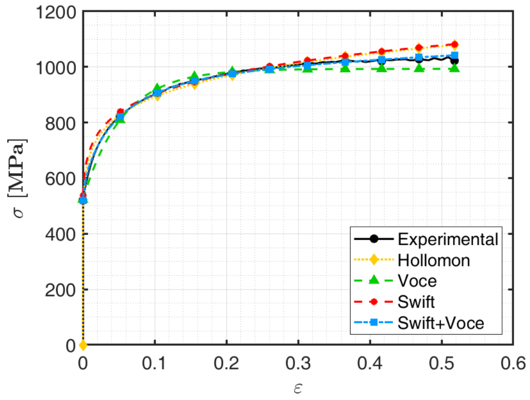

(c) DP780

Figure 4.2: Comparison between the equivalent stress-strain curve and hardening laws, for the different materials.

As seen in figure 4.2, the hardening behavior of the dual-phase steels for higher values of plastic strain is better characterized by the combined Swift+Voce law (equation 2.7). However, for some sheet metal forming processes, e.g. air bending, where the strain levels are below 0.4 for the DP500 and DP600, and 0.3 for the DP780, the hardening curve given by Swift law shows to be well suited. Hollomon law also describes the same behavior, although not being representative for very small strains, due to starting its curve from point (0,0).

Additionally, in order to analyze and evaluate the differences between using and not using the data from the hydraulic bulge test in the identification of parameters for the hardening law, a comparison with the constitutive models previously determined is performed and shown in figure 4.3.

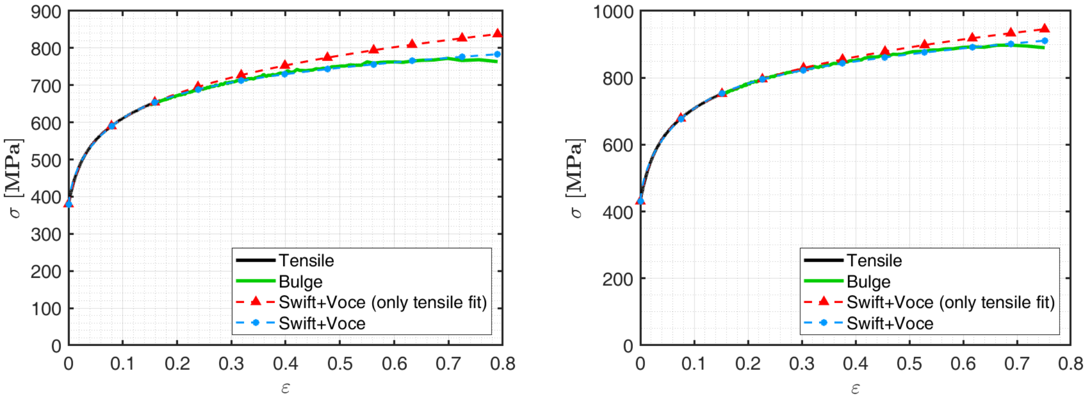

(a) DP500 (b) DP600

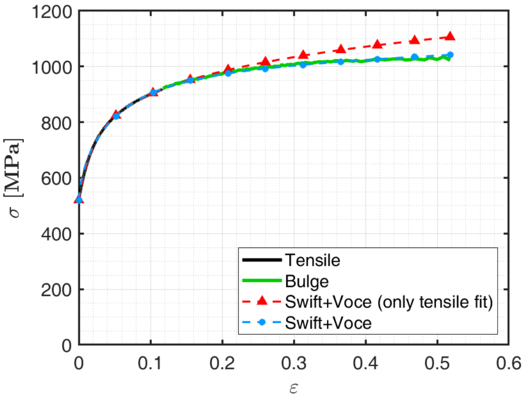

(c) DP780

Figure 4.3: Comparison of the equivalent stress-strain curve using additionally the data from the biaxial hydraulic bulge test in the selection of the constitutive model hardening law.

Based on figure 4.3, using only the data from the tensile test leads to a higher hardening of the material in the extrapolation zone. On the other hand, using the data from the biaxial bulge test, it is possible to improve the hardening prediction and getting higher accuracy to describe the material behavior.

4.3 Yield locus

To reproduce the material's mechanical behavior as close as possible, three different yield criteria were selected: Hill'48, Yld91 and CPB06. Additionally, it was considered a non-associated flow rule approach based on Hill'48 function, for both yield and potential surfaces.

In case of Hill'48 criterion the corresponding parameters can be identified based on stresses, using the expressions 2.26 and 2.25, and based on r-values considering the equation 2.27. For the NAFR approach, the parameters to describe the yield surface are based on stresses (Hill48 σ-based) and the parameters used to reproduce the potential surface are based on plastic anisotropic coefficients (Hill48 r-based). For the other models (Yld91 and CPB06), a Genetic Algorithm (GA) was used to minimize an objective function, which evaluates the difference between the predicted and experimental values. The considered material properties for the identification stage were:

- uniaxial tensile yield stresses: σ_0, $\sigma_{22.5}$, σ_{45}, $\sigma_{67.5}$, σ_{90}
- biaxial stress: σ_b
- uniaxial compression yield stresses: σ_0^c, σ_{90}^c
- plastic anisotropic coefficients (r-values): r_0, $r_{22.5}$, r_{45}, $r_{67.5}$, r_{90}
- plastic biaxial anisotropic coefficient: r_b

Some assumptions were established in the identification process for each criterion. The parameters associated with through-thickness material properties, which are quite challenging to assess in metallic sheets, were assumed to be equal to the isotropic condition value, which is the case of L and M equal to 1.5 for Hill'48, as well as, the anisotropy coefficients C_{44} and C_{55} of CPB06 and f and g of the Yld91 criterion assumed to be equal to 1. Also, for CPB06, the parameter C_{11} was considered constant and equal to 1, the parameter a equal to 2 and the variable k an average value result using the equation 2.49 and the two uniaxial compression yield stresses. The other CPB06 six parameters were identified for a range between ([-5 5]) [114]. The same applies to the four unknown parameters of the Yld91 criterion, where the range considered was from 0 to 5. The parameter m is equal to 6, since the studied materials are steels, having a Body Centered Cubic (BCC) crystal structure.

Table 4.4 presents a summary of the used experimental reference data, which it was already shown in section 3.2.

Table 4.4: Summary of experimental data used for yield criteria parameters identification.

	DP500	DP600	DP780
Uniaxial tensile yield stress			
σ_0	379.7	429.6	521.2
$\sigma_{22.5}$	403.8	427.3	540.8
σ_{45}	408.5	430.4	537.6
$\sigma_{67.5}$	401.3	436.6	543.7
σ_{90}	390.6	437	550
Biaxial stress			
σ_b	414.8	442.6	585.1
Uniaxial compression yield stress			
σ_0^c	346.7	381	509.1
σ_{90}^c	358.7	386.2	534
Plastic anisotropic coefficient			
r_0	0.971	0.695	0.648
$r_{22.5}$	0.888	0.783	0.802
r_{45}	0.851	0.935	0.922
$r_{67.5}$	1.002	0.899	0.891
r_{90}	1.11	0.811	0.824
Plastic biaxial anisotropic coefficient			
r_b	0.96	0.92	0.91

The obtained values for the three dual-phase steels are presented in tables 4.5, 4.6 and 4.7 for DP500, DP600 and DP780, respectively. The corresponding contours of the yield surfaces and predicted normalized yield stresses and r-values, as well as the initial yield and potential surfaces for the NAFR approach are presented in figures 4.4, 4.5 and 4.6, respectively.

Table 4.5: Identified yield criteria parameters for DP500.

Hill48	F	G	H	N				
r-based	0.4438	0.5074	0.4926	1.2850				
σ-based	0.3914	0.4465	0.5535	1.3090				
Yld91	a	b	c	h	m			
	0.9538	1.0026	0.9914	0.9404	6			
CPB06	C11	C12	C13	C22	C23	C33	C66	k
	1	-0.6677	0.6056	1.0254	1.03	-1.0987	-1.5684	0.134

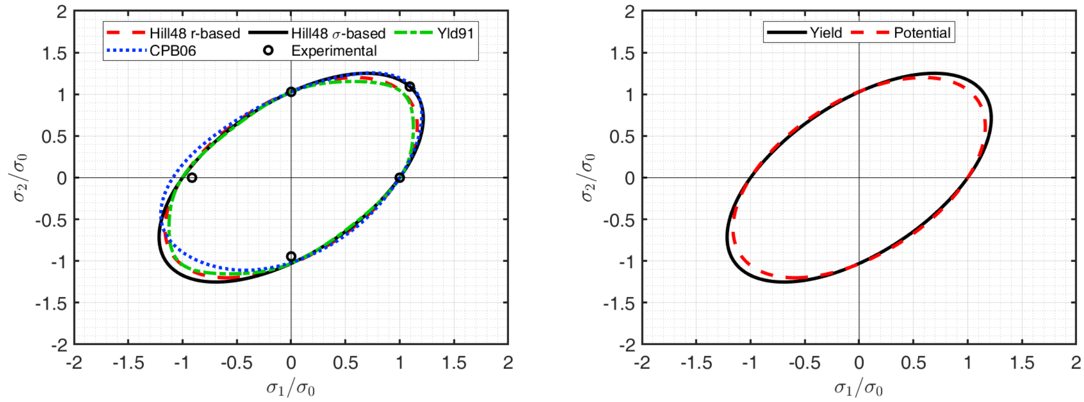

(a) Yield surface contours

(b) Initial NAFR yield and potential surface based on Hill'48

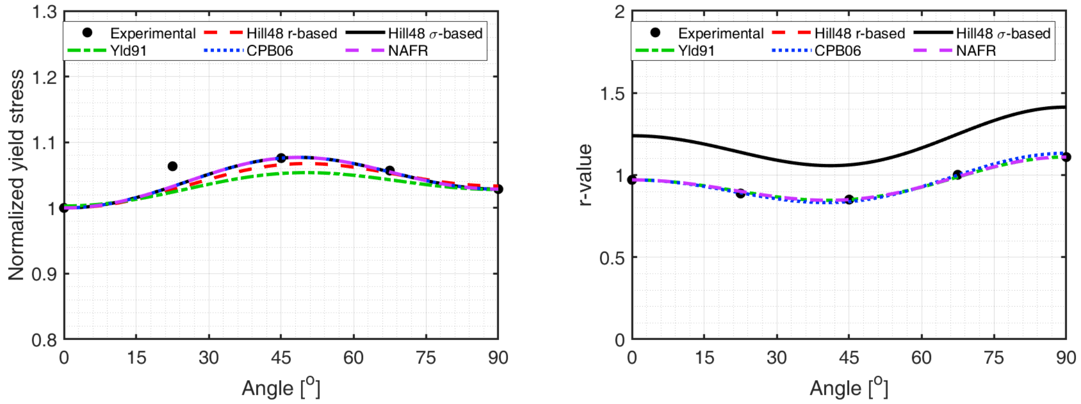

(c) Normalized yield stress evolution

(d) r-value evolution

Figure 4.4: Predicted yield surfaces and evolution of yield stresses and r-values of Hill'48, Yld91 and CPB06 models for DP500 steel.

Table 4.6: Identified yield criteria parameters for DP600.

Hill48	F	G	H	N				
r-based	0.5056	0.59	0.41	1.5721				
σ-based	0.4543	0.4878	0.5122	1.5215				
Yld91	a	b	c	h	m			
	1.0094	1.0621	0.9359	1.0187	6			
CPB06	C11	C12	C13	C22	C23	C33	C66	k
	1	-3.5067	-2.4307	0.8531	-2.3768	2.1045	4.1801	0.189

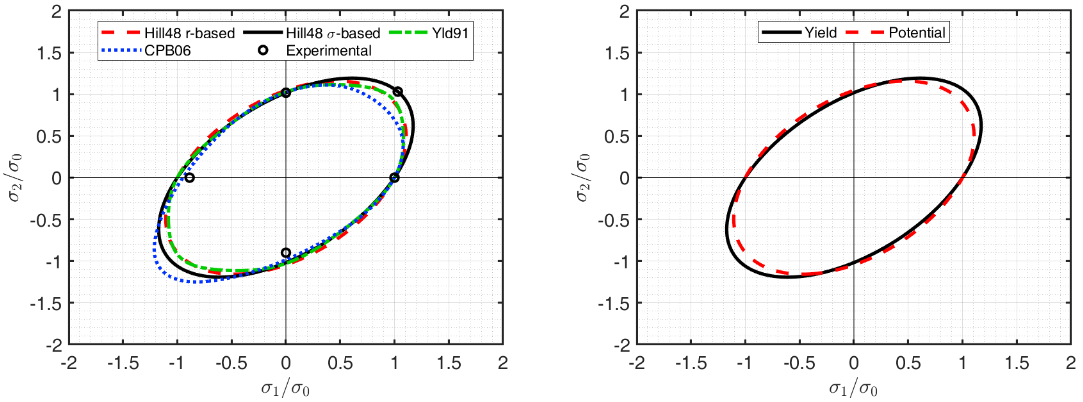

(a) Yield surface contours (b) Initial NAFR yield and potential surface based on Hill'48

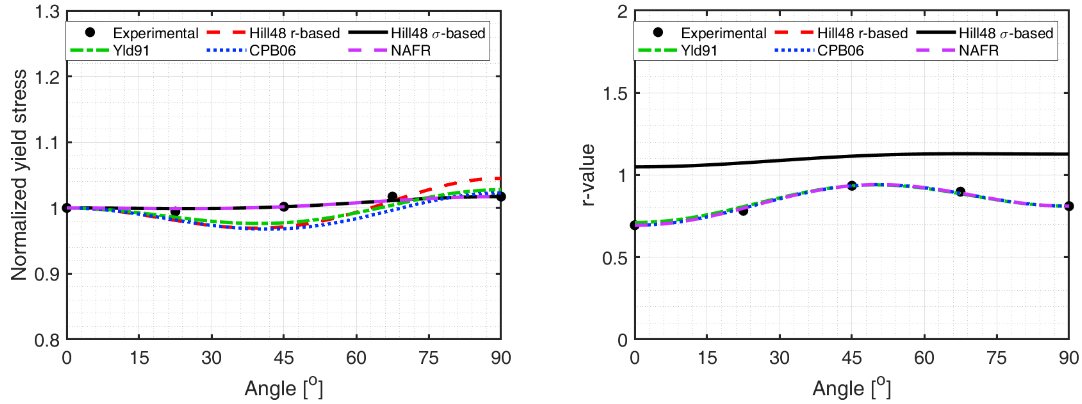

(c) Normalized yield stress evolution (d) r-value evolution

Figure 4.5: Predicted yield surfaces and evolution of yield stresses and r-values of Hill'48, Yld91 and CPB06 models for DP600 steel.

Table 4.7: Identified yield criteria parameters for DP780.

Hill48	F	G	H	N				
r-based	0.4772	0.6068	0.3932	1.5414				
σ-based	0.3458	0.4477	0.5523	1.4831				
Yld91	a	b	c	h	m			
	0.9797	1.0769	0.9150	1.008	6			
CPB06	C11	C12	C13	C22	C23	C33	C66	k
	1	-0.7924	-1.9396	0.7397	-0.6387	-2.8879	-2.0155	0.040

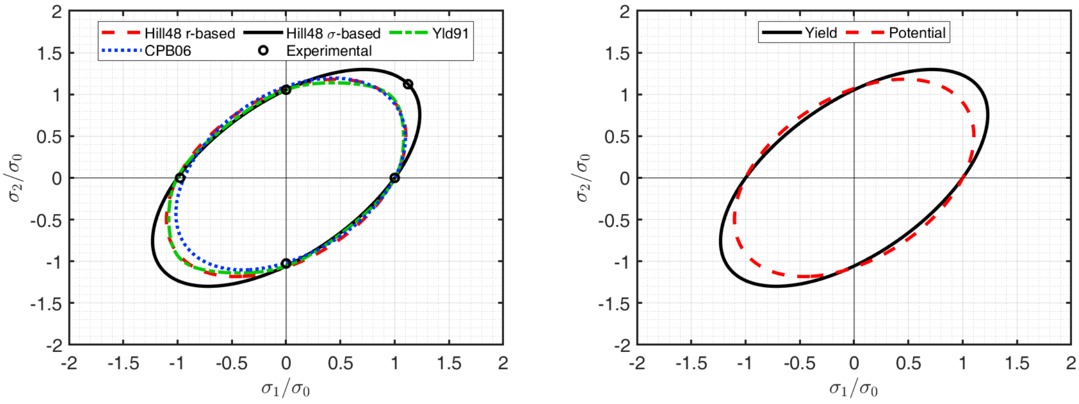

(a) Yield surface contours

(b) Initial NAFR yield and potential surface based on Hill'48

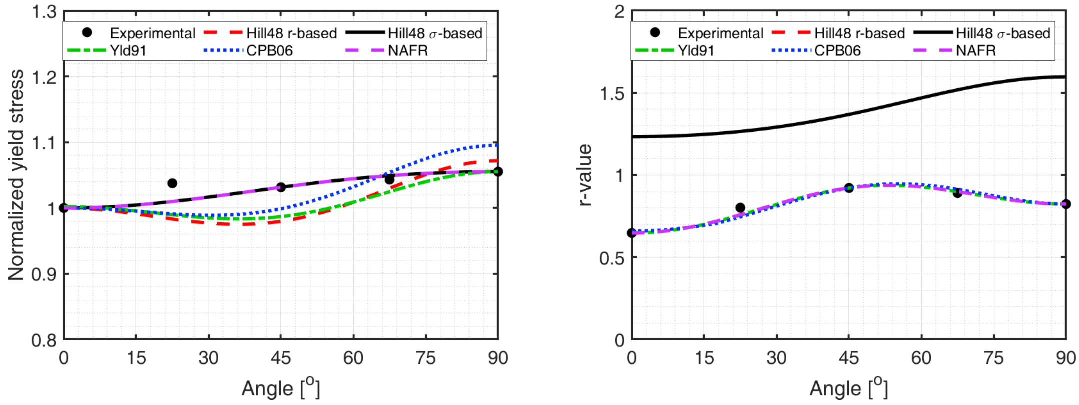

(c) Normalized yield stress evolution

(d) r-value evolution

Figure 4.6: Predicted yield surfaces and evolution of yield stresses and r-values of Hill'48, Yld91 and CPB06 models for DP780 stress.

As seen in figures 4.4, 4.5 and 4.6, all the selected yield criteria were able to describe and predict quite well the r-value evolution of DP600 and DP780, overlapping completely the experimental plastic anisotropic coefficient points, except for Hill'48 criterion using σ-based parameters. However, in the case of prediction for the yield stresses, distinct anisotropic behaviors can be observed. Yld91 criterion reproduced the DP600 yield stresses for 0^{o} and 90^{o} relative to the rolling direction but fails at 45^{o}, unlike the CPB06 prediction, being closer at 45^{o}. On the other hand, an opposite behavior of DP780 is observed for Yld91 and CPB06 predictions.

For DP500, the CPB06 yield criterion was capable of reproducing the yield stresses (except at 22.5^{o}) and r-value evolutions simultaneously, showing higher flexibility, like the NAFR approach. The Hill'48 σ-based clearly fails to reproduce r-value points, but it goes through experimental normalized yield stress values. In case of Yld91 and Hill'48 r-based, both can predict the plastic anisotropic coefficients, although Hill'48 r-based has a better performance than Yld91 to describe the normalized yield stresses, showing a closer 45^{o} prediction.

Regarding the yield surfaces, none of the yield criteria can reproduce completely every point of experimental data. The aptitude of CPB06 to reproduce the stress differential shows to be high, presenting a better and closer prediction of the uniaxial compression points, except for DP500, where an overestimation of σ_0^c was made. For the three dual-phase steels, Yld91 and Hill'48 r-based present similar yield surface shapes, inside of the Hill'48 σ-based yield surface, which was the only criterion passing through σ_b point, as well as, CPB06 for DP500.

In general, if an associated flow rule (AFR) is considered, the CPB06 yield criterion shows a good performance to reproduce closely the material anisotropic behavior, both normalized yield stress and plastic anisotropic coefficients. However, for an accurate prediction of such properties, the non-associated flow rule approach using the simple Hill'48 function seems to be an excellent option due to the ability to reproduce the normalized yield stresses and r-values independently and simultaneously. Both options have pros and cons, the CPB06 criterion can reproduce stress differential effects, while for the case of the NAFR method, the identification process of Hill'48 parameters is simpler and more explicit.

4.4 Damage criteria

To model the degradation of material strength during the deformation process, three ductile damage models were selected and their performance evaluated: GTN, Johnson-

Cook and Hosford-Coulomb. For the identification of the corresponding parameters, different methodologies where applied. In the case of Johnson-Cook damage model, the equation 2.79 was used in the minimization of the difference between the predicted and experimental strain at failure as a function of the stress triaxiality. The strain rate and temperature effects were not included and therefore parameters d_4 and d_5 are not defined.

For the Hosford-Coulomb damage model a more straight-forward approach is used, since it has explicit expressions (equation 2.83) to calculate the corresponding parameters.

To characterize the behavior of the material using the GTN damage model, seven parameters are needed, but a mutual correspondence can be considered [115]. According to literature, the parameters q_1, q_2 and S_N may be kept constant [116]. However, GTN damage model doesn not have a explicit relationship between stress triaxiality and the equivalent strain at fracture, therefore, an inverse finite element numerical analysis was performed to obtain the best fitting parameter. A finite element 3D explicit analysis for uniaxial tensile test and for hydraulic bulge test was created, having the damage model parameters as an input to the numerical simulation using Abaqus/Explicit code. Both numerical models use the same hardening behavior, according to the data presented in section 4.2.

The uniaxial tensile specimen was discretized by eight node solid elements with reduced integration (C3D8R type from Abaqus Library), having four elements through thickness. Due to the symmetry, only one quarter of the real setup was considered, as shown in figure 4.7(a). Material rolling direction is assumed to be along loading direction.

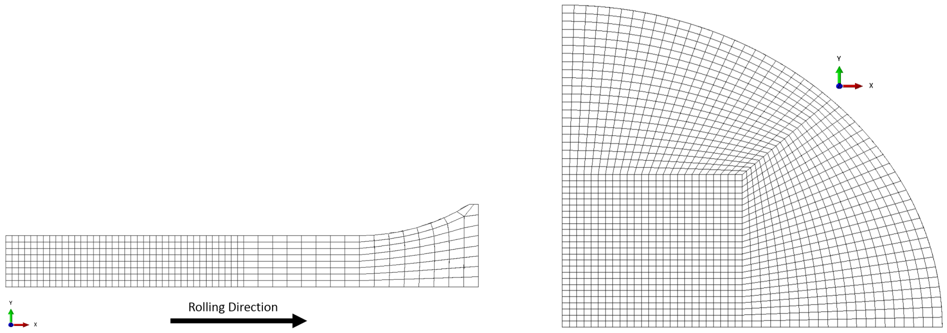

(a) Element size of 1x1x0.125 mm in uniform section

(b) Element size of 2x2x0.125 mm in central area

Figure 4.7: Uniaxial tensile and hydraulic bulge discretization used in the FE model.

In case of bulge test, a quarter of the model was modeled with discretization of four layers through thickness of eight node solid elements with reduced integration (C3D8R type from Abaqus Library), as shown in figure 4.7(b). The blank is subjected to a prescribed increasing linear increment pressure of 1 bar/s, in order to reproduce the same experimental conditions. The bulge test tools are discretized by analytical rigid surfaces. At each iteration, the damage model parameters are determined by comparing the numerical force vs. elongation curve of uniaxial tensile test with essential experimental data, and pressure vs. pole height behavior in the case of the hydraulic bulge test.

The validation of the predicted numerical results is ensured by the correlation with experimental data.

Tables 4.8, 4.9 and 4.10 present obtained parameters for every considered damage model in current thesis.

Table 4.8: Identified Johnson-Cook damage model parameters for the three dual-phase steels: DP500, DP600 and DP780.

Jonhson-Cook	d_1	d_2	d_3
DP500	0.667	0.273	-6.17
DP600	0.662	0.289	-5.99
DP780	0.428	0.313	-6.57

Table 4.9: Identified GTN damage model parameters for DP500 and DP780.

GTN	q_1	q_2	$q_3 = q_1^2$	f_0	f_C	f_F	ε_N	S_N	f_N
DP500	1.86	0.8	3.46	0.9998	0.01684	0.018	0.09	0.03	0.0104
DP780	1.76	0.83	3.10	0.9997	0.0239	0.026	0.085	0.2	0.0445

Table 4.10: Identified Hosford-Coulomb damage model parameters for the three dual-phase steels: DP500, DP600 and DP780.

Hosford-Coulomb	a	b	c	n
DP500	1.799	0.72	0.040	0.1
DP600	1.767	0.71	0.043	0.1
DP780	1.661	0.47	0.069	0.1

Figure 4.8 and figure 4.9 show the 3D surfaces of dual-phase steels for the identified Hosford-Coulomb damage model parameters and the evolution of the equivalent plastic strain as a function of the stress triaxiality for Hosford-Coulomb and Johnson-Cook damage models, respectively.

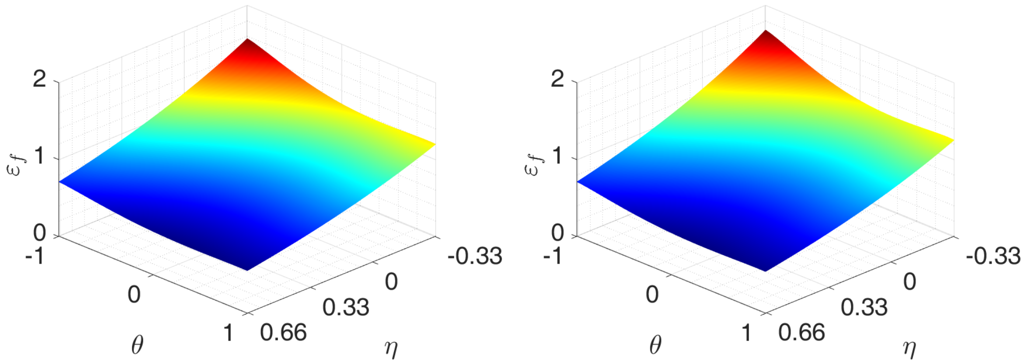

(a) DP500

(b) DP600

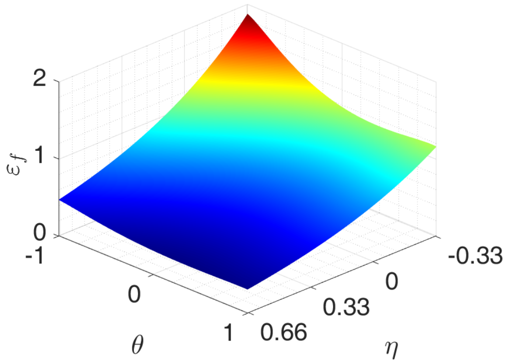

(c) DP780

Figure 4.8: Equivalent strain at fracture as a function of stress triaxiality and the Lode angle parameter, considering a proportional loading.

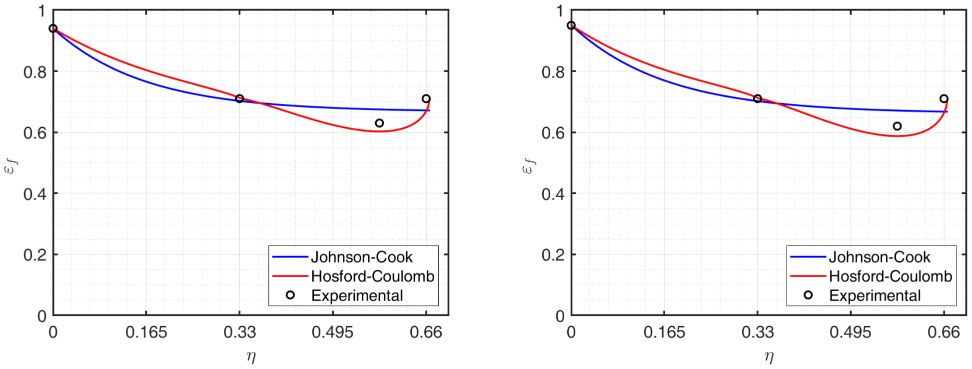

(a) DP500 (b) DP600

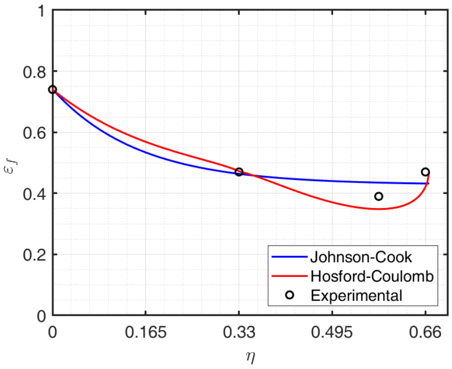

(c) DP780

Figure 4.9: Hosford-Coulomb and Johnson-Cook equivalent strain at fracture as a function of stress triaxiality considering a plane stress state.

(This page was deliberately left blank)

Chapter 5

Numerical simulation applied to stamping

In this chapter, the validation and assessment of the constitutive models are performed. A series of finite element numerical simulation were considered and applied to different forming conditions, such as deep drawing cylindrical cup, Nakajima test, hole expansion and a cross-die geometry. The aim was the prediction of the AHSS behavior using the previously obtained experimental data and the corresponding identified constitutive model parameters. A comparison between the numerical simulation results and the experimental data is also made.

(This page was deliberately left blank)

5.1 Cylindrical cup -Swift test

To evaluate the mechanical characterization and the considered yield criteria to describe the dual-phase steels behavior, a finite element model was created based on the experimental deep drawing cylindrical cup test, as shown in figure 3.36(b). The tool setup contains a stopper ring produced from the same sheet material and the same thickness, to prevent or reduce the pinching effect at the end of the cup drawing stage, by keeping a minimum gap between the die and blank holder. Additionally, the punch has an important feature, which allows the minimization of misalignment effects between the circular blank relative to the tools.

An explicit analysis of the deep drawing cup was considered using Abaqus/Explicit code to perform numerical simulations. Due to the symmetry of the test, only 1/4 of the experimental setup was taken into account to create a 3D finite element model (figure 5.1(a)).

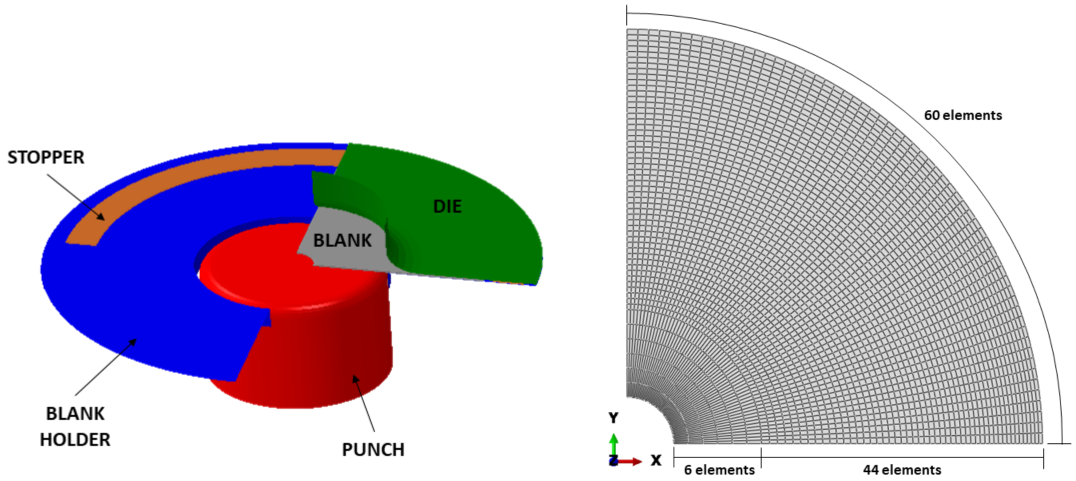

(a) (b)

Figure 5.1: Cylindrical cup test finite element 3D model: a) setup and position of tools and blank; b) blank mesh in XY plane.

The sheet blank and the stopper were discretized by three layers of eight node deformable elements with reduced integration (C3D8R type from Abaqus Library), being the tools (die, punch and blank holder) modeled as rigid analytic surfaces. The spacial discretization of blank XY plane can be seen in figure 5.1(b). A constant value of 0.05 was established to model the Coulomb friction between surfaces. Regarding the material modeling, the identified constitutive parameters in the chapter 4 were considered. The sheet blank elastoplastic behavior is described by the Hill'48, Yld'91 and CPB06 yield criteria, combined with an isotropic hardening defined by the Swift+Voce constitutive model. An associated flow rule (AFR) was assumed for the three yield criteria, as well as a non-associated flow rule (NAFR) applied only to Hill'48 criterion. All constitutive models were implemented in a user material subroutine (Abaqus code - VUMAT).

Taking into consideration, the limiting drawing ratio obtained from this test (2.15, 2.08 and 2.09 for DP500, DP600 and DP780, respectively), in the numerical analysis, an initial blank diameter of 125 mm was used for the three AHSS materials.

5.1.1 Punch force evolution with displacement

Figure 5.2 shows the punch force evolution with the displacement comparison between the experimental data and the results obtained from numerical simulation using the three yield criteria and the NAFR approach.

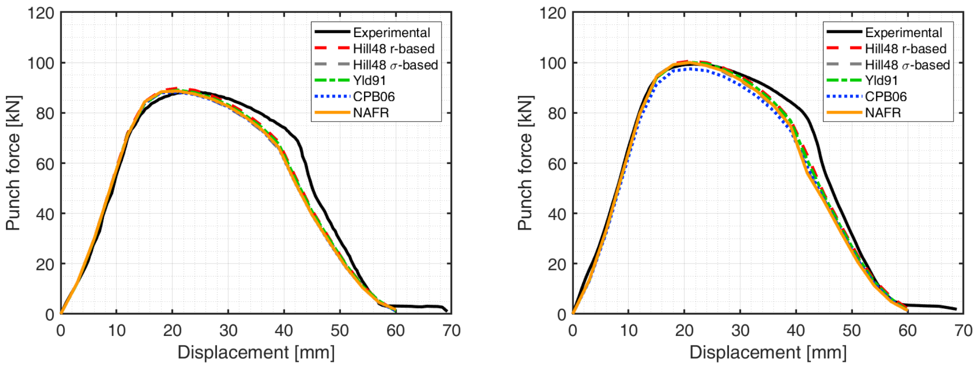

(a) DP500 (b) DP600

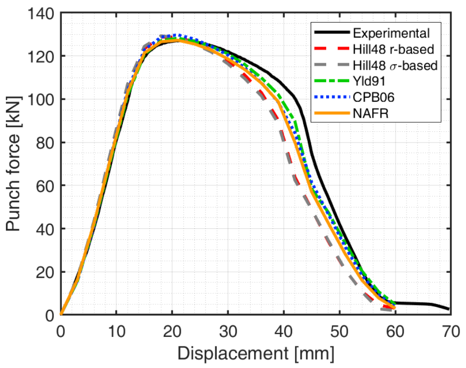

(c) DP780

Figure 5.2: Punch force evolution with punch displacement using the considered yield criteria.

It can be observed that the experimental punch force evolution is quite well predicted by the numerical simulation for the three dual-phase steels, for every yield criterion. These results show that selected hardening law follows an appropriate description of material behavior. Although taking into consideration the influence of friction coefficient value, the attained maximum punch in numerical simulation for the DP500 material is similar to the experimental evidence.

As mentioned in [117, 118], the predicted punch force evolution is very sensitive to the friction conditions, which can increase or decrease the maximum punch force, as well as, the initial slope of the evolution punch force. One the other hand, the punch force evolution is not very sensitive to the selected yield criteria under this drawing operation and proposed materials.

5.1.2 Earing profiles

The earing height profiles of the cylindrical cups were evaluated for the three dual-phase steels using the selected yield criteria. The obtained predictions were compared with experimental 360^{o} measured points, taking as reference the flat bottom of the cup. Figures 5.3, 5.4 and 5.5 present the obtained height of cup ears from the numerical simulation for DP500, DP600 and DP780, respectively.

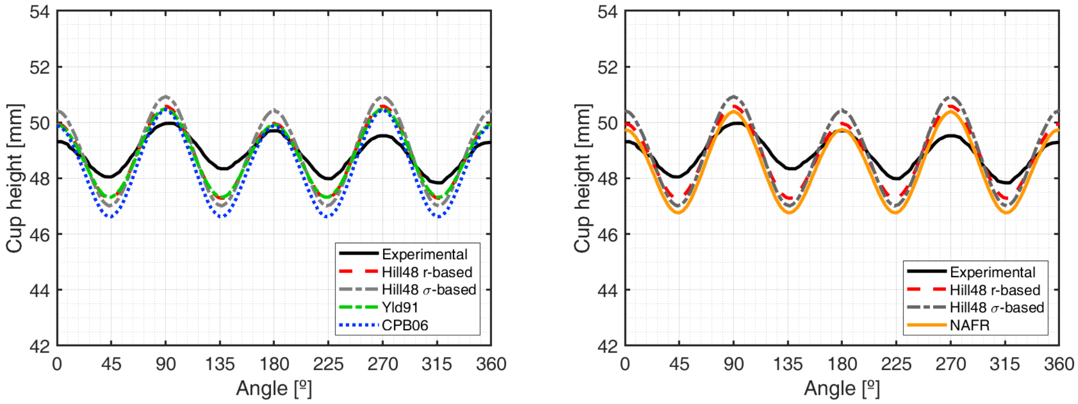

(a) Hill’48, Yld91 and CPB06 AFR approaches (b) AFR and NAFR using Hill’48 function

Figure 5.3: Comparison of numerical earing height profiles of DP500 with experimental data for the different implemented yield criteria.

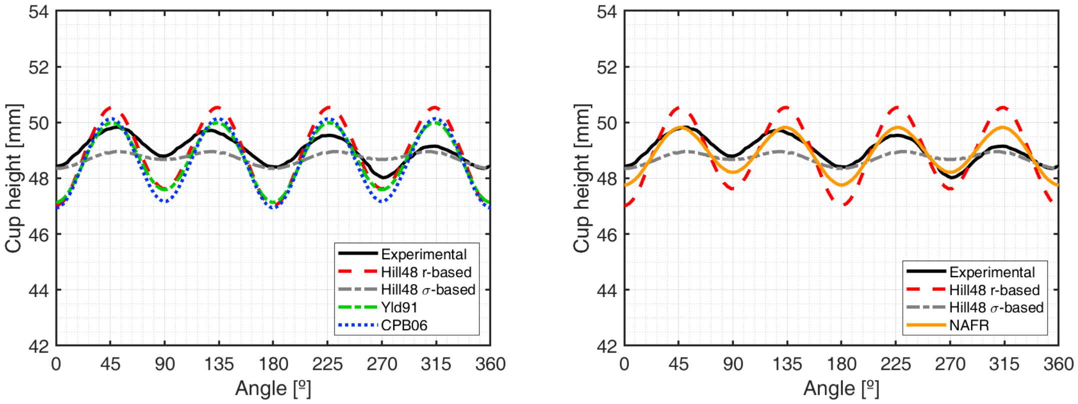

(a) Hill'48, Yld91 and CPB06 AFR approaches (b) AFR and NAFR using Hill'48 function

Figure 5.4: Comparison of numerical earing height profiles of DP600 with experimental data for the different implemented yield criteria.

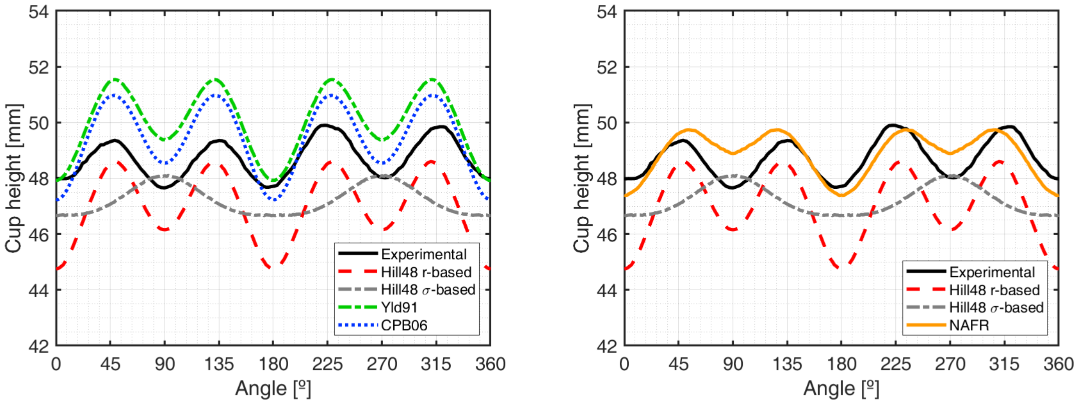

(a) Hill'48, Yld91 and CPB06 AFR approaches (b) AFR and NAFR using Hill'48 function

Figure 5.5: Comparison of numerical earing height profiles of DP780 with experimental data for the different implemented yield criteria.

As expected, all the considered yield criteria, as well as the NAFR approach based on Hill'48 function, give the same number of ears when compared to the experimental evidence, with the exception of Hill'48 σ-based for the DP780, in which only 2 ears where predicted.

In the case of DP500 earing profile predictions, the numerical tendency of earing height evolution from 0^o to 90^o relative to the rolling direction is identical to the experimental behavior, having a higher ear height at 90^o and a valley at 45^o. However, the difference between maximum and minimum ear height values is higher for all considered yield criteria, although the non-associated flow rule (NAFR) is closer to the experimental data than the others predictions.

An opposite behavior is observed for DP600, in which the earing profile evolution shows valleys at 0^o and 90^o and peaks at 45^o. Here, the most significant difference also observed is the amplitude predicted by the numerical simulation based on the associated flow rule, which is higher than the one obtained experimentally, apart from the case of Hill'48 σ-based, which predicts almost an isotropic behavior (amplitude between the maximum and minimum height very low). On the other hand, the prediction given by a non-associated flow rule provides a tendency closer to the experimental points, especially at 45^o, in comparison with the other approaches and yield criteria.

Since the DP780 and DP600 have the same behavior regarding the anisotropic plastic coefficients, the obtained results by the numerical simulation are also similar. The amplitude between the extreme values remains the main difference for the proposed yield criteria. Once again, NAFR predicts an earing height profile closer to the experimental evidence when compared to the other numerical results, however, for 90^o the numerical prediction overestimates the ear height.

Overall, the approach based on a non-associated flow rule provides a closer evolution to the experimental data, however, for some angles the accuracy of obtained results can still be improved. Nevertheless, the variability and dispersion that outcome from the experimental tests must be taken into account, not only in the measurement of earing height profiles, but also the properties used in the constitutive model parameters identification procedure. It is visible that the experimental evolution of the cup height is not symmetrical concerning the orthotropic planes, which implies a greater distance or approximation by the numerical predictions. This phenomenon can be affected by different factors, such as the initial blank centring (despite the existence of a device that minimizes such effect) or even the variation of the initial blank thickness.

5.1.3 Thickness Distribution

In this section, a comparison of the experimental data and numerical thickness distribution along the cup wall for different heights (figure 3.46) is presented, for the final stage of the deep drawing process. The corresponding line for measurement follows the material rolling, diagonal and transverse directions. A relationship between the cup height and sheet thickness was considered in such analysis, being the wall thickness measured perpendicularly to the cup axis.

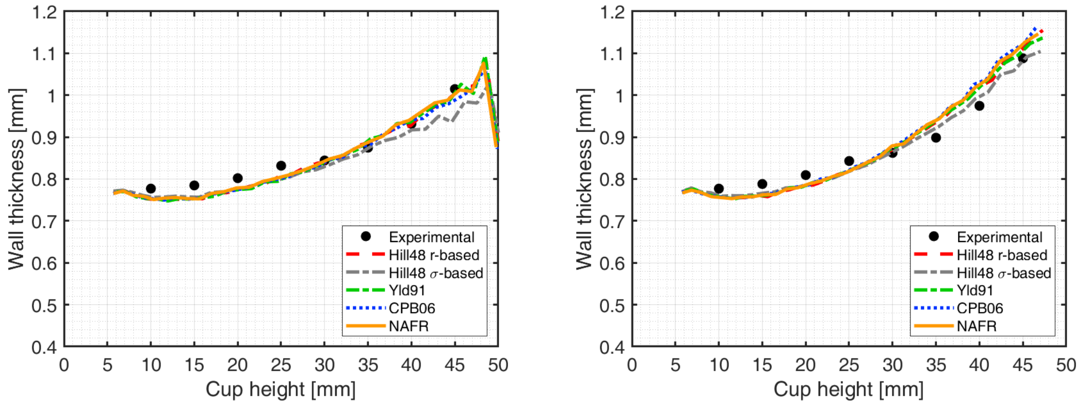

(a) Rolling direction (RD)   (b) Diagonal direction (DD)

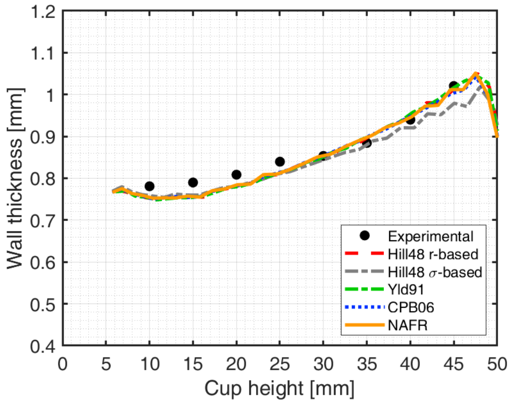

(c) Tranverse direction (TD)

Figure 5.6: Thickness distribution along vertical wall of DP500 using different yield criteria.

As seen in figure 5.6, the overall tendency of the wall thickness is similar for all the proposed yield criteria and quite well reproduced when compared to the experimental data points. Along the vertical cup wall, the thickness values are typically higher than the initial thickness, as a consequence of the compression stress state in the circumferential direction.

As expected, for the diagonal direction (45^{o} to RD) the increase of the cup wall thickness is higher, since for this direction the anisotropic plastic coefficient is greater than the other values.

For this material, only the Hill'48 r-based yield criterion gives a different behavior, underestimating the increase of the cup wall thickness along the rolling and transverse direction, but giving a closer distribution for the diagonal direction. Again, it should be noted that the differences between the numerical and experimental results are very low and at the same level of the variations observed experimentally (figure 3.47).

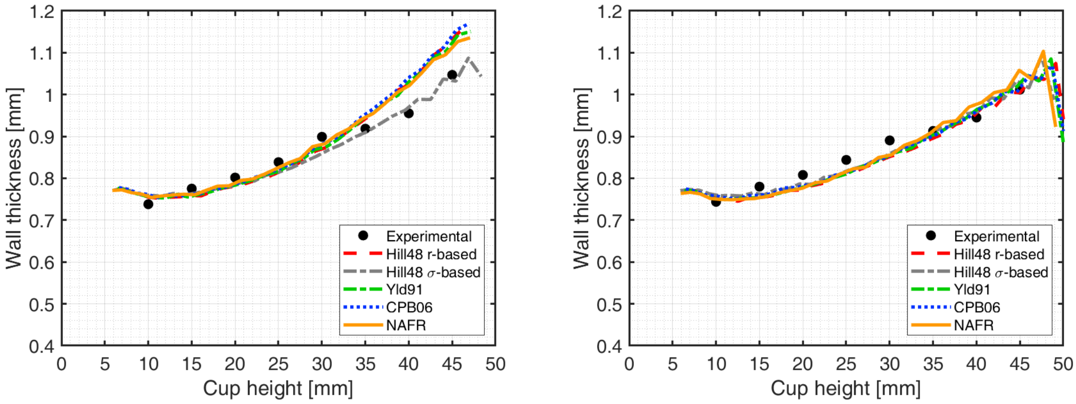

(a) Rolling direction (RD)

(b) Diagonal direction (DD)

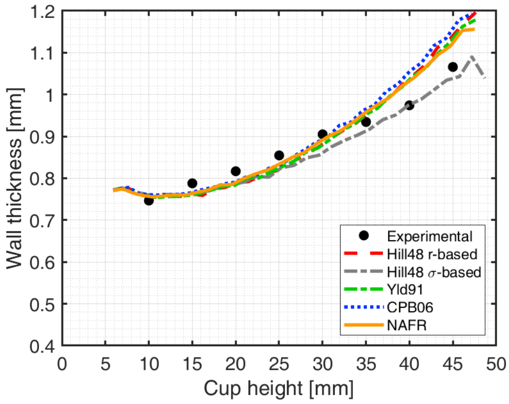

(c) Tranverse direction (TD)

Figure 5.7: Thickness distribution along vertical wall of DP600 using different yield criteria.

In case of DP600 wall thickness numerical predictions (figure 5.7), there is a clear overestimation of the thickness increase after the 30 mm for the rolling and transverse directions using the proposed yield criteria, except the Hill’48 r-based which predicts an wall thickness evolution almost identical to the experimental tendency.

For the diagonal direction (45^{o}), the overall tendency of the wall thickness is similar for all the proposed yield critera and well described when compared to the experimental data.

Since the DP600 has an opposite anisotropic behavior than the DP500, for the diagonal direction the increase of the cup wall thickness is lower than the other directions, as a consequence of the higher ear cup height.

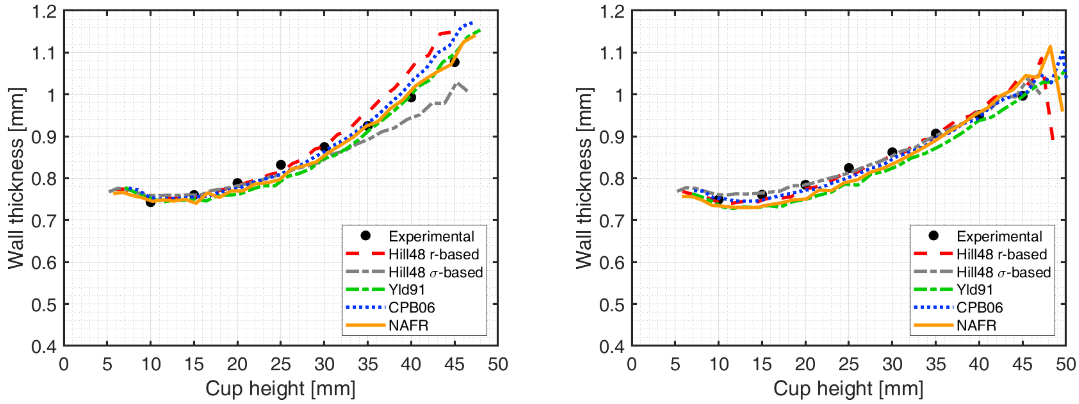

(a) Rolling direction (RD)

(b) Diagonal direction (DD)

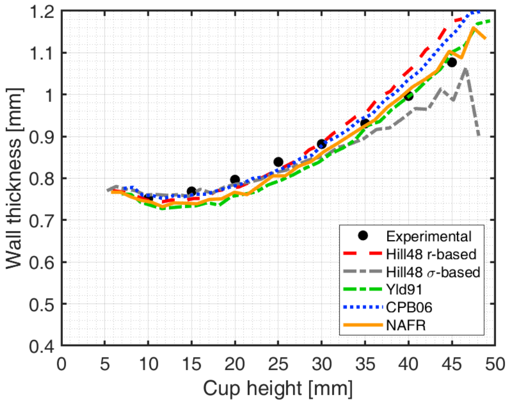

(c) Tranverse direction (TD)

Figure 5.8: Thickness distribution along vertical wall of DP780 using different yield criteria.

Figure 5.8 presents the cup thickness distribution along the vertical wall for DP780 using the different yield criteria. As seen, all the constitutive models show a good agreement with experimental points for the diagonal direction. However, for the rolling direction and for the transverse direction, some differences between the numerical predictions are visible. The Hill'48 r-based underestimates the thickness increase and the Hill'48 σ-based overestimates the thickness after the 30 mm.

For this material, The obtained cup thickness distributions using the Yld91 yield criteria and the NAFR approach based on Hill'48 function show a good correlation with the measured experimental data for all the considered sheet directions, for the final stage of the deep drawing process.

Figures 5.9, 5.10 and 5.11 show the distribution of the equivalent plastic strain and also the distribution of equivalent stress for each considered yield criteria for the DP500, DP600 and DP780, respectively.

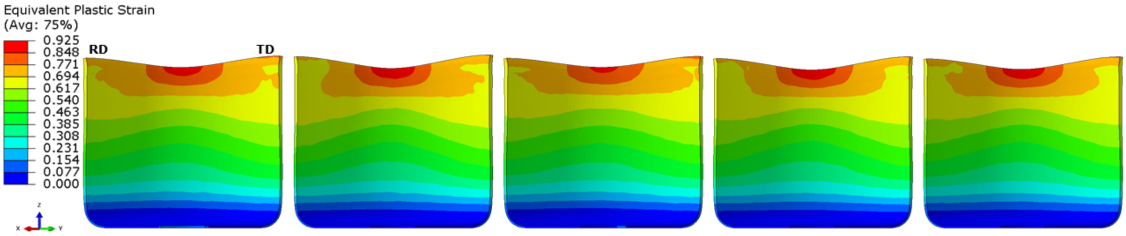

(a) Equivalent plastic strain

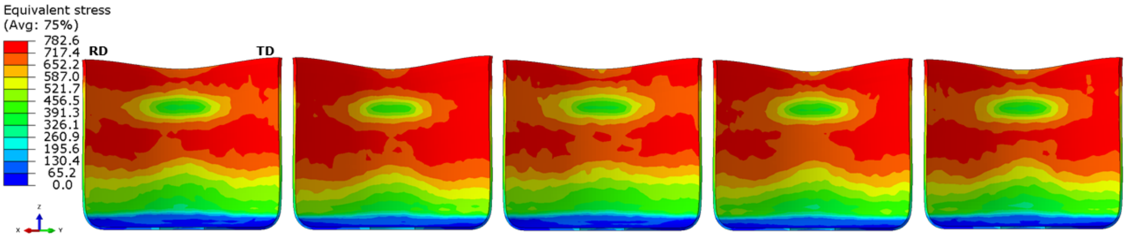

(b) Equivalent stress

Figure 5.9: Equivalent plastic strain and equivalent stress contours for DP500 cylindrical cup using the different yield criteria: Hill'48 r-based, Hill'48 σ-based, Yld91, CPB06, NAFR, from left to right, respectively.

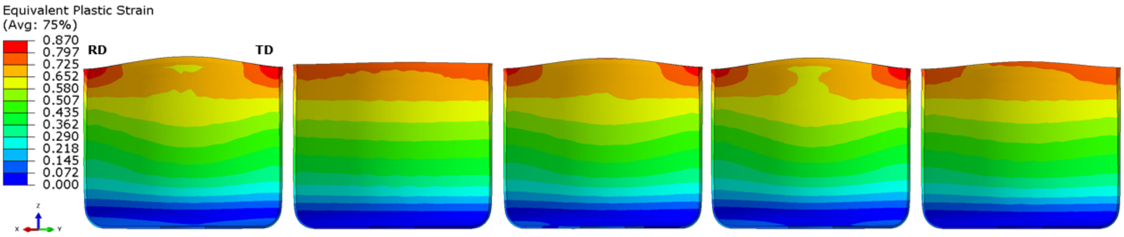

(a) Equivalent plastic strain

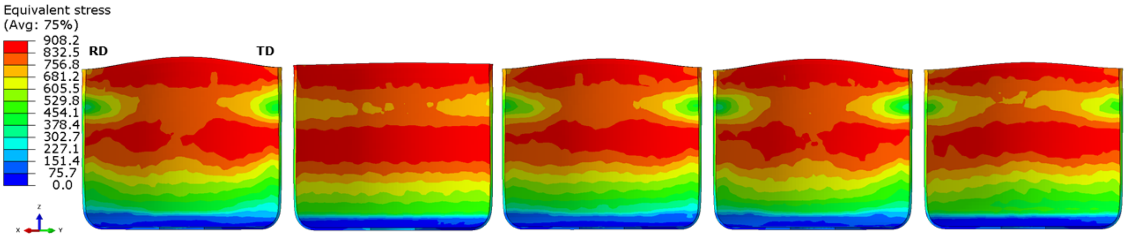

(b) Equivalent stress

Figure 5.10: Equivalent plastic strain and equivalent stress contours for DP600 cylindrical cup using the different yield criteria: Hill'48 r-based, Hill'48 σ-based, Yld91, CPB06, NAFR, from left to right, respectively.

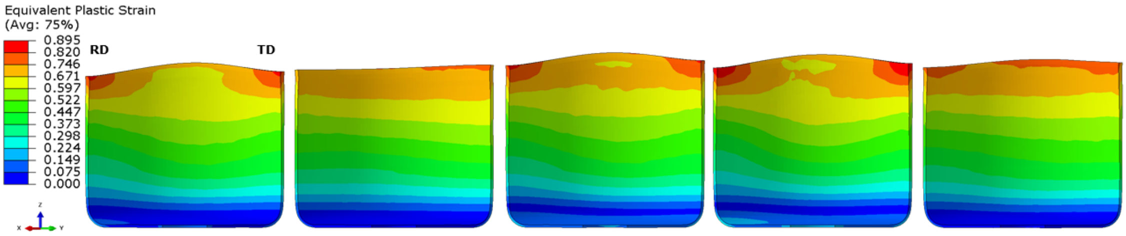

(a) Equivalent plastic strain

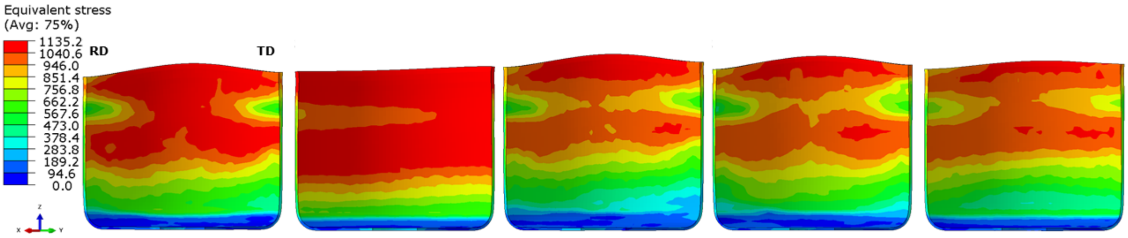

(b) Equivalent stress

Figure 5.11: Equivalent plastic strain and equivalent stress contours for DP780 cylindrical cup using the different yield criteria: Hill’48 r-based, Hill’48 σ-based, Yld91, CPB06, NAFR, from left to right, respectively.

It is observed that the strain distribution presents an opposite behavior when compared to the earing height profile. In the zone near to the cylindrical cup border, the equivalent plastic strain presents higher values, as a result of the ironing caused by the blank holder.

5.2 Nakajima test

To evaluate and validate the ability to predict damage and formability limits using the previous defined damage models, a finite element analysis is carried out considering the Nakajima test and the obtained results are compared with experimental data.

Numerical simulations were performed using a 3D finite element explicit analysis with Abaqus/Explicit code and defining a full model for the Nakajima test (figure 5.12(a)).

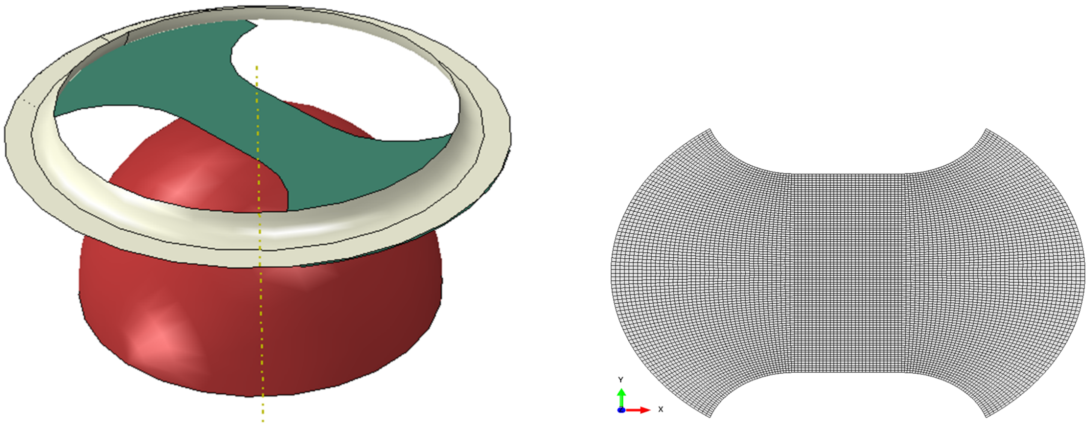

(a) (b)

Figure 5.12: Nakajima test finite element 3D model: a) setup and position of tools and blank; b) blank mesh in XY plane (1x1 mm element in center).

The sheet blank was discretized by three layers of eight node deformable elements with reduced integration (C3D8R type from Abaqus Library), being the tools (die, punch and blank holder) modeled by analytical rigid surfaces. The spacial discretization of blank XY plane can be seen in figure 5.1(b). A constant Coulomb friction coefficient of 0.05 was defined for the interacting surfaces. Regarding the material modeling, the identified constitutive parameters in the previous sections were considered. The sheet blank elastoplastic behavior is described by the Swift+Voce hardening law.

For the Johnson-Cook (JC) and Hosford-Coulomb (HC) damage models the anisotropic Hill'48 r-based yield criterion was considered. Johnson-Cook and GTN ductile damage models are available in FE program, on the other hand, the HC model was implemented in a user material subroutine.

5.2.1 Forming limits and punch force evolution

Limit strain values from the numerical simulation were obtained using the same experimental methodology. Each ductile damage model FLC was formed by a fitted curve to the strains points acquired from different sample widths (as seen in figure 3.33) using the least-squares method. The comparison of DP780 forming limit curves, determined experimentally and using the ductile damage models is shown in figure 5.13.

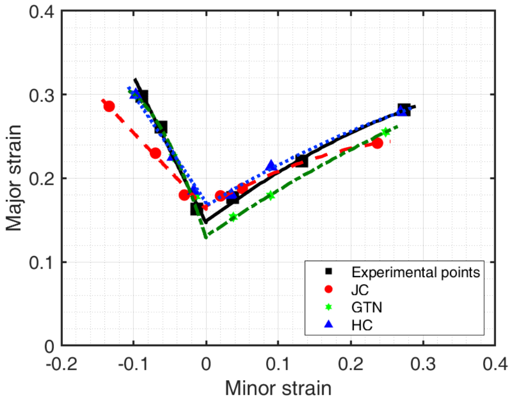

Figure 5.13: Comparison between the experimental points and numerical forming limit curves using the different damage models for the dual-phase steels.

Globally, the forming limit curves obtained from numerical simulation using the damage models and presented in figure 5.13 show a similar tendency compared to the experimental data. The GTN and Hosford-Coulomb criteria predictions of forming limit curve give a closer result to the experimental data for the drawing zone, while in case of Johnson-Cook damage model, the numerical points are more dispersed. Also, this damage model seems to have a higher formability in plane strain state and a lower limit in the stretching region, being more evident in equibiaxial loading case.

By comparison, the formability prediction for DP780 using these three ductile damage models with experimental results, it can be concluded that the Hosford-Coulomb damage model gives a better approximation and shows a closer overall prediction to current experimental data. However, with a smaller initial relative density, the formability prediction of GTN can be increased and the FLC could be closer in plane strain and stretching region (right side of FLD) but a possible overestimation in drawing region (left side of FLD) could be happen.

Additionally, a comparison of punch force vs. displacement curves were performed, in order to evaluate the numerical and experimental data, being also a complement to the FLD analysis.

Figure 5.14 shows the curves of punch force vs. displacement evolution during deformation for each selected sample width or strain path, defined in this work. Numerical results for current damage models and experimental data are compared on the same graph.

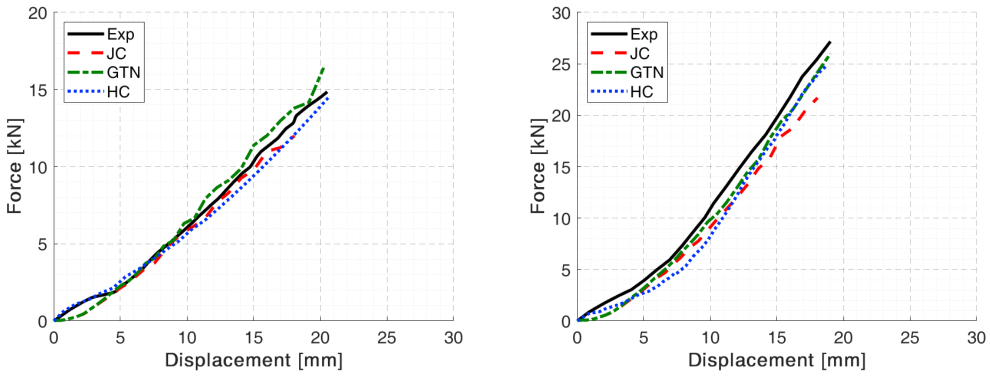

(a) width = 25 mm (b) width = 50 mm

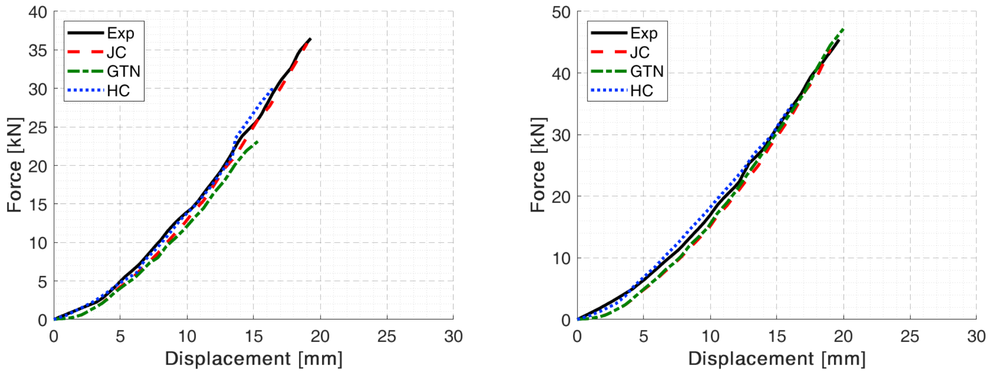

(c) width = 75 mm (d) width = 100 mm

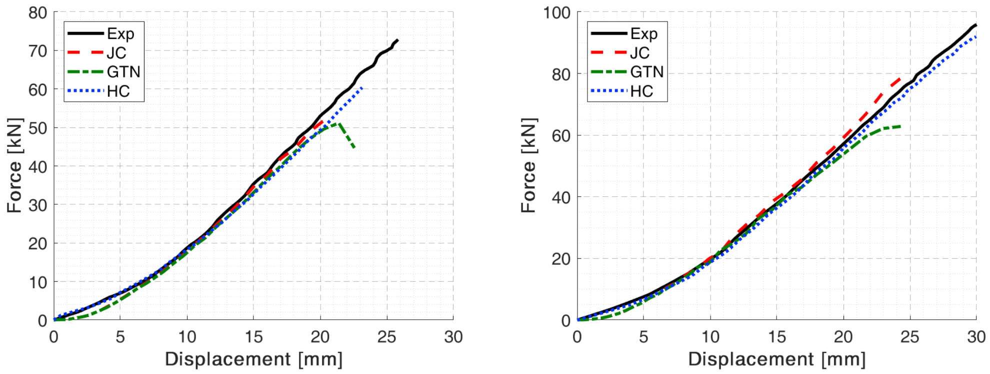

(e) width = 125 mm (f) width = 175 mm

Figure 5.14: Comparison of experimental punch force evolution for different specimen widths, with the numerical results from the damage models.

From figure 5.14, it can be observed that the evolution of punch force predicted is very similar to the experimental punch force. Additionally, this comparison allows the evaluation of punch stroke at which fracture occurs.

Since GTN damage model has a closer forming limit curve to the experimental data in the drawing zone, like the Hosford-Coulomb prediction, the punch stroke is in a very good agreement with experimental observation. In contrast, the Johnson-Cook model shows a smaller value of punch stroke for all of defined sample widths, except for the plane strain case.

Figure 5.15 shows a comparison between the experimental samples and the Hosford-Coulomb damage model fracture predictions. The obtained numerical results present a good agreement with experimental evidence, validating the ability of this type of constitutive models to predict the region where the material will fail.

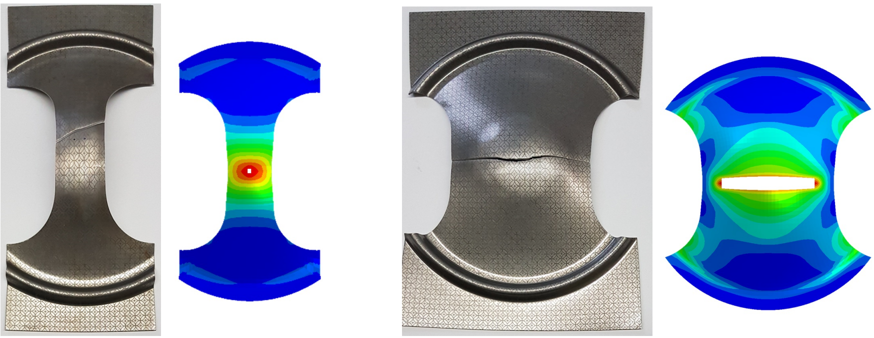

(a) width = 25 mm

(b) width = 75 mm

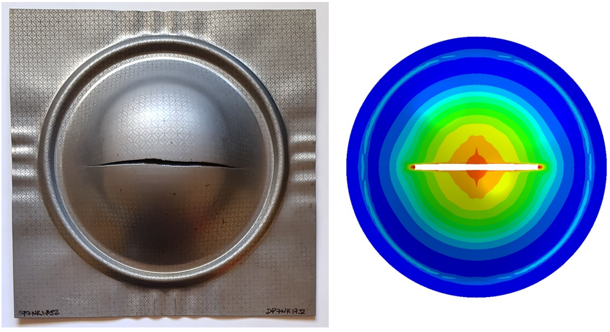

(c) width = 175 mm

Figure 5.15: Comparison of experimental fracture location with the numerical results from the Hosford-Coulomb damage models.

5.3 Cross-Die test

The applicability of the proposed damage models is illustrated by means of a deep drawing Cross-Die failure case of a cross-shaped (figure 5.16(b)) sheet metal component. This type of test was selected since it has a similar loading condition to those observed in the industry. To compare the performance of the different ductile damage models for the fracture prediction of such component, a finite element analysis is performed considering the Cross-Die test. The process is comparable to the deep drawing cylindrical cup (Swift) test, but different on the resulting final geometry.

Numerical simulations were performed using a 3D finite element explicit analysis with Abaqus/Explicit code and defining only one quarter of the real experimental setup (figure 5.17).

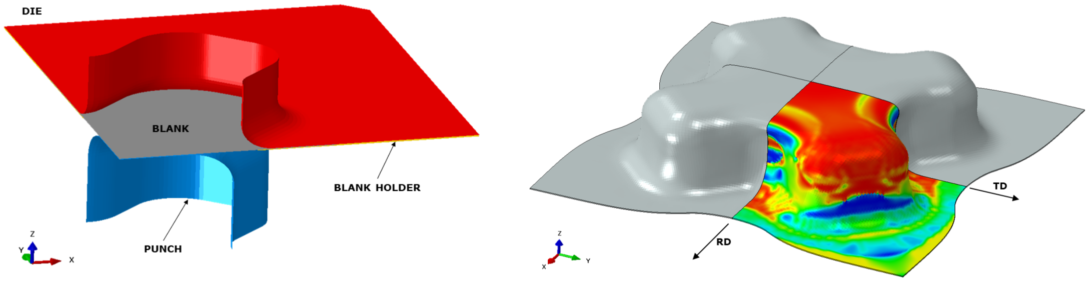

(a) (b)

Figure 5.16: 3D finite element model for Cross-Die test: a) setup and position of tools and blank; b) blank symmetry.

The sheet blank was discretized by three layers of eight node deformable elements with reduced integration (C3D8R type from Abaqus Library), making a total of 15138 elements, being the tools (die, punch and blank holder) modeled by discretized rigid surfaces. The spacial discretization of blank XY plane can be seen in figure 5.17(a), while the punch and die meshes are shown in figures 5.17(b) and 5.17(c), respectively.

The blank size is 270x270 mm square and a 60 mm punch stroke was considered, which corresponds to the height of a successful obtained part. The punch and die radii have constant values of 20 mm and 14 mm respectively, having the punch a total width of 180 mm and the die an opening of 186 mm. A constant blank holder force of 200 kN was applied for DP5000 and 300 kN in the case of DP780 steels.

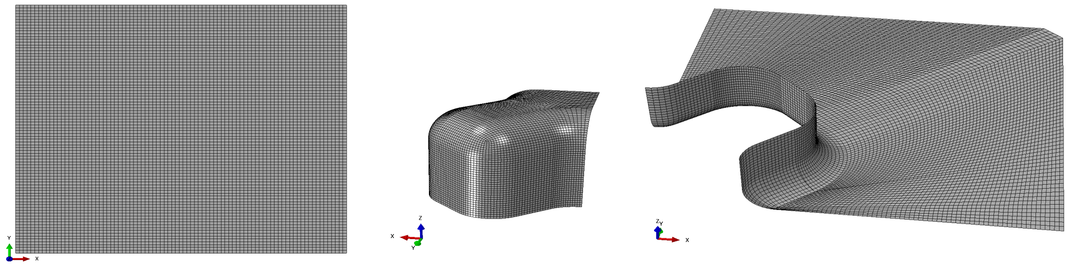

(a) Blank (b) Punch (c) Die

Figure 5.17: Finite element discretization of tools and blank used in the Cross-Die numerical analysis.

A constant Coulomb friction coefficient of 0.05 was defined for the interacting surfaces. Regarding the material modeling, the identified constitutive parameters in the previous chapter 4 were considered. The sheet blank elastoplastic behavior is described by the Swift+Voce hardening law. For the Johnson-Cook and Hosford-Coulomb damage models the anisotropic Hill'48 r-based yield criterion was considered. Johnson-Cook and GTN ductile damage models are available in FE program, on the other hand, the HC model was implemented in a user material subroutine.

5.3.1 Fracture location and equivalent plastic strain distribution

Figure 5.18 shows the predicted numerical results and the corresponding fracture location, as well as, the equivalent plastic strain and triaxiality level contours to the moment before fracture for the dual-phase steel DP500.

For this type of loading condition and material, the three models predict different zones where the material will fail, as shown in figure 5.18(a). The GTN damage model predict possible fracture location that can be observed in numerical results using the Johnson-Cook damage model and the Hosford-Coulomb damage model.

However, all the fractures were predicted for areas where the triaxiality levels are high, between a plane strain state and an equibiaxial stress state. The maximum attained value of the equivalent plastic strain is related with fracture location, with the exception of Johnson-Cook damage model, which predicts a different zone (near punch head radius).

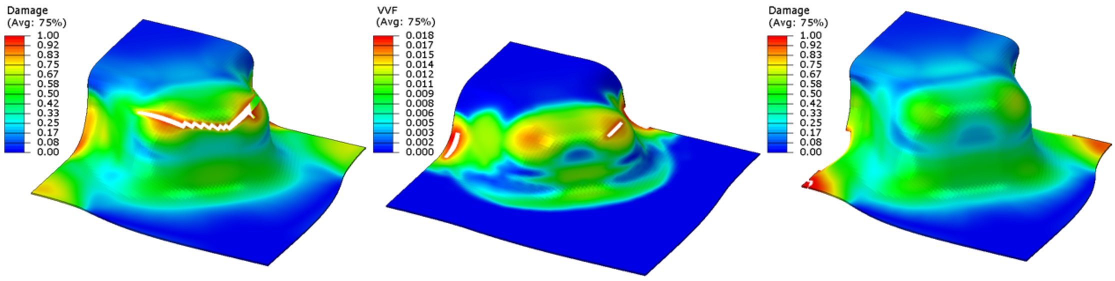

(a) Damage variable and volume void fraction

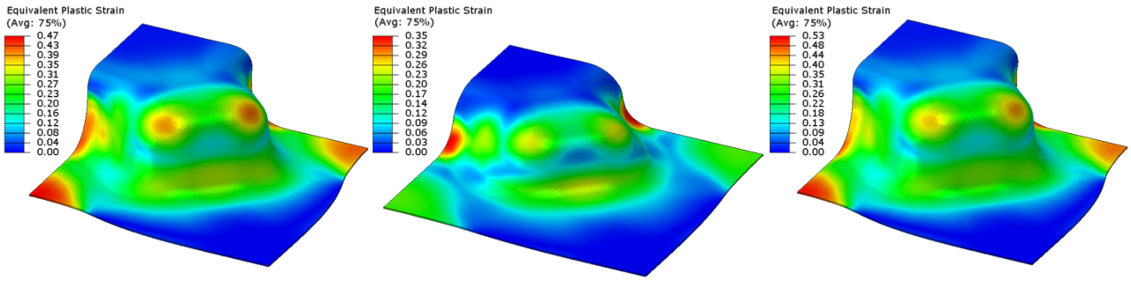

(b) Equivalent plastic strain

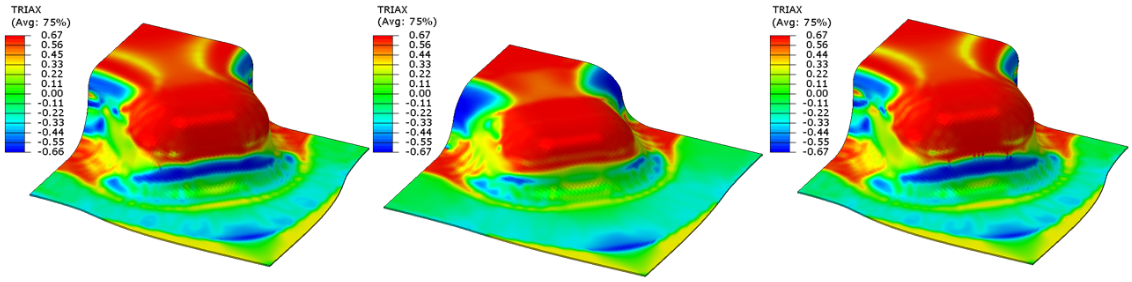

(c) Triaxiality

Figure 5.18: Comparison of the predicted fracture location using the different damage models and corresponding contours for DP500: Johnson-Cook, GTN and Hosford-Coulomb, from left to right, respectively.

Additionally, the GTN damage model overestimate the development of damage, predicting the fracture initiation for lower values of equivalent plastic strain and a consequent lower component height. Regarding the triaxiality contours, the obtained results from the three damage models show a similar behavior, as expected, since the geometry and loading conditions are the same.

The same methodology was applied to analyze the obtained numerical results for DP780. Figure 5.19 show the predicted numerical results and the corresponding fracture location, as well as, the equivalent plastic strain and triaxiality level contours just before fracture.

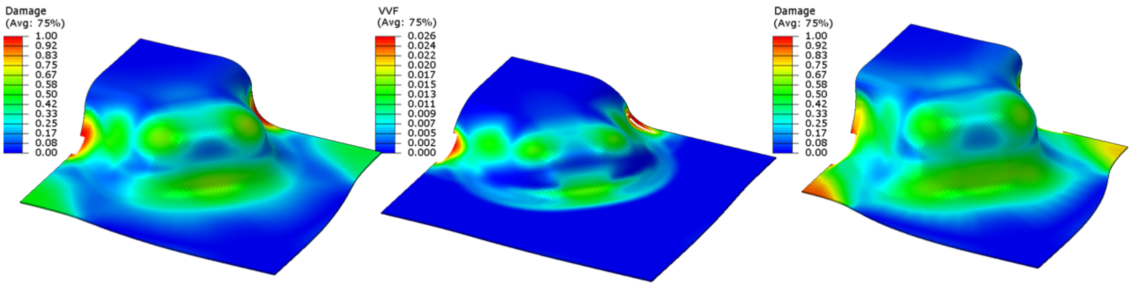

(a) Damage variable and volume void fraction

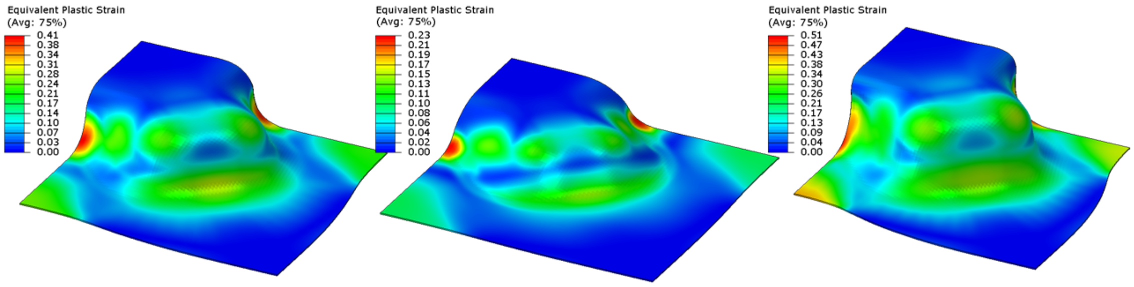

(b) Equivalent plastic strain

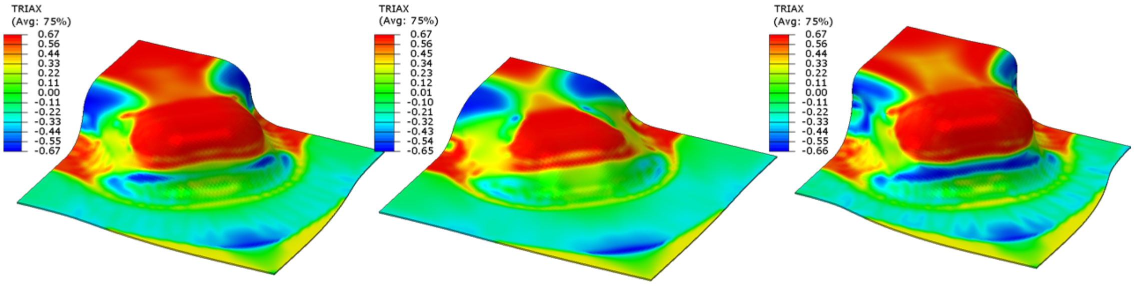

(c) Triaxiality

Figure 5.19: Comparison of the predicted fracture location using the different damage models and corresponding contours for DP780: Johnson-Cook, GTN and Hosford-Coulomb, from left to right, respectively.

As seen in figure 5.19, the three models predict the occurrence of fracture for DP780 in the same local of the component. The fracture location is characterized by higher levels of triaxiality, near to the plane strain levels, where the ability to plastic deform the material is more limited. Another aspect that can be observed is the premature fracture prediction and consequently a lower height of the component by the GTN damage model in comparison with the other two damage models. This fact is confirmed by the lower value of the equivalent plastic strain present in the part at moment before the fracture, which it is also an indicator of a possible location.

5.3.2 Evolution of punch force with displacement

The punch force vs. punch displacement evolution was also analyzed and figure 5.20 presents the obtained numerical predictions for DP500 and DP780. Additionally, it was considered, as a reference, a punch vs. displacement curve without using damage models.

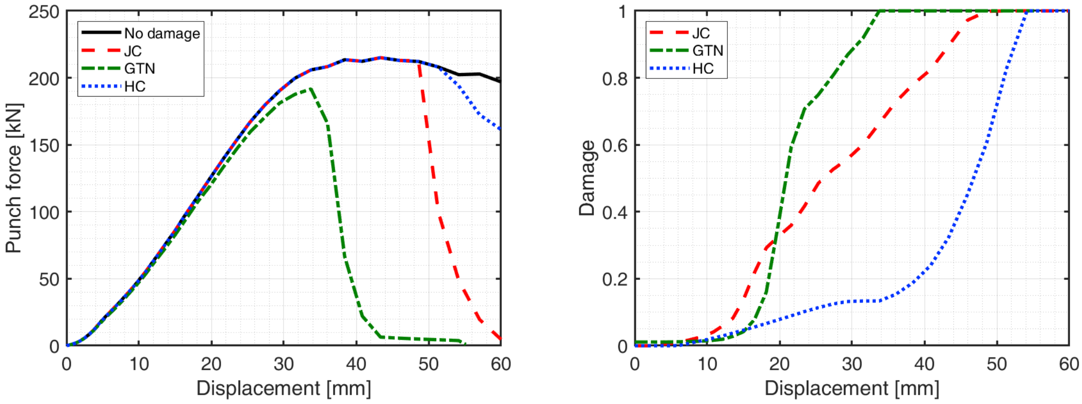

(a) DP500

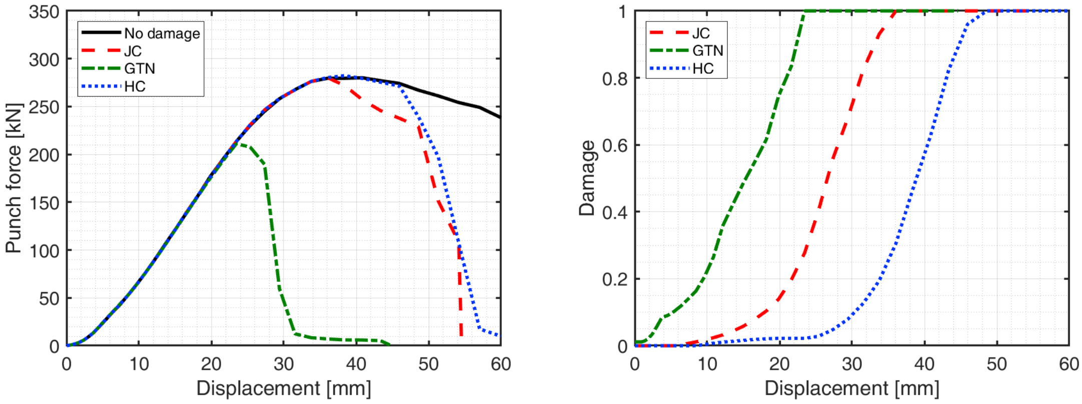

(b) DP780

Figure 5.20: Punch force evolution with punch displacement using the considered yield criteria.

For the two selected dual-phase steels, the numerical predictions of punch displacement at failure are different. GTN damage model predicts fracture at lower punch displacement and consequently a lower punch force for both materials (34 mm for DP500 and 25 mm for DP780), since the volume void fraction variable start to increase its value at an early stage of the drawing process, overestimating the damage development when compared to the other damage models.

Regarding the Johnson-Cook damage model and the Hosford-Coulomb damage model, both predict closer punch displacement at fracture (49 mm and 53 mm for DP500, and

36 mm and 48 mm for DP780, respectively), and also an identical punch force evolution tendency, until the internal damage variable of Jonhson-Cook reaches the critical value and a consequent material failure. In all of the numerical simulations performed using the Hosford-Coulomb model, the fracture occurs after the maximum force peak.

The difference observed in the numerical results, specially when using the GTN damage models, can be attributed to the parameter identification procedure, which in turn is related with triaxiality values. The tests used for Johnson-Cook and Hosford-Coulomb parameter identification are for a wide range of triaxiality stress states, from low triaxility (shear test) to high triaxiality (bulge test), considering also the tensile test result and the plane strain data. In case of GTN, the tests used have higher triaxiality values (tensile+bulge). Since the component shows critical strain localization for for plane strain triaxiality levels, this means that GTN and corresponding damage parameters, which may have different solutions, are not adjusted to predict failure in this component, although experimental tests should be performed to validate such results.

Chapter 6

Conclusions

This chapter highlights the main conclusions from this research, as well as, some considerations for future work concerning the modeling of the material behavior and its usage in the numerical simulation of sheet metal forming processes.

(This page was deliberately left blank)

6.1 Final remarks

The use of numerical tools is currently part of the development stage of products in sheet metal forming industries, and one of the main objectives of numerical simulation is to predict, with acceptable precision, the material behavior, as well as, the occurrence of defects in the obtained parts by providing alternative solutions to overcome problems. However, the increasing complexity in geometries and the use of new materials and corresponding non-traditional behaviors, combined with shorter development times and other factors inherent to the sheet metal forming process, always create new challenges and make numerical simulation an indispensable tool in this manufacturing process. The present thesis made use of the finite element method in the numerical simulation of sheet metal forming processes, where different constitutive models were applied to reproduce the anisotropic and damage behavior of three AHSS.

Within the scope of this thesis, the mechanical behavior of the advanced high strength steels DP500, DP600 and DP780 has been investigated under various loading conditions. Accordingly, uniaxial tensile tests, uniaxial and disc compression, and also hydraulic bulge tests have been performed to cover a wide range of stress states, which are present in complex sheet metal forming parts. The obtained results of the mechanical properties and stress-strain flow curves revealed that the loading condition significantly influences the plastic response of the material in terms of strain level, being evident for the bulge test. Additionally, the results of the uniaxial tensile tests performed at different strain rates showed that the amount of heat generated by plastic deformation has an independent trend to the material strength and shows a similar evolution when a normalized engineering strain is considered.

The combination of data from the tensile test with the results from the biaxial bulge test proved to be an approach with excellent results in reproducing the behavior of the material for higher values of plastic strain, since the use of only the stress-strain curve of the uniaxial tensile test to define the constitutive model may lead to deviations between the extrapolation and the actual behavior of the material.

The use of deep drawing cylindrical cup test allowed the determination of the limiting drawing ratio for selected materials, having DP500 steel the higher limit (LDR=2.15), followed by DP780 (LDR=2.09) and DP600 (LDR=2.08). These results show a good correlation with the measured experimental anisotropy coefficients, in which the planar anisotropy is higher for the DP500 steel. Also, the deep drawing cylindrical cup was used to evaluated and validate the performance of different yield criteria to predict the anisotropic behavior of the dual-phase steels. The earing height profile predictions using numerical simulation with a non-associated flow rule (NAFR) showed a good agreement when compared with experimental data points. The ability of the NAFR to predict the yield stress evolution, as well as the plastic anisotropic coefficients independently and simultaneous, proved to be an approach that gives efficient and accurate results.

Three ductile damage models, GTN, Johnson-Cook and Hosford-Coulomb, were described and numerically compared for prediction of damage in sheet metal forming. Finite element analysis of the Nakajima test and a cross-shaped component was performed, using the corresponding identified constitutive model parameters. The numerical simulations of GTN show an overestimation of damage evolution. On the other hand, Johnson-Cook and Hosford-Coulomb predicted identical behaviors and forming limits, although the results obtained from Hosford Coulomb uncoupled damage model are closer to the experimental data. Regarding the fracture location, all of the selected constitutive models provided a similar result.

6.2 Future work

For a deeper knowledge of the investigated topics of research, it would be interesting to continue this work in different paths. With this in mind, several perspectives for future work are proposed:

- The thermomechanical behavior of these dual-phase steels induced by the plastic deformation for different strain rates has not been thoroughly investigated; therefore, uniaxial tensile tests should be performed at higher strain rates ($> 10^{-1}$ s^{-1}) using a digital infrared measurement system, to capture the temperature field in order to analyze and to improve the material modeling;

- Implementation of more advanced constitutive models considering strain rate effects and temperature sensitivity, in order to improve the accuracy of the hardening laws, as well as, the fracture and necking predictions;

- Regarding the material user subroutine VUMAT, different approaches of return mapping within the Abaqus/Explicit FEM code should be considered and its efficiency evaluated (time cost and accuracy of results);

- Cyclic loading tests between a tensile and compression stress state should be performed at different strain levels, to evaluate the stress differential and any Bauschinger effect;

- Application of current developments of experimental systems and numerical methodologies to different materials, such as other type of AHSS and UHSS, aluminum alloys, metallic materials from additive-manufacturing, hybrid metallic materials, etc;
- To develop an integrated methodology for identification of constitutive models and corresponding parameters; it should include a minimum of manual involvement by using identification methodologies based on optimization algorithms and artificial intelligence, namely machine learning.

(This page was deliberately left blank)

References

[1] V.L Hattalli and S.R. Srivatsa. Sheet Metal Forming Processes - Recent Technological Advances. *Materials Today: Proceedings*, 5(1):2564–2574, 2018.

[2] POSCO. *Automotive Steel, Digital Brochure*, 2014 (accessed February 3, 2019). Digital Brochure: http://product.posco.com/homepage/product/eng/jsp/support/s91c5000200b.jsp.

[3] T. P. Hovorun, , K. V. Berladir, V. I. Pererva, S. G. Rudenko, A. I. Martynov, , , and and. Modern materials for automotive industry. *Journal of Engineering Sciences*, 4(2):f8–f18, 2017.

[4] M. Ghosh, A. Ghosh, and A. Roy. Renewable and Sustainable Materials in Automotive Industry. In *Encyclopedia of Renewable and Sustainable Materials*, pages 162–179. Elsevier, 2019.

[5] T.B. Hilditch, T. de Souza, and P.D. Hodgson. Properties and automotive applications of advanced high-strength steels (AHSS). In *Welding and Joining of Advanced High Strength Steels (AHSS)*, pages 9–28. Elsevier, 2015.

[6] A. Ramazani, M. Abbasi, U. Prahl, and W. Bleck. Failure analysis of DP600 steel during the cross-die test. *Computational Materials Science*, 64:101–105, 2012.

[7] H. Kim, T. Altan, and Q. Yan. Evaluation of stamping lubricants in forming advanced high strength steels (AHSS) using deep drawing and ironing tests. *Journal of Materials Processing Technology*, 209(8):4122–4133, 2009.

[8] R.H. Wagoner, J.H. Kim, and J.H. Sung. Formability of Advanced High Strength Steels. *International Journal of Material Forming*, 2(S1):359–362, 2009.

[9] S. Panich, K. Chongbunwatana, and M. Kamonrattanapisud. Formability prediction of advanced high-strength steel sheets by means of combined experimental and numerical approaches. *Procedia Manufacturing*, 29:528–535, 2019.

[10] A.K. Ghosh and S.S. Hecker. Stretching limits in sheet metals: In-plane versus out-of-plane deformation. *Metallurgical Transactions*, 5(10):2161–2164, 1974.

[11] D. Kitting, A. Ofenheimer, A.H. van den Boogaard, and P. Dietmaier. Deformation Scenarios of Combined Stretching and Bending in Complex Shaped Deep Drawing Parts. *Key Engineering Materials*, 554-557:1252–1264, 2013.

[12] J.H. Sung, J.H. Kim, and R.H. Wagoner. A plastic constitutive equation incorporating strain, strain-rate, and temperature. *International Journal of Plasticity*, 26(12):1746–1771, 2010.

[13] Z. Gronostajski, A. Niechajowicz, R. Kuziak, J. Krawczyk, and S. Polak. The effect of the strain rate on the stress- strain curve and microstructure of AHSS. *Journal of Materials Processing Technology*, 242:246–259, 2017.

[14] M.C. Oliveira and J.V. Fernandes. Modelling and Simulation of Sheet Metal Forming Processes. *Metals*, 9(12):1356, 2019.

[15] Z. Yue, K. Cao, H. Badreddine, K. Saanouni, and J. Gao. Failure prediction on steel sheet under different loading paths based on fully coupled ductile damage model. *International Journal of Mechanical Sciences*, 153-154:1–9, 2019.

[16] W. Volk, P. Groche, A. Brosius, A. Ghiotti, B.L. Kinsey, M. Liewald, L. Madej, J. Min, and J. Yanagimoto. Models and modelling for process limits in metal forming. *CIRP Annals*, 68(2):775–798, 2019.

[17] F. Barlat. Constitutive Modeling for Sheet Metal Forming. In *AIP Conference Proceedings*, volume 778, pages 353–358, 2005.

[18] P. Hora, P. Peters, N. Manopulo, and M. Gorji. Challenges in the accurate modelling of sheet metal forming processes. *Forming Technology Forum*, pages 3–9, 2005.

[19] H. Yang, H. Li, J. Ma, Z. Zhang, and J. Chen. Constitutive modeling related uncertainties: Effects on deformation prediction accuracy of sheet metallic materials. *International Journal of Mechanical Sciences*, 157–158:574–598, 2019.

[20] A. Taherizadeh, D.E. Green, and J.W. Yoon. A non-associated plasticity model with anisotropic and nonlinear kinematic hardening for simulation of sheet metal forming. *International Journal of Solids and Structures*, 69-70:370–382, 2015.

[21] M. Brünig, S. Gerke, and M. Schmidt. Damage and failure at negative stress triaxialities: Experiments, modeling and numerical simulations. *International Journal of Plasticity*, 102:70–82, 2018.

[22] Q. Hu, X. Li, and J. Chen. On the calculation of plastic strain by simple method under non-associated flow rule. *European Journal of Mechanics - A/Solids*, 67:45–57, 2018.

[23] M. Watson, R. Dick, Y.H. Huang, A. Lockley, R. Cardoso, and A.D. Santos. Benchmark 1 - Failure Prediction after Cup Drawing, Reverse Redrawing and Expansion Part A: Benchmark Description. *Journal of Physics: Conference Series*, 734:022001, 2016.

[24] F. Barlat. Advanced Constitutive Modeling for Application to Sheet Forming. *Journal of Physics: Conference Series*, 1063:012002, 2018.

[25] G. Mase. *Continuum mechanics for engineers*. CRC Press, Boca Raton, Fla, 1999.

[26] D. Banabic. *Sheet Metal Forming Processes*. Springer Berlin Heidelberg, 2010.

[27] I.N. Vladimirov, M.P. Pietryga, and S. Reese. Anisotropic finite elastoplasticity with nonlinear kinematic and isotropic hardening and application to sheet metal forming. *International Journal of Plasticity*, 26(5):659–687, 2010.

[28] H. Pashazad and M. Kharazi. A peridynamic plastic model based on von Mises criteria with isotropic, kinematic and mixed hardenings under cyclic loading. *International Journal of Mechanical Sciences*, 156:182–204, 2019.

[29] P. Ludwik. *Elemente der Technologischen Mechanik*. VerlagVon Julius, Springer Leipzig, 1909.

[30] J.H. Hollomon. Tensile Deformation. *Transactions of the Metallurgical Society of AIME*, 162:268–290, 1945.

[31] E. Voce. The relationship between stress and strain for homogeneous deformations. *Journal of the Institute of Metals*, 74:537–562, 1948.

[32] H.W. Swift. Plastic instability under plane stress. *Journal of the Mechanics and Physics of Solids*, 1(1):1–18, 1952.

[33] J.E. Hockett and O.D. Sherby. Large strain deformation of polycrystalline metals at low homologous temperatures. *Journal of the Mechanics and Physics of Solids*, 23(2):87–98, 1975.

[34] A.K. Gosh. Tensile instability and necking in materials with strain hardening and strain-rate hardening. *Acta Metallurgica*, 25:1413–1424, 1977.

[35] L. Kessler and J. Gerlach. The impact of materials testing strategies on the determination and calibration of different FEM material models. In *Proceedings of IDDRG 2006*, pages 113–120, 2006.

[36] T.B. Stoughton. A non-associated flow rule for sheetmetal forming. *International Journal of Plasticity*, 18:687–714, 2002.

[37] R. von Mises. Mechanik der festen Körper im plastisch deformablen Zustand. *Nachrichten von der Gesellschaft der Wissenschaften zu Göttingen, Mathematisch-Physikalische Klasse*, 1:582–592, 1913.

[38] H.-É. Tresca. Mémoire sur l'écoulement des corps solides soumis à de fortespressions. *Comptes Rendus l'Académie des Sciences*, 59:754–758, 1864.

[39] A.V. Hershey. The plasticity of an isotropic aggregate of anisotropic face centred cubiccrystals. *Journal of Applied Mechanics*, 21:241—-249, 1954.

[40] F. Barlat, J.C. Brem, J.W. Yoon, K. Chung, R.E. Dick, D.J. Lege, F. Pourboghrat, S.-H. Choi, and E. Chu. Plane stress yield function for aluminum alloy sheets—part 1: theory. *International Journal of Plasticity*, 19(9):1297–1319, 2003.

[41] R. Hill. A theory of the yielding and plastic flow of anisotropic metals. *Proceedings of the Royal Society London A*, 193:281–297, 1948.

[42] F. Barlat and K. Lian. Plastic behavior and stretchability of sheet metals. Part I: A yield function for orthotropic sheets under plane stress conditions. *International Journal of Plasticity*, 5(1):51–66, 1989.

[43] R.W. Logan and W.F. Hosford. Upper-bound anisotropic yield locus calculations assuming <111> pencil glide. *International Journal of Mechanical Sciences*, 22(7):419–430, 1980.

[44] F. Barlat, D.J. Lege, and J.C. Brem. A six-component yield function for anisotropic materials. *International Journal of Plasticity*, 7(7):693–712, 1991.

[45] O. Cazacu, B. Plunkett, and F. Barlat. Orthotropic yield criterion for hexagonal closed packed metals. *International Journal of Plasticity*, 22(7):1171–1194, 2006.

[46] F. Barlat, H. Aretz, J.W. Yoon, M.E. Karabin, J.C. Brem, and R.E. Dick. Linear transfomation-based anisotropic yield functions. *International Journal of Plasticity*, 21(5):1009–1039, 2005.

[47] D. Banabic. An improved analytical description of orthotropy in metallic sheets. *International Journal of Plasticity*, 21(3):493–512, 2005.

[48] H. Vegter and A.H. van den Boogaard. A plane stress yield function for anisotropic sheet material by interpolation of biaxial stress states. *International Journal of Plasticity*, 22(3):557–580, 2006.

[49] T.B. Stoughton and J.W. Yoon. Review of Drucker's postulate and the issue of plastic stability in metal forming. *International Journal of Plasticity*, 22:391–433, 2006.

[50] M. Safaei, J.W. Yoon, and W. De Waele. Study on the definition ofequivalent plastic strain under non-associated flow rule for finiteelement formulation. *International Journal of Plasticity*, 58:219–238, 2014.

[51] J. Mendiguren, L. Galdos, and E. Saenz de Argandoña. On the plastic flow rule formulation in anisotropic yielding aluminium alloys. *The International Journal of Advanced Manufacturing Technology*, 99(1-4):255–274, 2018.

[52] E.H. Atzema. Formability of auto components. In *Automotive Steels*, pages 47–93. Elsevier, 2017.

[53] P. Teixeira, A.D. Santos, J. César de Sá, F.M. Andrade Pires, and A. Barata da Rocha. Sheet metal formability evaluation using continuous Damage Mechanics. *International Journal of Material Forming*, 2:463–466, 2009.

[54] J. Lemaitre. A Continuous Damage Mechanics Model for Ductile Fracture. *Journal of Engineering Materials and Technology*, 107(1):83–89, 1985.

[55] S. Thuillier A. Pradeau and J.W. Yoon. Prediction of failure in bending of an aluminium sheet alloy. *International Journal of Mechanical Sciences*, 19:23–35, 2016.

[56] T.B. Stoughton and J.W. Yoon. A new approach for failure criterion for sheet metals. *International Journal of Plasticity*, 27(3):440–459, 2011.

[57] T.-S. Cao, C. Bobadilla, P. Montmitonnet, and P.-O. Bouchard. A comparative study of three ductile damage approaches for fracture prediction in cold forming processes. *Journal of Materials Processing Technology*, 216:385–404, 2015.

[58] F.H. Aboutalebi, M. Farzin, and M. Mashayekhi. Numerical predictions and experimental validations of ductile damage evolution in sheet metal forming processes. *Acta Mechanica Solida Sinica*, 25(6):638–650, 2012.

[59] A. Watanabe, S. Fujikawa, A. Ikeda, and N. Shiga. Prediction of Ductile Fracture in Cold Forging. *Procedia Engineering*, 81:425–430, 2014.

[60] Y. Bai and T. Wierzbicki. A comparative study of three groups of ductile fracture loci in the 3D space. *Engineering Fracture Mechanics*, 135:147–167, 2015.

[61] T. Wierzbicki, Y. Bao, Y.-W. Lee, and Y. Bai. Calibration and evaluation of seven fracture models. *International Journal of Mechanical Sciences*, 47(4-5):719–743, 2005.

[62] C.C. Roth and D. Mohr. Ductile fracture experiments with locally proportional loading histories. *International Journal of Plasticity*, 79:328–354, 2016.

[63] L. Gurson. Continuum Theory of Ductile Rupture by Void Nucleation and Growth: Part I - Yield Criteria and Flow Rules for Porous Ductile Media. *J Mater Process Tech*, 99:2–15, 1977.

[64] A. Needleman. A continuum model for void nucleation by inclusion debonding. *Journal of Applied Mechanics*, 54(3):525–531, 1987.

[65] V. Tvergaard. On localization in ductile materials containing spherical voids. *Int J Fracture*, 18:237–252, 1982.

[66] V. Tvergaard and A. Needleman. Analysis of the cup-cone fracture in a round tensile bar. *Acta Metallurgica*, 32:157–169, 1984.

[67] Z. Li, M. Huang, and C. Wang. Scale-dependent plasticity potential of porous materials and void growth. *International Journal of Solids and Structures*, 40(15):3935–3954, 2003.

[68] V. Monchiet and G. Bonnet. A Gurson-type model accounting for void size effects. *International Journal of Solids and Structures*, 50(2):320–327, 2008.

[69] M. Gologanu, J-B. Leblond, and J. Devaux. Approximate models for ductile metals containing non-spherical voids - case of axisymmetric prolate ellipsoidal cavities. *Journal of the Mechanics and Physics of Solids*, 41(11):1723–1754, 1993.

[70] J. Besson and C. Guillemer-Neel. An extension of the Green and Gurson models to kinematic hardening. *Mechanics of Materials*, 35(1-2):1–18, 2003.

[71] K. Nahshon and J.W. Hutchinson. Modification of the gurson model for shear failure. *European Journal of Mechanics - A/Solids*, 27(1):1–17, 2008.

[72] L. Xue. Constitutive modeling of void shearing effect in ductile fracture of porous materials. *Engineering Fracture Mechanics*, 75(11):3343–3366, 2008.

[73] L. Malcher, F.M.A. Pires, and J.M.A.C. de Sá. An extended GTN model for ductile fracture under high and low stress triaxiality. *International Journal of Plasticity*, 54:193–228, 2014.

[74] Z. Chen and X. Dong. The GTN damage model based on Hill'48 anisotropic yield criterion and its application in sheet metal forming. *Computational Materials Science*, 44(3):1013–1021, 2009.

[75] S.I. Oh, C.C. Chen, and S. Kobayashi. Ductile Fracture in Axisymmetric Extrusionand Drawing—Part 2: Workability in Extrusion and Drawing. *Journal of Engineering for Industry*, 101(1):36, 1979.

[76] M. Oyane, T. Sato, K. Okimoto, and S. Shima. Criteria for ductile fracture and their applications. *Journal of Mechanical Working Technology*, 4(1):65–81, 1980.

[77] G.R. Johnson and W.H. Cook. Fracture characteristics of three metals subjected to various strains, strain rates, temperatures and pressures. *Engineering Fracture Mechanics*, 21:31–48, 1985.

[78] D. Mohr and S.J. Marcadet. Micromechanically-motivated phenomenological Hosford–Coulomb model for predicting ductile fracture initiation at low stress triaxialities. *International Journal of Solids and Structures*, 67-68:40–55, 2015.

[79] J. Lee, S.-J. Lee, and B. C. De Cooman. Effect of micro-alloying elements on the stretch-flangeability of dual phase steel. *Materials Science and Engineering: A*, 536:231–238, 2012.

[80] A. D. Rollett and S. I. Wright. *Typical textures in geological materials and ceramics*, chapter Texture and anisotropy : preferred orientations in polycrystals and their effect on materials properties, pages 178–239. Cambridge University Press.

[81] ASTM E8 / E8M-16ae1. Standard Test Methods for Tension Testing of Metallic Materials, 2016.

[82] ASTM E517-19. Standard Test Method for Plastic Strain Ratio r for Sheet Metal, 2019.

[83] J. L. Geoffroy and A. Col. Thermal influence during tensile testing. *International Deep Drawing Research Group IDDRG 2008 International Conference, 16-18 June 2008, Olofström, Sweden*, 2008.

[84] J.L. Perez and A. Rusinek. Temperature increase associated with plastic deformation under dynamic compression: application to aluminium alloy al 6082. *Journal of Theoretical and Applied Mechanics*, 2:377–398, 2012.

[85] J.T. Benzing, W.A. Poling, D.T. Pierce, J. Bentley, K.O. Findley, D. Raabe, and J.E. Wittig. Effects of strain rate on mechanical properties and deformation behavior of an austenitic Fe-25Mn-3Al-3Si TWIP-TRIP steel. *Materials Science and Engineering: A*, 711:78–92, 2018.

[86] R. Amaral, A.D. Santos, and A.B. Lopes. Mechanical properties determination of dual-phase steels using uniaxial tensile and hydraulic bulge test. *Ciência & Tecnologia dos Materiais*, 29(1):e239–e243, 2017.

[87] L.C. Reis, M.C. Oliveira, A.D. Santos, and J.V. Fernandes. On the determination of the work hardening curve using the bulge test. *International Journal of Mechanical Sciences*, 105:158–181, 2016.

[88] M. Sigvant, K. Mattiasson, H. Vegter, and P. Thilderkvist. A viscous pressure bulge test for the determination of a plastic hardening curve and equibiaxial material data. *International Journal of Material Forming*, 2(4):235–242, 2009.

[89] A. Nasser, A. Yadav, P. Pathak, and T. Altan. Determination of the flow stress of five AHSS sheet materials (DP 600, DP 780, DP 780-CR, DP 780-HY and TRIP 780) using the uniaxial tensile and the biaxial viscous pressure bulge (VPB) tests. *Journal of Materials Processing Technology*, 210(3):429–436, 2010.

[90] A.D. Santos, J. Mendes, F. Gomes de Almeida, P. Teixeira, and J. Bessa Pacheco. Caracterização de materiais em chapa metálica com o ensaio bulge: desenvolvimento de um sistema mecânico experimental. *In Actas do X Congresso Iberoamericano de Engenharia Mecânica - CIBEM 10*, pages 103–114, 2011.

[91] R. Amaral, A. D. Santos, J. A. Sousa, and A. B. Lopes. The Influence of Microstructure on the Mechanical Behaviour of Dual Phase Steels. In *Advanced Structured Materials*, volume 65, pages 25–35. Springer International Publishing, 2017.

[92] M. Atkinson. Accurate determination of biaxial stress—strain relationships from hydraulic bulging tests of sheet metals. *International Journal of Mechanical Sciences*, 39(7):761–769, 1997.

[93] X. Lemoine, A. Iancu, and G. Ferron. Flow Curve Determination at Large Plastic Strain Levels: Limitations of the Membrane Theory in the Analysis of the Hydraulic Bulge Test. volume 1353, pages 1411–1416, 2011.

[94] ISO 16808:2014(en)Metallic materials — Sheet and strip — Determination of biaxial stress-strain curve by means of bulge test with optical measuring systems, 2008.

[95] P. Peters, C. Leppin, and P. Hora. Method for the evaluation of the hydraulic bulge test. *In Proceedings of IDDRG 2011, Bilbao, Spain*, 2011.

[96] A. Mutrux, B. Hochholdinger, and P. Hora. Procedure for evaluation and validation of hydraulic biaxial experiment. *in Proceeding of Numisheet 2008 Conference, Switzerland*, pages 67–71, 2008.

[97] L. Lazarescu, I. Nicodim, I. Ciobanu, D. S. Comsa, and D. Banabic. Determination of material parameters of sheet metals using the hydraulic bulge test. *Acta Metallurgica Slovaca*, 19(1):4–12, 2013.

[98] ASTM E9-19. Standard Test Methods of Compression Testing of Metallic Materials at Room Temperature, 2019.

[99] F. Yoshida, T. Uemori, and K. Fujiwara. Elastic–plastic behavior of steel sheets under in-plane cyclic tension–compression at large strain. *International Journal of Plasticity*, 18(5-6):633–659, 2002.

[100] R.K. Boger, R.H. Wagoner, F. Barlat, M.G. Lee, and K. Chung. Continuous, large strain, tension/compression testing of sheet material. *International Journal of Plasticity*, 21(12):2319–2343, 2005.

[101] T. Kuwabara. Advances in experiments on metal sheets and tubes in support of constitutive modeling and forming simulations. *International Journal of Plasticity*, 23(3):385–419, 2007.

[102] S.J. Marcadet and D. Mohr. Effect of compression–tension loading reversal on the strain to fracture of dual phase steel sheets. *International Journal of Plasticity*, 72:21–43, 2015.

[103] M. Tritschler, A. Butz, D. Helm, G. Falkinger, and J. Kiese. Experimental analysis and modeling of the anisotropic response of titanium alloy Ti-X for quasi-static loading at room temperature. *International Journal of Material Forming*, 7(3):259–273, 2013.

[104] M.B. Gorji and D. Mohr. Micro-tension and micro-shear experiments to characterize stress-state dependent ductile fracture. *Acta Materialia*, 131:65–76, 2017.

[105] D.J. Cruz, M. Trindade, A.D. Santos, J. Mendes, R.L. Amaral, and S.S. Miranda. Development of a miniature testing for sheet metal mechanical characterization. *DCE 2019, 3rd Doctoral Congress in Engineering, Symposium on Mechanical Engineering*, page 17, 2019.

[106] K. Nakajima, T. Kikuma, and K. Hasaku. Study of the formability of steel sheets. Technical Report 264 (141–154), Yawata Technical Report, 1968.

[107] ISO 12004 standard: Metallic materials guidelines for the determination of forming limit diagrams, 2014.

[108] A.D. Santos, J.F. Duarte, and A. Barata da Rocha. *Tecnologia da Embutidura*. INEGI, 2005.

[109] R. Safdarian, H. Moslemi Naeini, R.M. Natal Jorge, A.D. Santos, and M.P.L Parente. A comparative study of forming limit diagram prediction of tailor welded blanks. *International Journal of Material Forming*, 8(2), 2014.

[110] M. Parente, R. Safdarim, A.D. Santos, A. Loureiro, P. Vilaca, and R.M Natal Jorge. A study on the formability of aluminum tailor welded blanks produced by friction stir welding. *International Journal of Advanced Manufacturing Technology*, 83:2129–41, 2016.

[111] P. Parniere and G. Sanz. Appréciation des Caractéristiques d'Emboutissabilité des Tôles Minces – Mise en forme des métaux et alliages. *CNRS, Paris,*, pages 305–330, 1976.

[112] C.C. Roth and D. Mohr. Determining the strain to fracture for simple shear for a wide range of sheet metals. *International Journal of Mechanical Sciences*, 149:224–240, 2018.

[113] J.C. Lagarias, J.A. Reeds, M.H. Wright, and P.E. Wright. Convergence Properties of the Nelder–Mead Simplex Method in Low Dimensions. *SIAM Journal on Optimization*, 9(1):112–147, 1998.

[114] P. Barros, J.L. Alves, M.C. Oliveira, and L.F. Menezes. Tension-compression asymmetry modelling: strategies for anisotropy parameters identification. *MATEC Web of Conferences*, 80:05002, 2016.

[115] D.-A. Wang, W. Y. Chien, K. C. Liao, J. Pan, and S. C. Tang. A Gurson Yield Function for Anisotropic Porous Sheet Metals and its Applications to Failure Prediction of Aluminum Sheets. *Journal of Mechanics*, 19(1):161–168, 2003.

[116] Z.L. Zhang. A Sensitivity Analysis of Material Parameters for the Gurson Constitutive Model. *Fatigue & Fracture of Engineering Materials and Structures*, 19(5):561–570, 1996.

[117] D.M. Neto, M.C. Oliveira, R.E. Dick, P.D. Barros, J.L. Alves, and L.F. Menezes. Numerical and experimental analysis of wrinkling during the cup drawing of an AA5042 aluminium alloy. *International Journal of Material Forming*, 10(1):125–138, 2015.

[118] R.L. Amaral, A.D. Santos, and S.S. Miranda. *Limiting Drawing Ratio and Formability Behaviour of Dual Phase Steels - Experimental Analysis and Finite Element Modelling*, volume 98 of *Materials Design and Applications II: Advanced Structured Materials*. Springer, Cham, 2019.

(This page was deliberately left blank)

Appendix A

Dual-phase steels engineering and true stress-strain curves

(This page was deliberately left blank)

A.1 Dual-phase steel DP500 engineering and true stress-strain curves

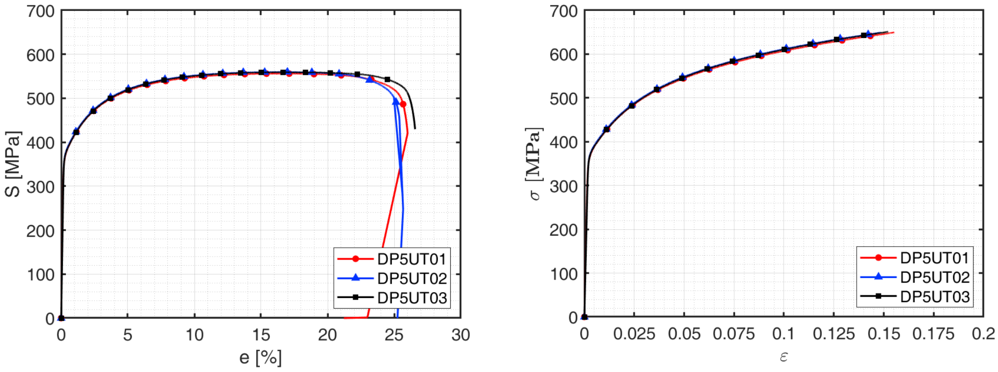

(a) Eng. stress-strain (b) True stress-strain

Figure A.1: Engineering and true stress-strain curves of DP500 for 0^o relative to RD.

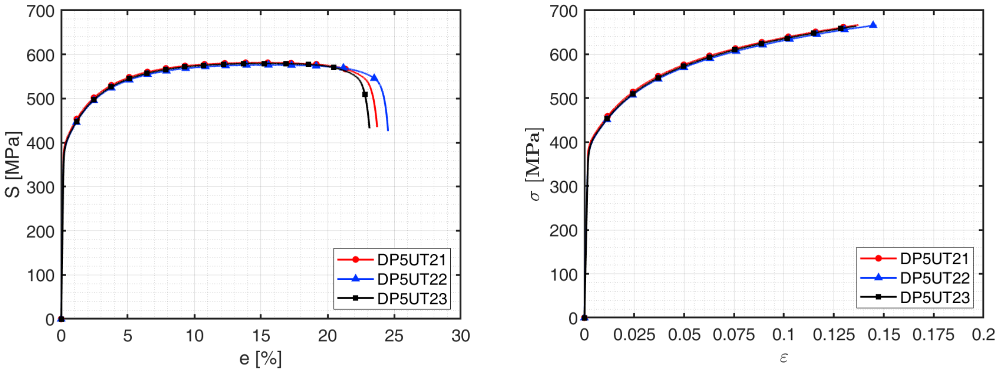

(a) Eng. stress-strain (b) True stress-strain

Figure A.2: Engineering and true stress-strain curves of DP500 for 22.5^o relative to RD.

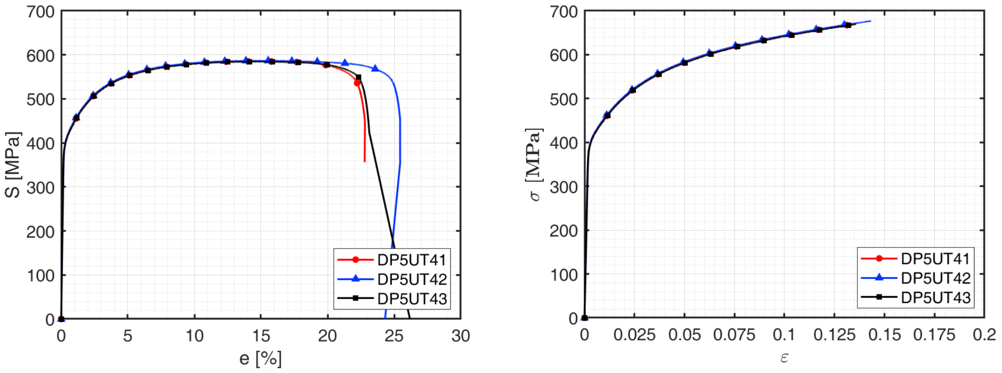

(a) Eng. stress-strain (b) True stress-strain

Figure A.3: Engineering and true stress-strain curves of DP500 for 45^o relative to RD.

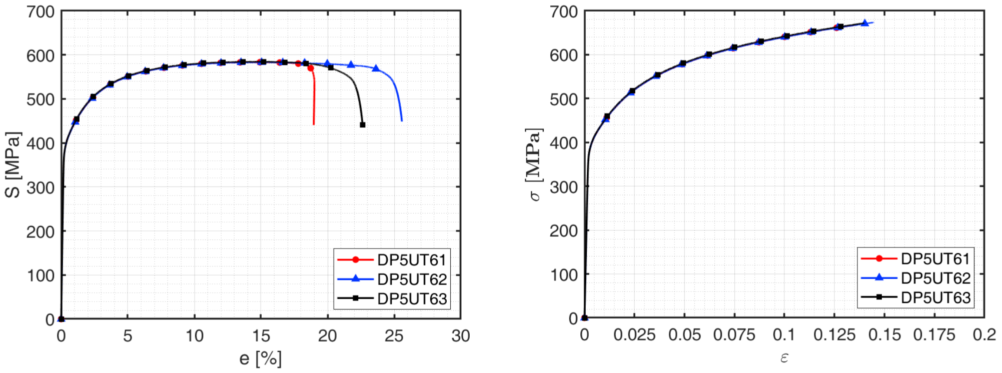

(a) Eng. stress-strain (b) True stress-strain

Figure A.4: Engineering and true stress-strain curves of DP500 for 67.5^o relative to RD.

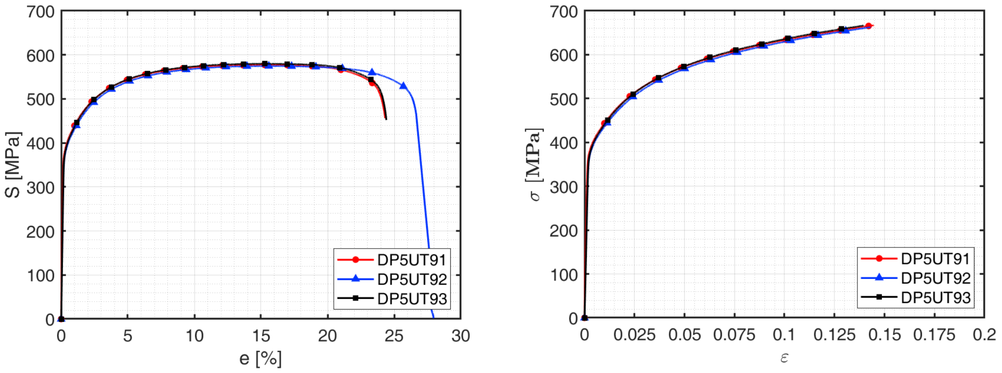

(a) Eng. stress-strain (b) True stress-strain

Figure A.5: Engineering and true stress-strain curves of DP500 for 90^o relative to RD.

A.2 Dual-phase steel DP600 engineering and true stress-strain curves

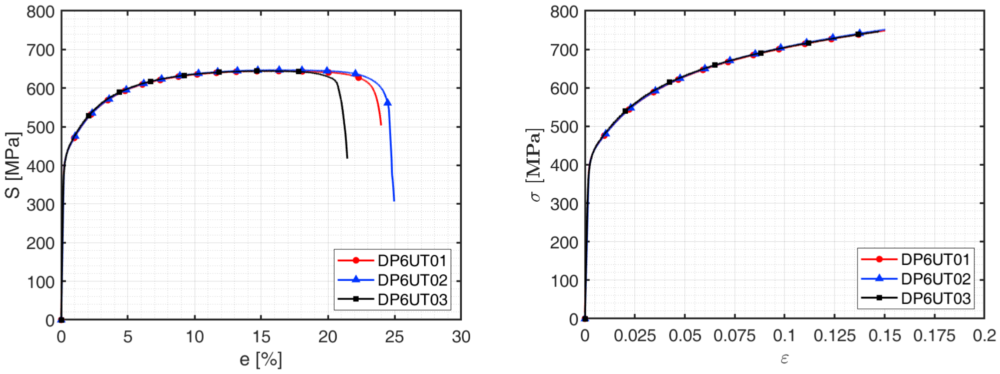

(a) Eng. stress-strain (b) True stress-strain

Figure A.6: Engineering and true stress-strain curves of DP600 for 0^o relative to rolling direction.

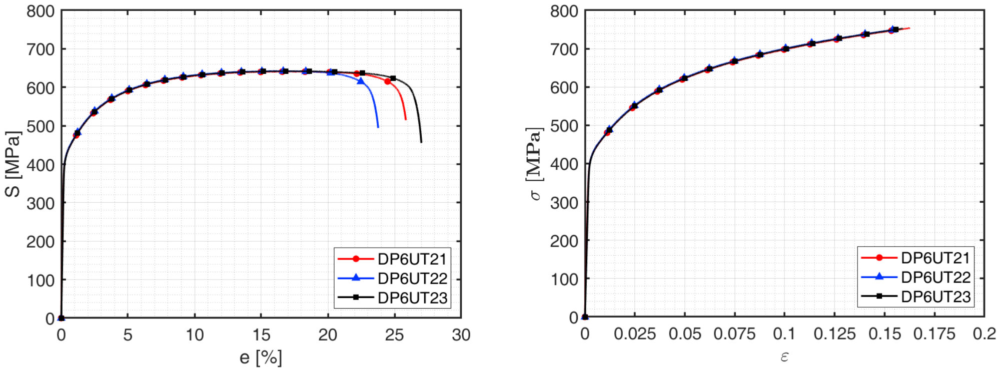

(a) Eng. stress-strain (b) True stress-strain

Figure A.7: Engineering and true stress-strain curves of DP600 for 22.5^o relative to RD.

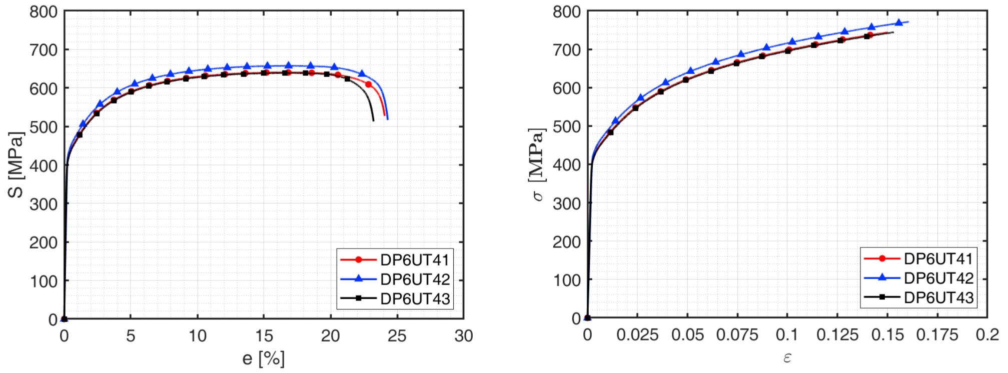

(a) Eng. stress-strain (b) True stress-strain

Figure A.8: Engineering and true stress-strain curves of DP600 for 45^o relative to RD.

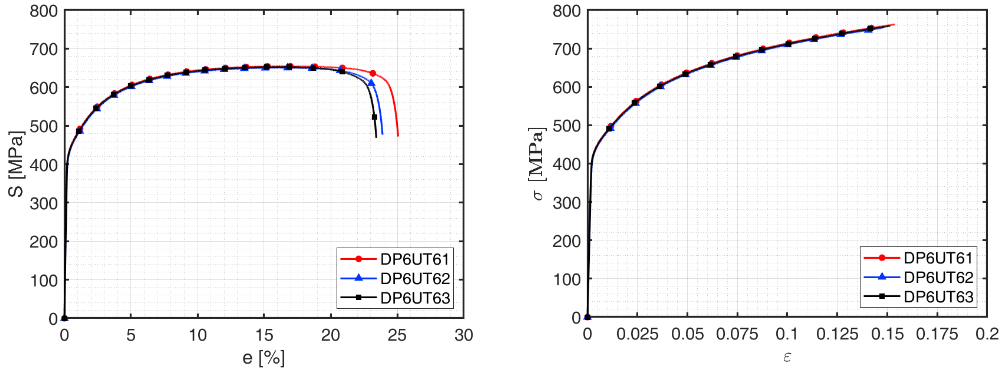

(a) Eng. stress-strain (b) True stress-strain

Figure A.9: Engineering and true stress-strain curves of DP600 for 67.5^o relative to RD.

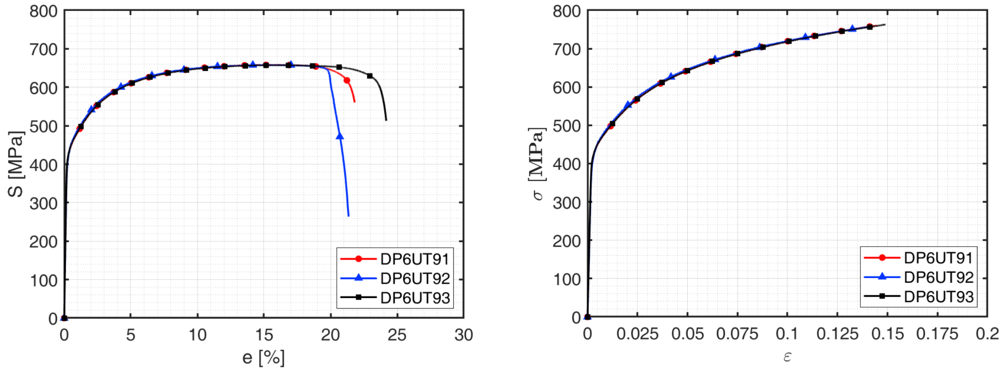

(a) Eng. stress-strain (b) True stress-strain

Figure A.10: Engineering and true stress-strain curves of DP600 for 90^o relative to RD.

A.3 Dual-phase steel DP780 engineering and true stress-strain curves

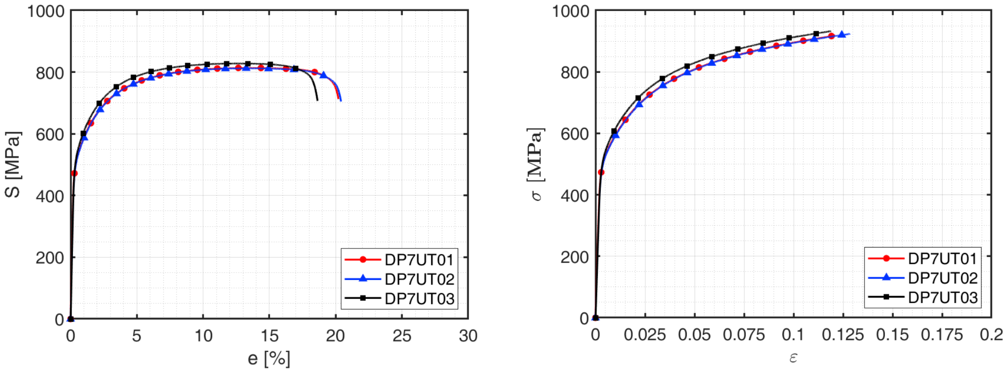

(a) Eng. stress-strain (b) True stress-strain

Figure A.11: Engineering and true stress-strain curves of DP780 for 0^o relative to rolling direction.

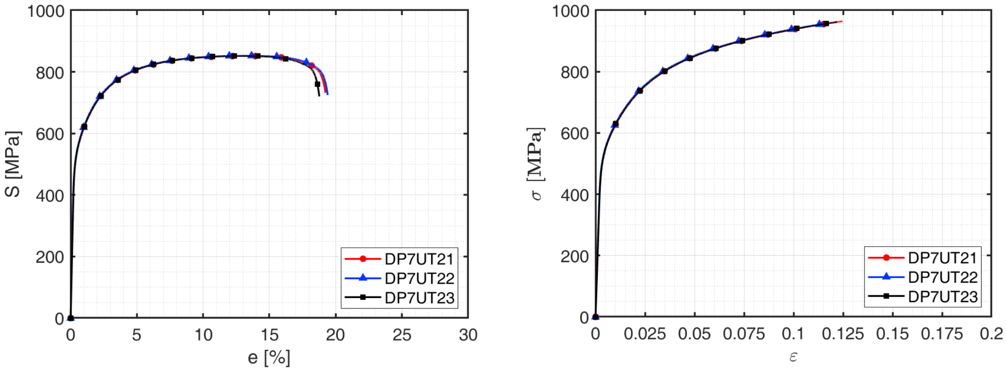

(a) Eng. stress-strain (b) True stress-strain

Figure A.12: Engineering and true stress-strain curves of DP780 for 22.5^o relative to RD.

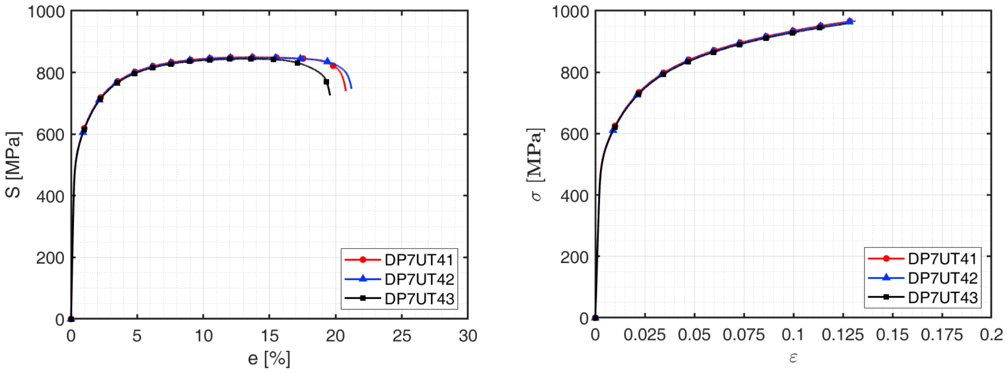

(a) Eng. stress-strain (b) True stress-strain

Figure A.13: Engineering and true stress-strain curves of DP780 for 45^o relative to RD.

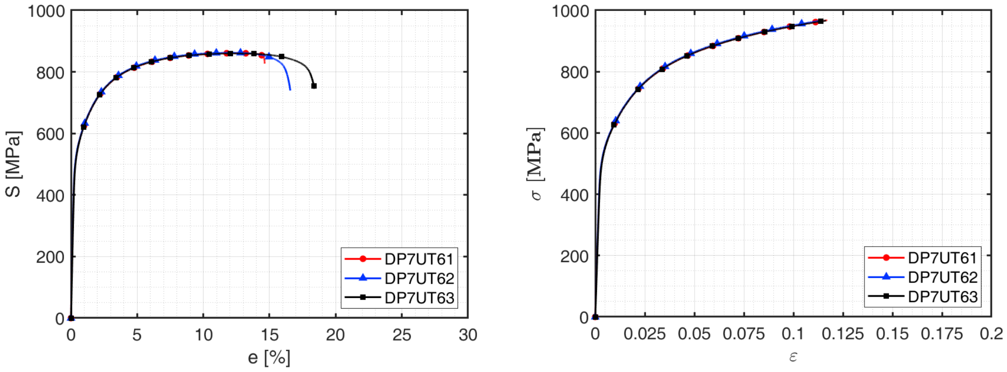

(a) Eng. stress-strain (b) True stress-strain

Figure A.14: Engineering and true stress-strain curves of DP780 for 67.5^o relative to RD.

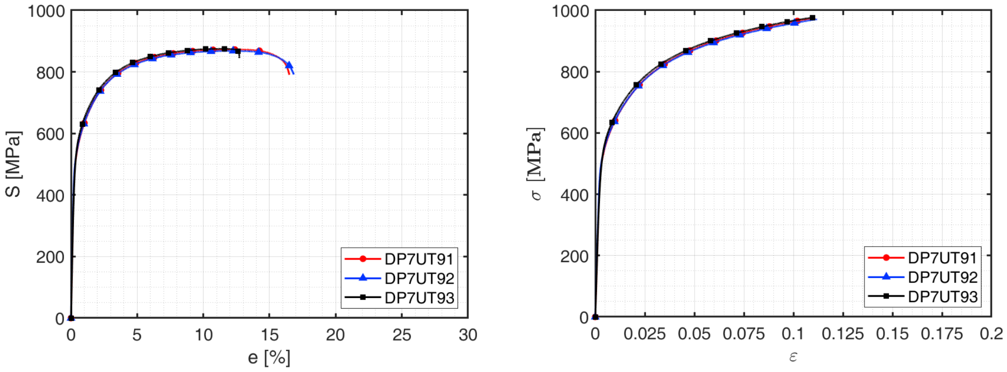

(a) Eng. stress-strain (b) True stress-strain

Figure A.15: Engineering and true stress-strain curves of DP780 for 90^o relative to RD.

Appendix B

Deep drawing cylindrical cup force-displacement curves of dual-phase steels

(This page was deliberately left blank)

B.1 Swift test force evolution with displacement of DP500 for different blank diameters

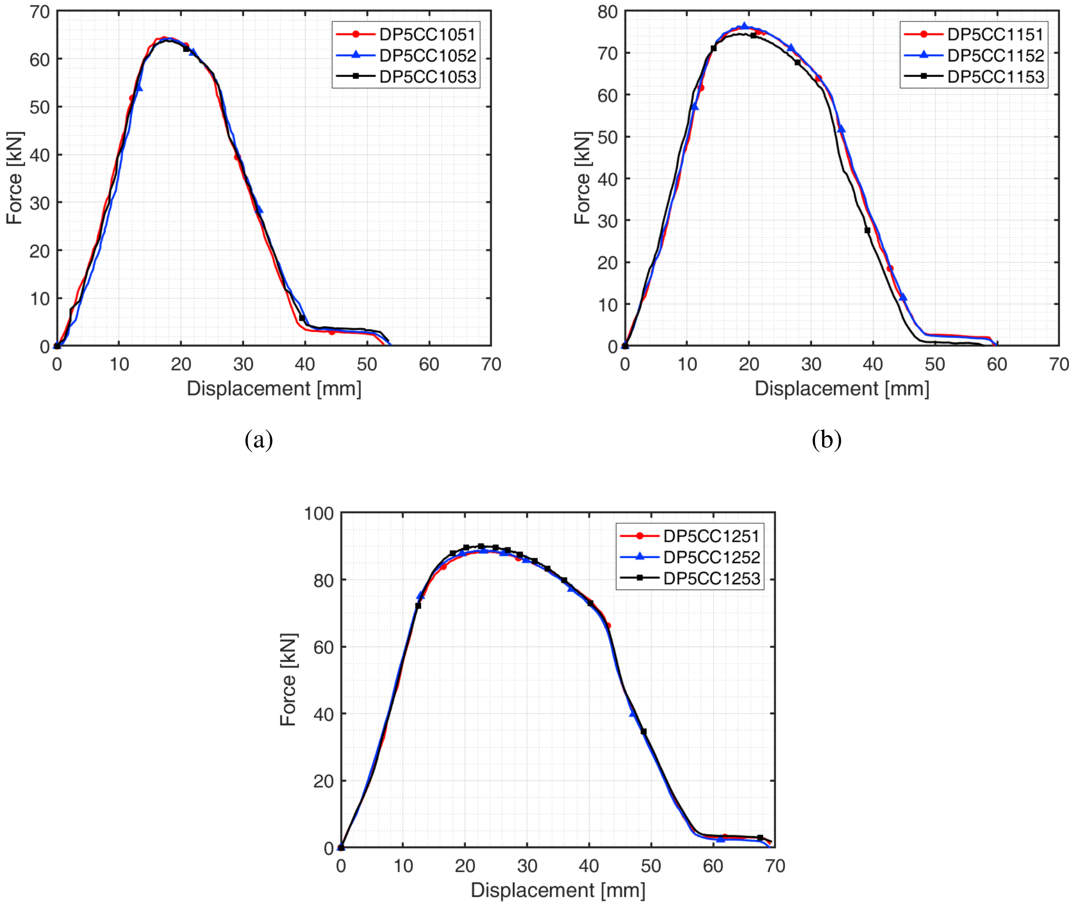

(a)

(b)

(c)

Figure B.1: Punch force evolution with displacement of DP500 for the blank diameters: a) 105 mm; b) 115 mm; c) 125 mm.

B.2 Swift test

force evolution with displacement of DP600 for different blank diameters

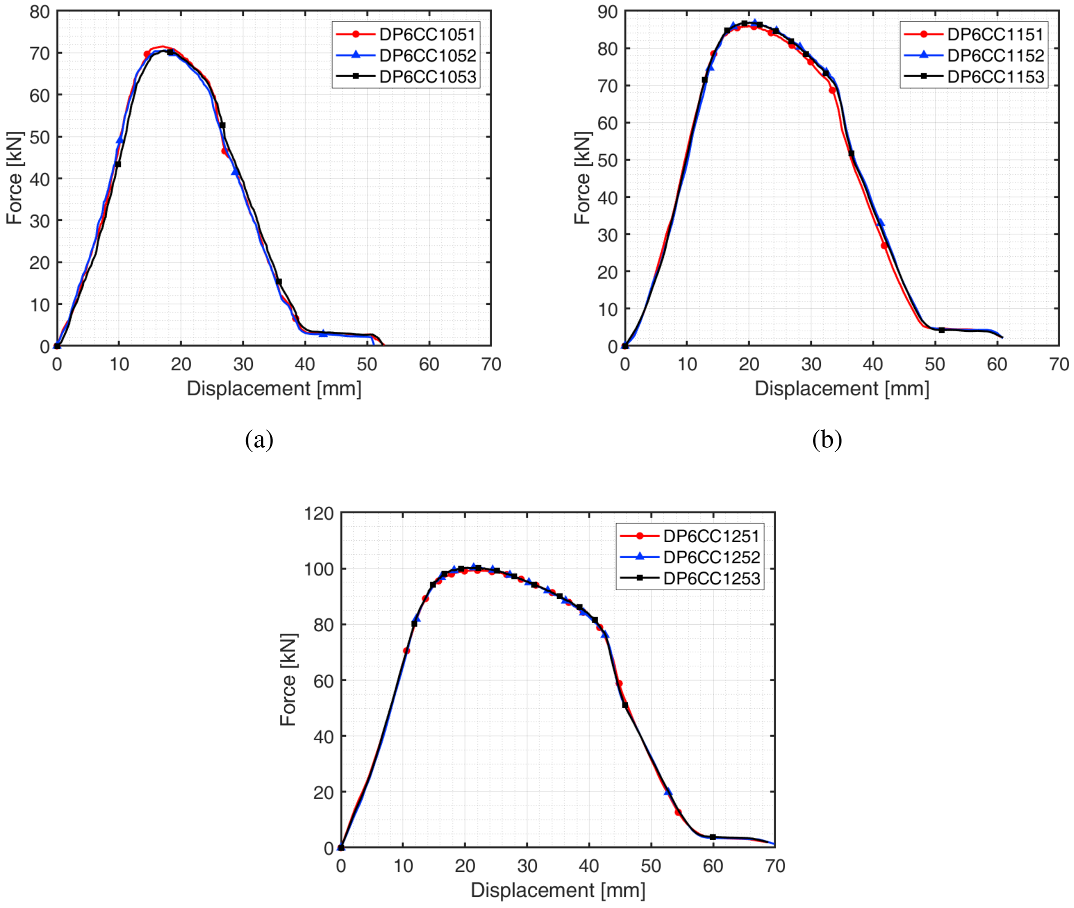

(a)

(b)

(c)

Figure B.2: Punch force evolution with displacement of DP600 for the blank diameters: a) 105 mm; b) 115 mm; c) 125 mm.

B.3 Swift test force evolution with displacement of DP780 for different blank diameters

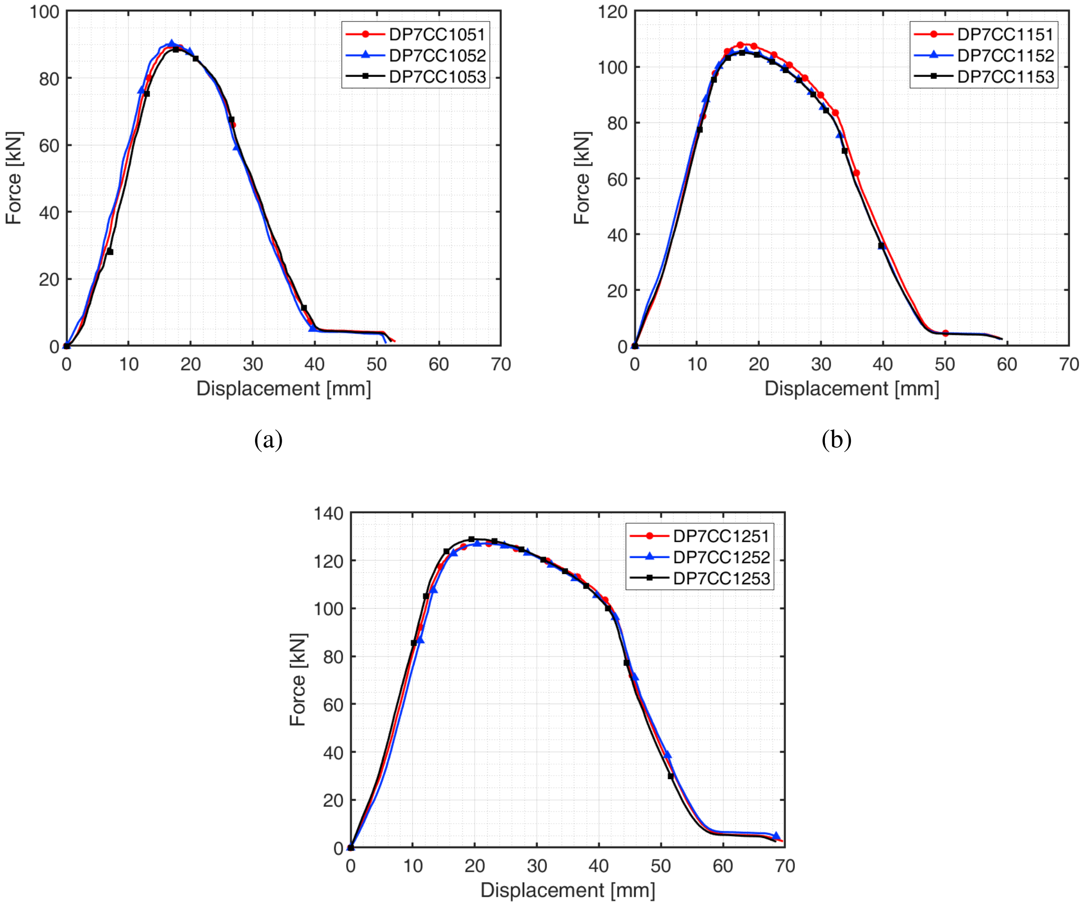

(a)

(b)

(c)

Figure B.3: Punch force evolution with displacement of DP780 for the blank diameters: a) 105 mm; b) 115 mm; c) 125 mm.